Aus dem Berlin Institute of Health Berlin-Brandenburg Center for Regenerative Therapies (BCRT) der Medizinischen Fakultät Charité – Universitätsmedizin Berlin

DISSERTATION

Quantification of structural changes in cortical bone by estimating thickness, speed of sound and pore size distribution

Quantifizierung struktureller Veränderungen im kortikalen Knochen durch Abschätzung von Dicke, Schallgeschwindigkeit und Porengrößenverteilung

zur Erlangung des akademischen Grades

Doctor of Philosophy (PhD)

vorgelegt der Medizinischen Fakultät

Charité – Universitätsmedizin Berlin von

Minh Huong Nguyen-Ullrich (geborene Nguyen)

aus Berlin

Datum der Promotion: 30.11.2023

Contents

List of abbreviations

a	Radius of cortical pore
aBMD	Areal bone mineral density
AUC	Area under the curve
BMU	Basic multicellular unit
BSC(f)	Frequency dependent backscatter cross section
$BSC^{model}(f)$	Measured model of backscatter cross section
$BSC^{theory}(f)$	Theoretical model of backscatter cross section
BUA	Broadband ultrasound attenuation
CortBS	Cortical backscatter
$Ct.\alpha_f$	Slope of attenuation $\alpha(f)$
$Ct.\alpha_o$	Intercept of attenuation $\alpha(f)$
Ct.BMD.D	Cortical bone mineral density distribution
Ct.Po	Cortical Porosity
Ct.Po.D	Cortical distributions of porosity
Ct.Po.Dm	Cortical pore size diameter
Ct.Po.Dm.D	Cortical pore size diameter distribution
$Ct.Po.Dm.D_{FWHM}$	Full width half maximum (FWHM) of Ct.Po.Dm.D
$Ct.Po.Dm.D_{FWHM,max}$	Maximum FWHM of Ct.Po.Dm.D
$Ct.Po.Dm.D_{FWHM,min}$	Minimum FWHM of Ct.Po.Dm.D
$Ct.Po.Dm.D_{Peak}$	Peak of Ct.Po.Dm.D
$Ct.Po.Dm.D_{Peak}$	Peak of Ct.Po.Dm.D
$Ct.Po.Dm.D_{Q10}$	10% quantile of Ct.Po.Dm.D
$Ct.Po.Dm.D_{Q90}$	90% quantile of Ct.Po.Dm.D
Ct.Po.Dn	Cortical pore density
Ct.Th	Cortical Thickness
$Ct.v_{11}$	Cortical speed of sound propagating in radial bone direction
DXA	Dual-energy X-ray absorptiometry
f	Frequency
F_B	Focus Depth at backside bone interface
FB	Front-backside reflection echoes
FDTD	Finite difference time domain
F_F	Focus Depth at frontside bone interface
Fz	Focus depth
HR-MRI	High-resolution magnetic resonance imaging
HR-pQCT	High-resolution peripheral quantitative computed tomography
k	Wave number
k_{eff}	Correction factor for effective aperture
L_{Tibia}	Tibia Length: as the distance between medial malleolus and medial knee joint cleft
MF	MultiFocus
NDS(f,z)	depth-dependent normalized mean difference spectrum
N_{Rx}	Transducer elements in receive
N_{Tx}	Transducer elements in transmit
PLS	Partial Least Square
PLS-LOOCV	Partial Least Square with Leave-One-Out Cross-Validation
pQCT	Peripheral quantitative computer tomography

QUS	Quantitative ultrasound
RE	Relative error
ROI	Region of interest
SD	Standard deviation
SOS	Speed of Sound
t	Time
TOF	Time of Flight
TOF_B	Time of flight of the backside echo
TOF_F	Time of flight of the frontside echo
vFAS	Velocity of first arriving signal
$\alpha(f)$	Frequency dependent attenuation coefficient
β	Refraction angle
ΔFz	Shift in focus depth for confocal focus positions
ΔTOF	Shift in Time of Flight
θ_{crit}	Critical angle
θ_{eff}	Effective aperture angle
θ_{incl}	Inclination angle
θ_{sweep}	Sweeping angle
ϕ_{steer}	Steering angle
λ	Wavelength
v_{H20}	Speed of sound of water

List of Tables

List of Figures

Abstract

Quantitative bone ultrasound (QUS) method has been introduced as a promising alternative for diagnosing osteoporosis and assessing fracture risk. The latest QUS technologies aim to quantitatively assess structural cortical bone characteristics, e.g, cortical porosity, cortical thickness (Ct.Th) and cortical speed of sound at cortical measurement regions. Large cortical pores and reduced Ct.Th in the tibia have been proposed as an indication of reduced hip strength and structural deterioration.

In this work two novel ultrasound methods were studied using a conventional ultrasound transducer to measure cortical bone properties at the tibia. The first method is a refraction and phase aberration corrected multifocus (MF) imaging approach that measures Ct.Th and the compressional sound velocity traveling in the radial bone direction (Ct.v_{11}). The second method is a novel cortical backscatter (CortBS) method that assesses microstructural properties in cortical bone. Both methods were validated in silico on bone models, ex vivo on bone samples and in vivo on 55 postmenopausal women at the anteromedial tibia midshaft. The aim of this work was to study the precision, accuracy, and fragility fracture discrimination performance of CortBS and MF parameters in comparison to clinical High-resolution peripheral quantitative computed tomography (HR-pQCT) and Dual-energy X-ray absorptiometry (DXA) measurements.

The results of the MF approach show precise and accurate estimation of Ct.Th and Ct.v_{11}. The comparison of the measured Ct.Th with reference thicknesses from HR-pQCT measurement have also shown accurate determination of Ct.Th (R^2=0.94, RMSE=0.17 mm). Future simulation studies with real bone structures from HR-pQCT measurements should target the validation of accurate Ct.v_{11} estimation. For the first time, CortBS assessed the distribution of cortical pore size and viscoelastic properties of cortical bone in vivo. The short- term in vivo precision was observed between 1.7% and 13.9%. Fragility fracture discrimination performance was retrieved using multivariate partial least squares regression. The combination of CortBS+MF showed superior fracture discrimination performance compared with DXA and similar fracture discrimination performance compared with HR-pQCT. Further clinical studies with larger cohort size should target the potential to demonstrate the ability of CortBS and MF parameters for individual fracture risk assessment.

In conclusion, alteration in cortical microstructure and viscoelasticity caused by the aging process and the progression of osteoporosis can be measured by CortBS and

MF. These methods have high potential to identify patients at high risk for fragility fractures.

Abstrakt

Die quantitative Knochenultraschallmethode (QUS) wurde als vielversprechende Alternative für die Diagnose von Osteoporose und die Bewertung des Frakturrisikos eingeführt. Die neuesten QUS-Technologien zielen darauf ab, strukturelle kortikale Knochenmerkmale, z. B. kortikale Porosität, kortikale Dicke (Ct.Th) und kortikale Schallgeschwindigkeit in kortikalen Messregionen quantitativ zu bewerten. Große kortikale Poren und eine verringerte Ct.Th in der Tibia wurden als Anzeichen für eine verringerte Festigkeit der Hüfte und eine strukturelle Verschlechterung vorgeschlagen. In dieser Arbeit wurden zwei neuartige Ultraschallmethoden unter Verwendung eines herkömmlichen Ultraschallwandlers zur Messung der Eigenschaften am kortikalen Knochen des Schienbeins untersucht. Bei der ersten Methode handelt es sich um einen brechungs- und phasenaberrationskorrigierten multifokalen (MF) Bildgebungsansatz, der Ct.Th und die Kompressionsschallgeschwindigkeit in radialer Knochenrichtung ($Ct.v_{11}$) misst. Die zweite Methode ist eine neuartige kortikale Rückstreumethode (CortBS), die die mikrostrukturellen Eigenschaften des kortikalen Knochens misst. Beide Methoden wurden in silico an Knochenmodellen, ex vivo an Knochenproben und in vivo an 55 postmenopausalen Frauen am anteromedialen Tibia-Mittelschaft validiert. Ziel dieser Arbeit war es, die Präzision, Genauigkeit und Fragilitätsfraktur-Diskriminierungsleistung von CortBS- und MF-Parametern im Vergleich zur klinischen hochauflösenden peripheren quantitativen Computertomographie (HR-pQCT) und Dualen-Energie-Röntgenabsorptiometrie (DXA) zu untersuchen.

Die Ergebnisse des MF-Ansatzes zeigen eine präzise und genaue Schätzung von Ct.Th und $Ct.v_{11}$. Der Vergleich der gemessenen Ct.Th mit Referenzdicken aus HR-pQCT-Messungen hat ebenfalls eine genaue Bestimmung der Ct.Th gezeigt ($R^2=0,94$, RMSE=0,17 mm). Zukünftige Simulationsstudien mit realen Knochenstrukturen aus HR-pQCT-Messungen sollten die genauen Schätzung der $Ct.v_{11}$ validieren. Zum ersten Mal hat CortBS die kortikale Porengrößenverteilung und die viskoelastischen Eigenschaften des kortikalen Knochens in vivo untersucht. Die kurzfristige In-vivo-Präzision lag zwischen 1,7% und 13,9%. Die Fragilitätsfraktur-Diskriminierungsleistung wurde mittels multivarianter Regression der partiellen kleinsten Quadrate bewertet. Die Kombination von CortBS+MF zeigte im Vergleich zur DXA eine überlegene Leistung bei der Frakturerkennung und eine ähnliche Leistung wie die bei HR-pQCT. Weitere klinische Studien mit größerer Kohortengröße sollten

die Fähigkeit von CortBS- und MF-Parametern zur individuellen Frakturrisikobewertung nachweisen.

Zusammenfassend lässt sich sagen, dass Veränderungen der kortikalen Mikrostruktur und Viskoelastizität, die durch den Alterungsprozess und das Fortschreiten der Osteoporose verursacht werden, mit CortBS und MF gemessen werden können. Diese Methoden haben ein hohes Potenzial zur Identifizierung von Patienten mit hohem Risiko für Fragilitätsfrakturen.

1. Introduction

1.1 Bone biology

Bone has an important role in the body by protecting vital organs, both as structural support for the whole body and also by providing and storing minerals, e.g., calcium and bicarbonate. As a living tissue, bone is constantly regenerating, a process carried out by basic multicellular units (BMUs) containing two types of bone cells, osteoclasts and osteoblasts. Osteoclasts resorb calcified bone matrix, while osteoblasts produce new bone matrix (1). At a macro structural level, bone is classified into two different types. The first type is the outer shell, which is made up of compact and dense cortical bone containing the main part of the long bone shafts, the so-called diaphysis, and composed of Harversian canals for the passage of blood vessels, lymphatic vessels, and nerves. The second type of the bone is the inner shell, the cancellous trabecular bone, which is filled with fat and marrow. In trabecular bone resorption occurs along the bone surface, whereas in cortical bone, it takes place through the bone itself (2). A circulating process of bone remodeling begins with bone resorption and concludes with bone formation (3). In adults, each bone remodeling cycle lasts 3 to 12 months (4). After the age of 50, unbalanced bone remodeling, which occurs as part of the normal ageing process, results in bone loss, especially in women during and after menopause. More bone matrix is removed than replaced by cells of the BMU leading to more non-refilled BMUs in the cortex. The clustering of BMUs at the endosteum results in the trabecularization of the inner cortex (5). Bone loss in trabecular bone is more rapid and bone fractures occur predominantly at sites, which are predominantly composed of trabecular bone e.g., the hip, spine and proximal femur (6). Therefore, studies over the last 70 years have focused on trabecular bone loss. Nevertheless, the majority of bone loss occurs after the age of 50 in cortical bone (7, 8). Because 80% of the human skeleton consists of cortical bone (7) and cortical bone is determent for bone strength (8), studies have shifted the focus towards cortical bone loss for fracture risk assessment. With advancing age, unbalanced remodeling results in increased porosity, increased pore size and cortical thinning. In addition, the transitional zone enlarges by increased trabecularization of the inner cortex. According to Chen et al. study (9), the cortical thickness of the femoral neck thins by 4% per decade for people aged 60 to 90.

1.2 Osteoporosis

Osteoporosis is the most common bone disease in the ageing population and causes more than 9 million fractures worldwide every year, with a fracture occurring every three seconds (10). It is known as a 'silent disease' because of its symptomless course until fractures occur (11). Major osteoporotic fracture sites are hip (proximal femur), non-vertebral i.e., distal forearm and vertebral fractures. Hip fractures are the greatest clinical concern with a mortality rate of 15% to 20% (12). Osteoporotic fractures can occur from a fall or simple activities, i.e., lifting objects. Osteoporosis results from unbalanced bone resorption and bone formation, and therefore, unbalanced bone turnover. Low bone mass and bone density, increased bone porosity and bone thinning are characteristics of osteoporosis (13) and results in reduce mobility and quality of life and increased healthcare costs and mortality (14). In a 1994 report, the World Health Organization has defined osteoporosis as a bone mineral density (BMD) T-score at major fracture sites, e.g., spine or proximal femur, of −2.5 standard deviation (SD) or less compared to the average BMD of a young (30 years of age) and healthy reference population (13). The current state-of-the-art technique for BMD estimation is dual-energy X-ray absorptiometry (DXA) because of its reproducibility (15). Until now it is the single most predictive diagnostic parameter and is used to determine the requirement of pharmaceutical treatment.

Different factors influence bone turnover, e.g., genetics, nutrition, environment, and biomechanics. Vitamin D, calcium, magnesium and estrogen deficiency and exogenous glucocorticoids have shown to decrease bone mass (16, 17). Osteoporosis commonly affects more women than men, especially postmenopausal women (18, 19). For postmenopausal women, estrogen deficiency results in a more rapid loss of total mass compared to men (17). Studies have shown that 50% of women (18) and 25% of men over the age of 50 have osteoporotic fractures (20). Fracture risk increases with age in both sexes and is associated with reduced bone mineral density (21).

1.3 Current in vivo assessment of bone quality

Methods for assessing bone quality use absorptiometry, computed tomography (CT), magnetic resonance imaging (MRI) and quantitative ultrasound (QUS). The current gold standard method to assess bone quality is the DXA. It uses two photon energies, i.e., 40 keV and 70 keV, and measures the attenuation of bone and soft tissue. Attenuation is converted into BMD and BMD is given by bone mineral content in grams

normalized to the two-dimensional projected bone area in cm^2. The T-score is calculated by dividing the patient's BMD by the standard deviation of the young, healthy control population (13). Although the strong relationship between low BMD and high fracture risk is well established (22, 23), around 82% of women who sustain a fragility fracture had a non-osteoporotic T-score and were not treated (24). Those patients had dominantly osteopenia BMD values between -1 to -2.49 (24). Furthermore, the definition of the cut-off value for the diagnosis and treatment of osteoporosis is -2.5 according to the World Health Organization and has not changed in the last 25 years even though the majority of women with fragility fractures are not identified with DXA. Moreover, DXA only reports bone density from two-dimensional images normalized to the bone area and is not adjusted for vertebral depth. Therefore, patients with larger and wider vertebrae and skeletons will have an overestimation of their BMD and patients with a small skeleton receive an underestimation of BMD (25). A study has reported the reduction of differences in BMD after the correction of differences in skeletal size between Asians and Caucasians (26). The differences in bone structure between different ethnic groups are also not considered in the DXA measurement and interpretation. In summary, using standard DXA measurements to diagnose osteoporosis based on BMD does not provide information about bone microstructure and structural decay with advancing age, resulting in undiagnosed and undertreated patients at high risk of fracture. DXA is not widely available in many countries due to its high cost and difficulty of reimbursement (27). In order to calculate fracture risk, FRAX® was introduced by Kanis et al. (28). It estimates the probability of major osteoporotic fractures over a 10-year period based on clinical risk factors, e.g., age, weight, history of fracture, diabetes mellitus (29). The International Osteoporosis Foundation has suggested the use of FRAX® for fracture risk estimation (30). However, FRAX® have been shown to exhibit high specificity but poor sensitivity for diagnosing osteoporosis (31).

Another technique for quantifying bone density is peripheral quantitative computer tomography (pQCT), which also uses ionizing radiation. It was introduced shortly after CT for medical imaging at the forearm, and more recently, at the tibia. Compared to the assessment of BMD from DXA, pQCT provides a volumetric bone parameter, i.e., cortical and trabecular bone mineral density, and bone volume due to small-angle fan beam X-ray source and due to the higher resolution (32). By increasing spatial resolution to 120 µm, high resolution pQCT (HR-pQCT) can additionally assess bone

microarchitecture, i.e., cortical porosity, cortical pore volume and cortical thickness. In 2004, the Swiss producer Scanco launched the first HR-pQCT to measure bone microstructure at the ultradistal radius and tibia (33). HR-pQCT measurements of bone microstructure have been shown to predict incident fractures both prospectively and retrospectively (34). Reduced cortical thickness and the presence of large pores (cortical pore size diameter > 100 µm) showed a decrease of bone strength (35) and were introduced as "quantifiable 'fingerprint' of structural deterioration" (36). Although HR-pQCT is a powerful tool to image bone changes, it is only used as research tool due to its high cost (much higher than DXA). In comparison to pQCT and HR-pQCT, MRI is a non-ionizing method. High resolution MRI (HR-MRI) with an in-plane resolution of 150 µm is used to image trabecular and cortical bone (37) and reasonable acquisition time can provide bone details (38, 39), but results in long scanning times of 20-30 min. There is no standardized HR-MRI sequence, which results in a wide variation of image quality between studies and MRI systems (40). Additional disadvantages are the loud noise and high costs.

Currently, DXA is the gold standard method for clinical management of osteoporosis (6). Meanwhile, the development of HR-pQCT has shifted the focus to cortical bone to improve fracture risk assessment of osteoporotic patients (7). In the past 30 years, quantitative ultrasound (QUS) methods have shown the ability for fracture risk assessment by measuring bone structure parameters. The next subchapter examines significant QUS approaches for assessing bone strength in cortical bone.

1.4 New alternatives for assessment of bone quality: Quantitative Ultrasound (QUS) for bone assessment

Ultrasound waves propagate, scatter, and absorb through the bone depending on the structure, stiffness, density, and elasticity of bone. In contrast to DXA, which uses X-ray photon absorption by bone atoms, QUS utilized ultrasound waves with characteristic wavelengths to interact with bone structures. Ultrasound waves interact with the bone in a complex manner, providing information on its structure. In contrast to DXA, QUS is relatively inexpensive, portable, non-ionizing and non-invasive. In the past 30 years several QUS methods have been developed to characterize bone strength and structural properties using different physical principles (6). A review of QUS approaches for bone quality assessment can be found in (6, 41). In this section the most relevant QUS techniques targeting cortical bone will be briefly introduced.

These QUS methods include transverse transmission, pulse-echo, and cortical axial transmission.

For the transverse transmission method, a transducer is positioned on both sides of the bone, a transmitter and a receiver. The ultrasound waves propagating through the skeletal site is measured and compared to the ultrasound wave transmitted through a reference medium with a known attenuation and speed of sound to estimate the broadband ultrasound attenuation (BUA) or speed of sound (SOS) (6). Both parameters have been applied clinically and are related to BMD, the proportion of trabecular and cortical bone, and the elasticity and fatigue fracture of the bone (27). QUS of the heel can predict osteoporosis-related fracture risk in elderly women to the same level as DXA (42-45). However, similar to DXA, this method cannot differentiate between trabecular and cortical bone. It only gives an estimation of the total amount of bone within the propagation path. In addition, heterogeneity of measurement techniques makes it challenging to compare measurements with QUS devices of different types and establish transmission QUS devices in clinical routine on a wider market (46).

The pulse-echo method was used in the QUS device Bindex® (Kuopio, Finland). The device measures the cortical bone thickness based on the reflected waves from the frontside (periosteal) and backside (endosteal) surface of the cortical bone at the tibia (47). The main limitation of this approach is the assumption of the radial sound velocity in cortical bone, which has been chosen to be 3565 m/s. However, studies have reported differences in speed of sound in the cortex of healthy and osteoporotic subjects from (3485 ± 128 m/s) to (3200 ± 307 m/s), respectively (48, 49). Therefore, Bindex® only measures an index instead of the true bone thickness.

The cortical axial transmission method uses transmitting and receiving transducers to measure the cortical speed of sound propagating in the longitudinal bone direction. In contrast to transverse transmission, the transmitter and receiver are positioned along the measured bone (6). The radius, tibia, and phalanges are preferred measurement regions for QUS devices using cortical axial transmission (50). Early cortical axial transmission QUS devices analyzed the ultrasound signals in the time domain, and measured the time of flight and the velocity of the first arriving signal (vFAS) to calculate the longitudinal wave velocity in bone (6, 51). The FDA-approved Sunlight Omnisense series (BeamMed Ltd, Tel-Aviv, Isreal) offers multi-skeletal site QUS in a clinical setting (52-54). Several clinical studies have reported that vFAS discriminates

healthy subjects from osteoporotic patients (50, 55-59). A study on postmenopausal women showed the association of SOS with fracture risk independent of BMD and age (60). Foiret et al. (61) proposed a dispersion curve analysis on ultrasound guided waves propagating in long bones to determine cortical thickness and velocities. The approach assumed wave dispersion in long bones with an ideal plate model having transverse isotropy and no absorption coefficient. Different ultrasound transducers have been evolved to measure cortical thickness and porosity from guided waves analysis at the radius using 1-MHz waves (62, 63) and at the tibia using 500-kHz waves (64). Based on ultrasound guided waves analysis, thickness and porosity estimations are reported to differentiate fragility fractures in postmenopausal women (62). The restriction to subjects with a low body fat index (62, 65) and high-operator dependence weakens the methods use in vivo and its translation to clinical routine.

In the past 30 years, several QUS devices have been developed to target specific bone architecture. The wide availability of conventional ultrasound systems makes the use of ultrasound in bone structure research attractive. Therefore, research groups have dedicated their work into hardware improvements. Ultrasound Bone imaging was hampered by the strong impedance mismatch between bone and soft tissue interface. Renaud et al. (66) demonstrated the first in vivo images of human cortical bone at the tibia and radius using Kirchhoff migration developed by seismologists (67) and enabled an accurate measurement of bone thickness and anisotropic sound velocity profiles. However, the method does not consider adapting the imaging approach to osteoporotic subjects with an altered bone microstructure. Another novel method to retrieve cortical bone morphology from spectral responses of reflected and backscattered waves of cortical pores in human tibia was proposed by Iori et al. (68). The method is based on a cortical backscatter model (CortBS), which predicts microstructural changes in cortical pore diameter distributions, Ct.Po, cortical pore density and material properties. So far, the method was validated in silico using finite-difference time-domain (FDTD) simulations and ex vivo on human tibia bones.

In conclusion, QUS is not recommended for monitoring osteoporosis treatment at this point (50). The current standard still remains the measurement of BMD by DXA. The current limitations for the clinical use of QUS parameters are the lack of standardization and quality control and the variability of measurements. However, QUS methods are promising for evaluating bone quality (6). Previous studies showed a strong association between cortical speed of sound and BMD (69) and Ct.Po (70, 71). Thus,

cortical speed of sound was introduced as an indicator for bone status (72). Speed of sound in the cortex of healthy and osteoporotic subjects are reported to differ (48, 49). With advancing age, unbalanced bone resorption and bone formation results in cortical thinning. Recent studies reported about 20% variation in cortical thickness between healthy and osteoporotic subjects (73, 74). In fact, Szulc et al. (75) demonstrated a decrease of cortical thickness of 1.10% ± 1.06% per year resulting in increased bone fracture risk in postmenopausal women. Iori et al. (35) reported a reduction in bone strength with decreased cortical thickness. In conclusion, reduced cortical thickness, speed of sound and cortical porosity has been shown to provide "quantifiable 'fingerprint' of structural deterioration" (36).

1.5 Outline of the dissertation

The purpose of this project was to develop a refraction corrected MultiFocus (MF) imaging technology using ultrasound waves to image the periosteal and endosteal cortical bone surface and to determine both the cortical thickness (Ct.Th) and also the radial sound velocity in cortical bone (Ct.v_{11}). Both cortical parameters have been shown to be biomarkers for bone quality (24, 67). The confocal depth and travel time of reflections from the periosteal and endosteal cortical bone surface are determined by focusing waves at various depths. In combination with microstructural cortical bone properties, i.e., cortical porosity, cortical density and cortical pore size distribution, predicted from CortBS proposed in Iori et al. (68), we hypothesize a superior discrimination performance of the CortBS and MF measurement compared to the gold standard DXA method and the current high resolution HR-pQCT measurement for bone structure assessment. Both developed techniques, MultiFocus and CortBS, use conventional ultrasound technology and are highly clinically feasible for identifying people with high fracture risk. Therefore, the aims of this work are to:

- Establish image and signal processing methods to validate the estimation of cortical thickness and cortical speed of sound in silico and ex vivo on plate-shaped materials using the MF imaging sequence (Study A)
- Analyze the precision and accuracy for thickness and speed of sound estimation compared to reference values (Study A)
- Expand signal processing methods for the transition into curved bone structures with realistic in vivo transducer to bone distance (Study B)

- Validate MF approach on in silico and ex vivo measurement using phase aberration correction methods (Study B)
- Validate signal processing methods for MF in vivo measurements (Results)
- Validate CortBS method in vivo and study the discrimination performance compared to DXA and HR-pQCT measurements (Study C)

2.   Method and Materials

2.1 Samples

Study A used plate-shaped materials for in silico and ex vivo validation of the MF method. For in silico validation, 4mm thick bone plates with different cortical bone properties (porosity, pore diameter and pore density) were simulated. For ex vivo validation homogenous materials of polymethylmethacrylate (PMMA), polycarbonate (PC) and polyvinylchloride (PVC), heterogenous plates of short fiber-reinforces epoxy (Sawbone, Malmoe, Sweden) and porous plates of bovine tibia bone, cut with a band saw (EXCAT GmbH, Remscheid. Germany) were used. Study B used curved-shaped bone models for in silico validation and a tibia bone sample from a human cadaver for ex vivo validation. In Study C, 55 postmenopausal women (aged 57 – 85 years, mean: 70 ± 7 years) were recruited at the Center for Muscle and Bone Research, Berlin, after a clinical DXA bone density measurement. To investigate the fracture discrimination, the patients were recruited according to three patient groups: i) osteoporosis; ii) osteopenia with prevalent fragility fracture); iii) osteopenia without prevalent fragility fracture. In addition to the postmenopausal women, three healthy volunteers (age 25, 31 and 52) participated.

2.2 Numerical Ultrasound propagation model

For in silico validation of the MF methods, bone models were simulated using the two-dimensional finite difference time domain (FDTD) method with Simsonic (www.simsonic.fr) (76) to model ultrasound wave propagation in cortical bone. Simsonic is a software which considers multiple scattering, refraction, wave conversion, diffusion and frequency-independent absorption occurring during the wave propagation through bone.

All bone model geometries consisted of 4 mm thick cortical bones surrounded by water. The bone properties are summarized in Study A (Tab. I (77)) and Study B (Tab. 2 (78)). Study A used a linear transducer array with 32-element sub-aperture (element and pitch sizes: 0.3mm), which emitted ultrasound waves with a broadband pulse, a center frequency of 5 MHz, and a -6dB bandwidth of 60% towards the 4mm thick bone plates at a distance of 4 mm away from the transducer array (77).

Study B used a linear transducer array with 64-element sub-aperture (element and pitch sizes: 0.3 mm) to ensure an appropriate beam opening angle for the MF acquisition at a realistic transducer-bone distance of 15 mm for future in vivo

measurements. The center frequency was changed to a lower frequency of 4 MHz to avoid scattering.

2.3 Ex vivo ultrasound measurements

For ex vivo validation, all samples were scanned using a medical ultrasound scanner SonicTOUCH, a linear ultrasound transducer 4DL14-5/38 with center frequency of 8 MHz and 128 elements and a pitch size of 0.3 mm. A single-channel data acquisition system SonixDAQ (Ultrasonix, Richmond, BC, Canada) was used to capture pre-beamformed single-channel RF data of all 128 channels at a sampling rate of 40 MHz with 12-b resolution during the data acquisition (77). Figure 1 shows the MF imaging setup (77). The samples were placed in degassed water at a distance of 20 mm from the transducer array. All ex vivo MF measurements were performed using B-mode images with conventional delay and beamforming with a gradually increasing focus depth starting above the samples. For an optimal penetration depth, a transducer emitted ultrasound waves with a transmission frequency of 5 MHz was used resulting in a center frequency of 5.1 MHz and a -6dB bandwidth of 69%.

Fig. 1: "Schematic illustration of the multifocus measurement in the radial direction (x, z) of a long bone. The transducer is positioned 20 mm above the sample. Focused sound beams are emitted using a 32-element subaperture of a 128-element linear array. The semi-aperture angle θ of the transmit beam is gradually decreased to move the focus from a depth above the sample front side to a position below backside of the sample. Refraction at the frontside interface results in a change the propagation direction of transmitted waves, and thereby, a shift of the focus depth inside the sample. ΔFz indicates the shift of the focus depth needed to focus from the frontside (F_F) to the backside (F_B). In addition to the scan of the focus depth, the sub-aperture was scanned along the array (x) direction" (reprinted from Nguyen Minh et al. (77) with permission under Creative Commons 4.0 license).

2.4 In vivo ultrasound measurements

For the in vivo measurements, the same medical ultrasound scanner SonicTOUCH and set up as mentioned above for ex vivo measurements were implemented. In vivo measurements were performed at the anteromedial surface of the tibia midshaft for

two main reasons. First, the tibia midshaft is primarily composed of cortical bone (79). Second, the Ct.Th at 45-55% of the tibia length on the anteromedial site of the tibia remains relatively invariant and is thicker with respect to the long-axis positions (80). The patient's leg with the lowest aBMD (areal bone mineral density) at the proximal femur was chosen for ultrasound measurements (81). Lumbar spine and proximal femur were scanned using DXA (Lunar Prodigy Advance EnCore Software v13.4 or Lunar iDXA EnCore Software v 16.1, GE Medical Systems, Wisconsin, USA). The tibia length (L_{Tibia}) was defined as the distance between the medial malleolus and the medial knee joint cleft (81). At 50% of L_{Tibia} the measurement position was marked with a skin pencil as described in Study C (81). The ultrasound transducer 4DL14-5/38 was placed at the marked region using an ultrasound gel pad (aquaflex®, Parker Laboratories, Inc., Fairfield, NJ) to ensure an optimal coupling to the skin and bone surface. Conventional B-mode scans provided immediate visual feedback to position the transducer such that the center position of the periosteal bone interface appeared at the center of the B-mode image, and the periosteal bone interface was approximately parallel to the transducer array (81).

For MF acquisitions, conventional B-mode imaging sequences at N_{Tx}= 128 lateral scan positions x_i with a 32-element transmit aperture were repeated with progressively greater focus distances (77). In total, 19 focus depths with a step size of 1.75 mm were acquired starting from 3 mm above the center position of the periosteal bone. In addition, the excitation frequency was decreased from 5 MHz to 4 MHz, this was to increase the penetration depth, and the pulse shape was changed from "+" pulse to "+-" pulse to widen the bandwidth and lower the frequency compared to study A. The SonixDAQ captured single-channel RF data (N_{Rx} = 128) and provided a 4-D Matrix V(N_{Tx}, F_z, N_{Rx}, t) with dimensions 128 × 19 ×128 × 1023 for postprocessing (77).

For CortBS acquisitions, multi-angle 3-D compound B-mode scan sequences at N_{Tx} = 128 lateral scan positions x_i with a 16-element transmit aperture were used (Fig. 2). Three different beam steering angles θ_{sweep} (-10°, 0°, 10°) and fifteen sweeping angles ϕ_{steer} (-7° to 7° with an increment of 1°) acquired the multi-angle scan. The focus depth F_z was defined approximately 1 mm below the center position of the periosteal bone (81). The SonixDAQ captured single-channel RF data (N_{Rx} = 128) and provided a 5-D Matrix V(N_{Tx}, θ_{sweep}, ϕ_{steer}, N_{Rx}, t) with dimensions 128 × 3 × 15 ×128 × 1023 for postprocessing.
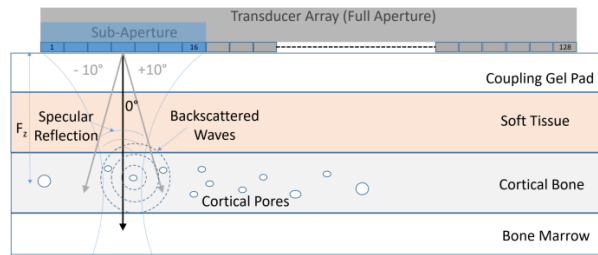
Fig. 2: "Schematic drawing of the CortBS method. A focused beam generated by a 16-element sub-aperture of the 128-element transducer array is scanned and steered across the bone. The focus depth F_z is positioned approximately 1 mm below the bone surface. Pulse-echo signals are recorded simultaneously with all 128 channels" (reprinted from Armbrecht et al. (81) with permission under Creative Commons 4.0 license).

2.5 Ultrasound data analysis, MF post-processing

2.5.1 MF post-processing

The MF method simultaneously measures thickness and longitudinal speed of sound of a sample based on the method proposed by Hänel (82), Maev et al. (83), and Raum (84). Hänel's study uses two focus positions to focus the acoustic wave on the front- and backside of the sample with a focusing lens of an acoustic microscope. In contrast, the MF method uses multiple focus depths of an ultrasound array to focus ultrasound waves starting above the frontside and down though the sample. Furthermore, the MF approach uses a broadband pulse to increase the temporal resolution and a smaller frequency range from 4-5 MHz (compared to other studies using frequency ranges up to 100 MHz) for the speed of sound estimation of biological hard tissue (85-87), to avoid scattering.

A transmit sub-aperture emitted broadband pulses with multiple focus depth through the sample. A large sub-aperture angle θ ensures high lateral spatial resolution. For each focus depth, the shift in time of flight (ΔTOF) and the maximum amplitudes of the Hilbert envelope of front-and backside (FB) reflection echoes [$V_F (x, F_z)$ and $V_B (x, F_z)$] were tracked (Fig. 3). The ΔTOF is dependent on the sample thickness, the ratio of the speed of sound between the sample and the surrounding medium, and the phase of the reflected ultrasound signals with respect to the inclination angles θ. Only at the focal plane of the frontside and of the virtual focus are all ultrasound wave components in phase. The virtual focus depth is deeper than the backside depth position caused by the increased speed of sound in the sample compared to the surrounding medium.
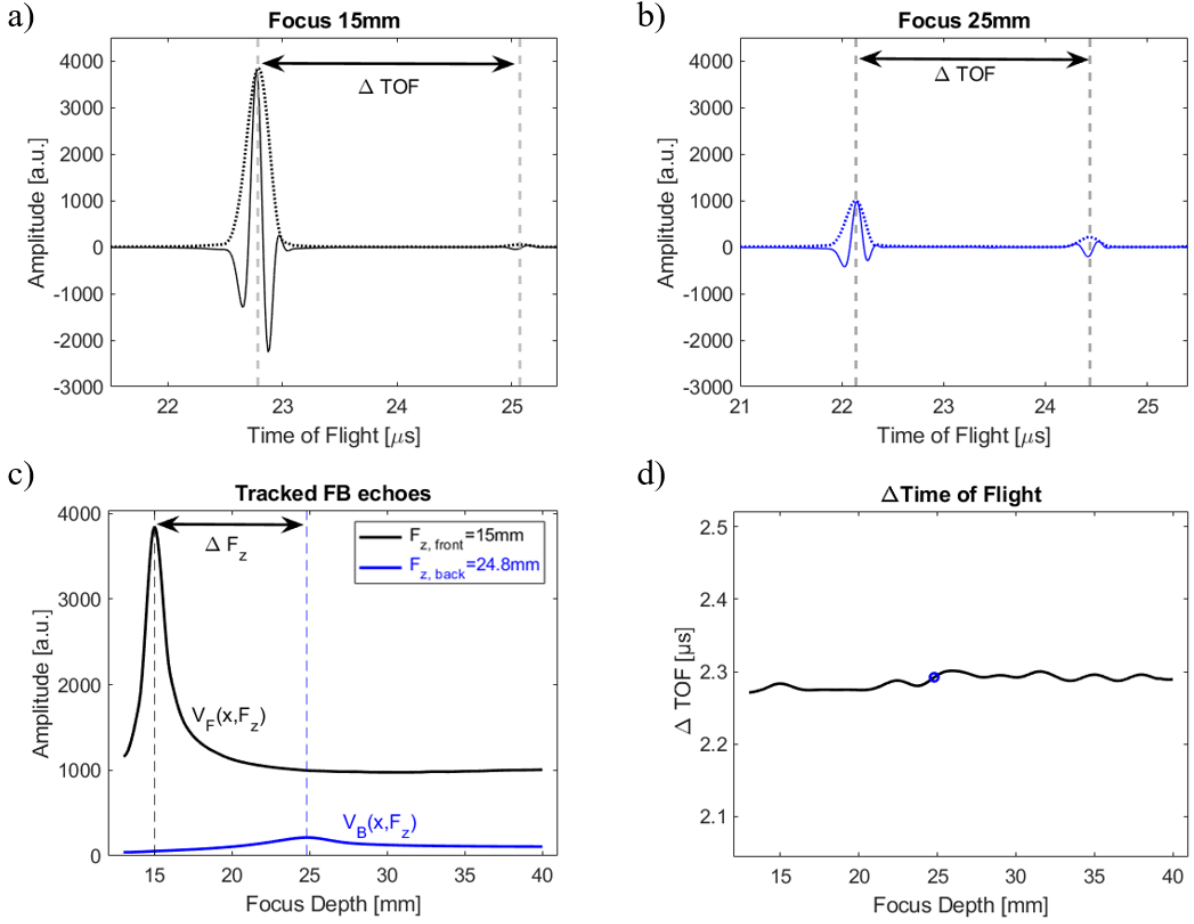
Fig. 3: a) Representative plot of frontside reflections by focusing at the frontside interface with a focus depth of 15mm and b) of backside reflections by focusing at the backside at 25mm for a 4mm thick bone plate model at a 15mm distance with 64-element sub-aperture transducer array of Study B. The difference in time of flight ΔTOF was estimated by peak positions of Hilbert-transformed envelope beamformed signal (dashed line). c) Confocal focus position of front- and backside reflections ΔF_z were extracted from tracked amplitude of FB echoes over all focus depths. d) Tracked ΔTOF over all tracked focus depths and used ΔTOF for Ct.Th and $Ct.v_{11}$ estimations at confocal focus position (blue circle).

At the frontside focal plane the lateral components of the focused ultrasound wave cancel each other out. The time of flight of the frontside echo TOF_F is determined by the focus distance F_F and the speed of sound of the surrounding material v_{H2O}, i.e., water for in silico and ex vivo measurements and soft tissue for in vivo measurements

$$TOF_F = \frac{2 \cdot F_F}{v_{H_2O/\text{soft tissue}}}. \tag{I}$$

For focus depths below the sample frontside interface the ultrasound wave front generates longitudinal waves and shear waves, which will be reflected at the backside interface. Ultrasound waves with large aperture angles generate shear waves, which travel along the sample surface resulting in decreasing longitudinal wave transmission. At a virtual focus depth, the time of flight of the backside interface TOF_B is determined by the following parameters:

17

- TOF_F (time of flight of the frontside echo)
- ΔF_z (the needed focus shift to the virtual focus depth)
- Ct.Th (sample thickness)
- θ_{incl} (inclination angle)
- β (refraction angle)
- Ct.v_{11} (speed of sound of the sample)
- $v_{H_2O/soft\ tissue}$ (speed of sound of the surrounding medium)

$$\textbf{TOF}_{\textbf{B}} = \textbf{TOF}_{\textbf{F}} - \frac{2 \cdot \Delta \textbf{F}_{\textbf{z}}}{v_{H_2O/soft\ tissue} \cdot \cos\theta_{incl}} + \frac{2 \cdot \textbf{Ct.\,Th}}{\textbf{Ct.\,v}_{11} \cdot \cos\beta}. \qquad \text{[II]}$$

The shift in the time of flight between the front-and backside interface using the Snell's law results in

$$\Delta\textbf{TOF} = \frac{2 \cdot \Delta\textbf{F}_{\textbf{z}}}{v_{H_2O/soft\ tissue} \cdot \cos\theta_{incl}} \cdot \left(1 - \frac{v_{H_2O/soft\ tissue}^2}{\textbf{Ct.\,v}_{11}^2}\right) \qquad \text{[III]}$$

and therefore, the longitudinal speed of sound Ct.v_{11} in

$$\textbf{Ct.\,v}_{11} = \sqrt{\frac{v_{H_2O/soft\ tissue}^2}{1 - \frac{\Delta\textbf{TOF} \cdot v_{H_2O/soft\ tissue} \cdot \cos\theta_{incl}}{2 \cdot \Delta\textbf{F}_{\textbf{z}}}}}. \qquad \text{[IV]}$$

The needed shift in focus depth for confocal focus positions ΔF_z was described in Maev et al. study (83) as

$$\Delta\textbf{F}_{\textbf{z}} = \textbf{Ct.\,Th} \cdot \left(1 - \frac{\textbf{Ct.\,v}_{11}}{v_{H_2O/soft\ tissue}}\right). \qquad \text{[V]}$$

The combination of (4) and (5) results in the following equation (77)

$$\textbf{Ct.\,Th} = \left(\frac{\Delta\textbf{F}_{\textbf{z}}}{0.5 \cdot \frac{\textbf{Ct.\,v}_{11}}{v_{H_2O/soft\ tissue}} \cdot \left(1 - \frac{\textbf{Ct.\,v}_{11}^2}{v_{H_2O/soft\ tissue}^2}\right) \cdot (1 - \cos(\textbf{k}_{eff} \cdot \theta_{incl})) - \frac{\textbf{Ct.\,v}_{11}}{v_{H_2O/soft\ tissue}}}\right). \qquad \text{[VI]}$$

In addition, the relation between Ct.Th and Ct.v_{11} of

$$\textbf{Ct.\,v}_{11} = \frac{2 \cdot \textbf{Ct.\,Th}}{\Delta\textbf{TOF}} \qquad \text{[VII]}$$

results in two equations [VI] and [VII] with two unknown parameters to estimate a unique solution for thickness Ct.Th and speed of sound Ct.v_{11} values.

The effective aperture θ_{eff} in equation [VI] considers increased wave conversion from compressional into shear waves with an increased angle of incidence (77) (Fig. 4a)

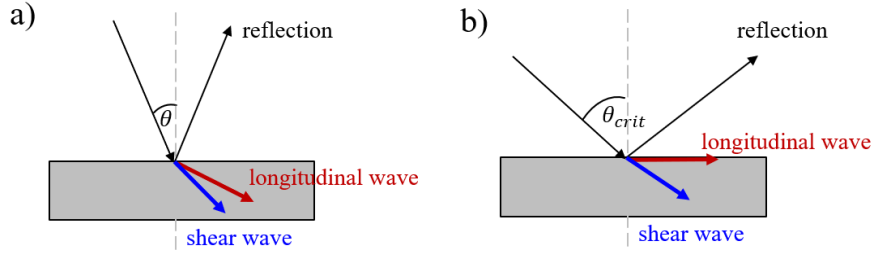and transmission loss into the sample (bone) for an inclination angle larger than a critical angle (Fig. 4b).

Fig. 4: Schematic illustration of longitudinal and shear waves in cortical bone. a) Longitudinal and shear waves were reflected at the backside surface. Due to longitudinal waves traveling faster than shear waves, these were used for MF post-processing. b) When a critical angle θ_{crit} was reached, the longitudinal waves traveled along the surface and resulted in a complete lack of longitudinal wave transmission into the bone.

Therefore, the following algorithm to estimate the effective factor was applied

$$\mathbf{k_{eff}} = \begin{pmatrix} \mathbf{1} & \text{if } \boldsymbol{\theta} \leq \boldsymbol{\theta_{crit}} - \mathbf{10°} \\ \mathbf{b \cdot \Delta\theta} & \text{if } \boldsymbol{\theta} > \boldsymbol{\theta_{crit}} - \mathbf{10°} \end{pmatrix}, \quad \text{[VIII]}$$

with b = 0.1 for Study A (77) and b= 0.122 for Study B (78) and $\Delta\theta = \theta_{crit} - \theta$. The factor k_{eff} started from 1 and was determined in five iteration steps (Study A) or was interrupted for larger transducer-bone surface distance at $k_{eff} = 0.6$ to avoid overestimation (Study B).

In summary, for each receiving channel and each focus position, the difference in time of flight of front- and backside reflections ΔTOF (Fig. 3a and b) and confocal front-backside focus position ΔF_z (Fig. 3c) were tracked to estimate Ct.Th and $Ct.v_{11}$ with equation [VI] and [VII]. Both $\Delta TOF = TOF_B - TOF_F$ and $\Delta F_z = F_{z,B} - F_{z,F}$ were retrieved at the peak position of $V_F(x, F_z)$ and $V_B(x, F_z)$. For $V_F(x, F_z)$ and $V_B(x, F_z)$ and ΔTOF the data was interpolated with a step size of 0.1 mm using spline interpolation.

Phase aberration methods

For the transition into in vivo measurements, Study B validated the MF approach on curved bone structures without pores to study the effect of bone geometry on the MF method. Figure 6 shows a schematic of the phase aberration of the received reflected backside signals caused by the bone curvature when compared to an ideal flat plate shaped bone sample. Note, that only ideal flat plate shaped bone samples were considered in Study A. In Figure 5, the concept of conventional delay and sum beamforming using a linear transducer array for a beamformed signal of a flat bone sample is shown. Each element of the transducer transmitted ultrasound waves with predefined beamform delays based on the focal point, i.e., backside bone interface,

and speed of sound of the surrounding material. Afterwards, the reflected ultrasound waves were captured by the receiver channels and beamforming delays were added for each received channel signal. When ultrasound waves were transmitted at a confocal backside focal depth $F_{z,B}$ the received backside signals were in phase and aligned after adding a beamforming delay. When ultrasound waves were transmitted with focal depths smaller than $F_{z,B}$ the backside signals were out of phase and showed a convex shape. In contrast, for focal depths larger than $F_{z,B}$ the backside signal showed a concave shape. At a confocal focus depth $F_{z,B}$ beamformed signals after delay and sum beamforming show higher amplitudes compared to beamformed signals smaller or larger than confocal focus depth $F_{z,B}$.
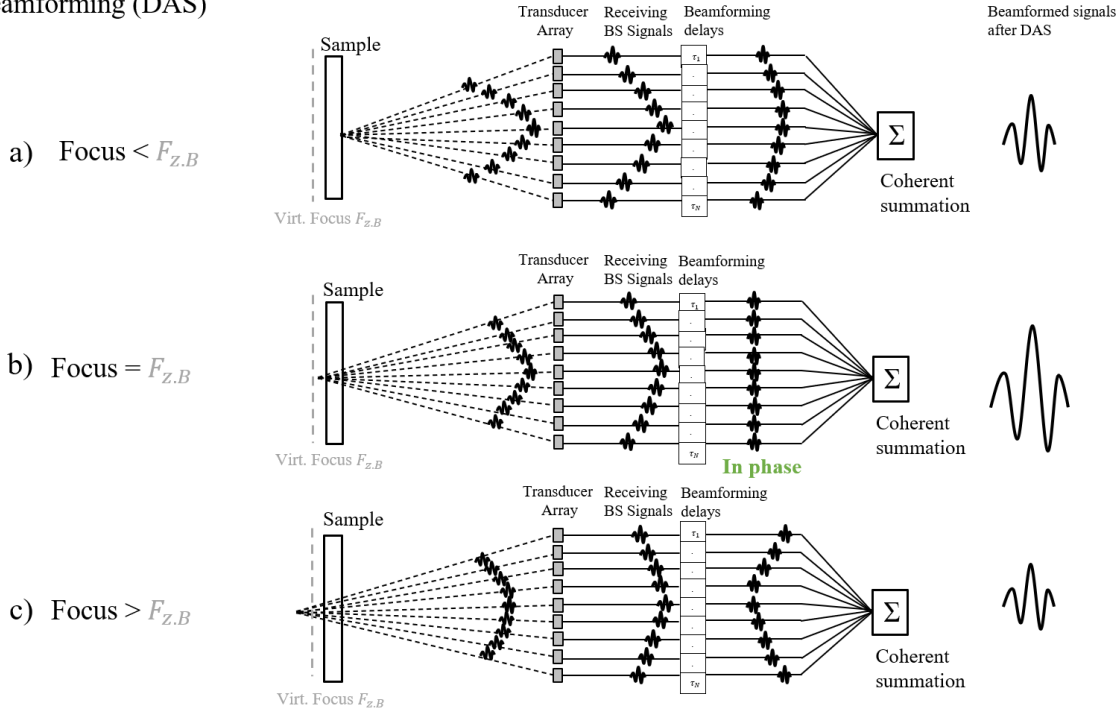
Fig. 5: Schematic illustration of delay and sum beamforming of backside signals at a) focal depths smaller the confocal backside focus depth $F_{z,B}$, b) at $F_{z,B}$ and b) at focal depths greater than $F_{z,B}$. The signals left from the transducer arrays shows the signals transmitted from the transducer to focus at a certain depth. The signals right to the transducer array illustrates the reflected backside signals captured by the received channels. The signals on the right side to the beamforming delays shows the signals after adding the beamforming delays. After delay and sum beamforming the beamformed signals is illustrated ion the right side of figure.

Additional phase aberration due to bone curvature is shown in Figure 6. Curved bone interfaces will cause additional shifts in time of flight compared to an ideal flat bone interface. The received reflected backside signals will not be in phase after adding beamforming delays (blue signals in Fig. 6) and the beamformed signal after

summation will be decreased in amplitude compared to the beamformed signal of an ideal flat bone sample.

Fig. 6: Schematic illustration of phase aberration caused by bone curvature. For a flat plate shaped bone sample, the received reflected backside signals are aligned after conventional delay and s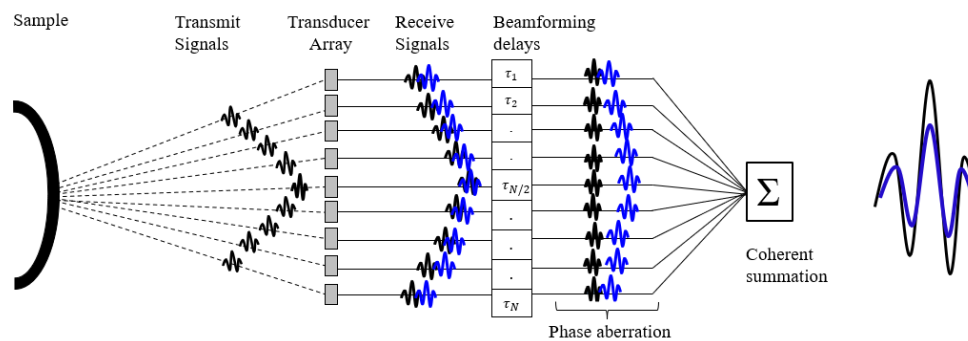um beamforming for focus position at the backside bone interface (black signals). For a curved shaped bone sample, the transmitted signals will travel longer path in the surrounding material and cause additional phase shifts of the reflected backside signals (blue signals). Therefore, receiving signals are not aligned after delay and sum beamforming, resulting in a decreased beamformed signal after summation.

Phase aberration methods of surface geometry time shift, autocorrelation function and cross-correlation corrections were used in addition to conventional delay and sum beamforming (Study B (78)).

The surface geometry time shift correction considered the additional time shift of the ultrasound waves propagating in the surrounding tissue caused by the bone curvature compared to a plate shaped bone surface. The method of autocorrelation function correction was used to correct the tilt of reflected ultrasound waves when bone surfaces were tilted with respect to the beam axis. The cross-correlation method was used to retrieve the curvature of the backside signals at each focus depth $p_1(F_z)$ with second order fits to retrieve the confocal backside focus depth $F_{z,B}$ instead of using the peak position at $V_B(x, F_z)$. The $F_{z,B}$ was defined at a zero-crossing point of the $p_1(F_z)$ by using a linear fit over $p_1(F_z)$.

2.5.2 CortBS post processing

The estimation of cortical pore properties from cortical backscattering has been proposed by Iori et al. (68). The initial idea for the method arose from the high dependence of backscattering intensity (backscatter cross section) on the product of ultrasound wave number $k=2\pi/\lambda$, with ultrasound wavelength λ, and the scatter dimension 'a', i.e., radius of the cortical pore (Fig. 7). For scattering cortical pores smaller than wavelength ($ka < 1$, Rayleigh scattering), the backscattering cross-section for i.e., pores with a pore diameter from 7 to 95 µm reported in (35, 88) shows

approximately a linear relation to ka. For small frequencies (f < 1 MHz and ka → 0), the backscattering coefficient diminishes and the temporal overlap between reflected and backscattered waves from pores will increase. For large frequencies (f > 10 MHz and ka > 1, Mie scattering) the backscattered cross section does not increase further, and ultrasound attenuation is approximately proportional to f^2, which results in a reduced penetration depth. Therefore, the frequency range between 1 and 10 MHz is optimal in order to separate specular reflections. These reflections are caused by the periosteal and endosteal cortical bone interfaces. In summary, the analysis of backscattered signals from internal cortical pores and changes in the backscattered spectral response related to variation of cortical pore dimension is performed in the frequency range from 1 to 10 MHz.
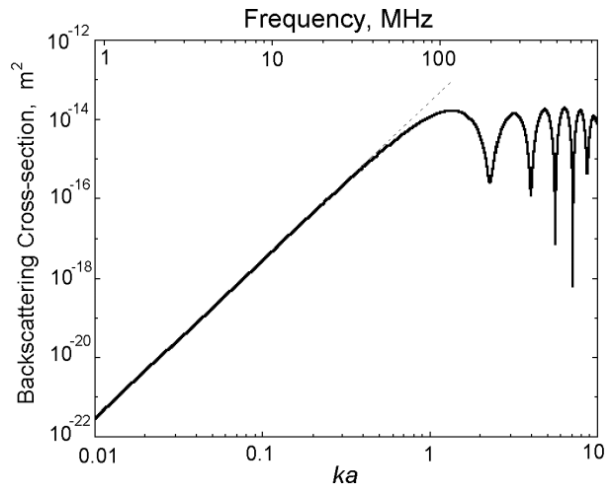
Fig. 7: Backscattering cross-section, which represents the intensity of acoustic backscatter with respect to ka (reprinted from Cobbold (89), Fig. 5.4, with permission from Oxford Publishing Limited).

Based on numerical FDTD simulations, an attenuation backscattered cross section *BSC(f)* and an attenuation coefficient *α(f)* were obtained, and a theoretical backscatter coefficient model of cortical bone *BSC^{theory}(f)* was derived (68). A detailed description of the estimation of *BSC(f)* and *α(f)* and the backscatter model *BSC^{model}(f)* was reported in (68) and are not part of this PhD thesis.

A schematic illustration of all CortBS analysis steps is shown in Figure 8. From the pre-beamformed 128-channel data, spectral analysis was performed within the manual selected region of interest (ROI, Fig. 8a green box) by calculating a normalized and depth-dependent mean difference spectrum (*NDS(f,z)*) (Fig. 8b) using local beam inclination and an inclination corrected mean surface reflection spectrum (81). From *NDS(f,z)*, the frequency dependent attenuation *α(f)* was calculated by extrapolating the attenuated intensities for frequencies within the bandwidth of the transducer (3.5-9

MHz) with linear regression to the depth of 0 (Fig. 8c). From $\alpha(f)$ the intercept α_0-, slope α_f - value and attenuation value at center frequency α_{6MHz} were extracted. From the backscatter coefficient $BSC^{model}(f)$ the mean backscatter coefficient was derived. Finally, the cortical pore size diameter distribution (*Ct.Po.Dm.D)* was calculated by the smallest error between measured and theoretical backscatter coefficient using analytical pore size distribution.
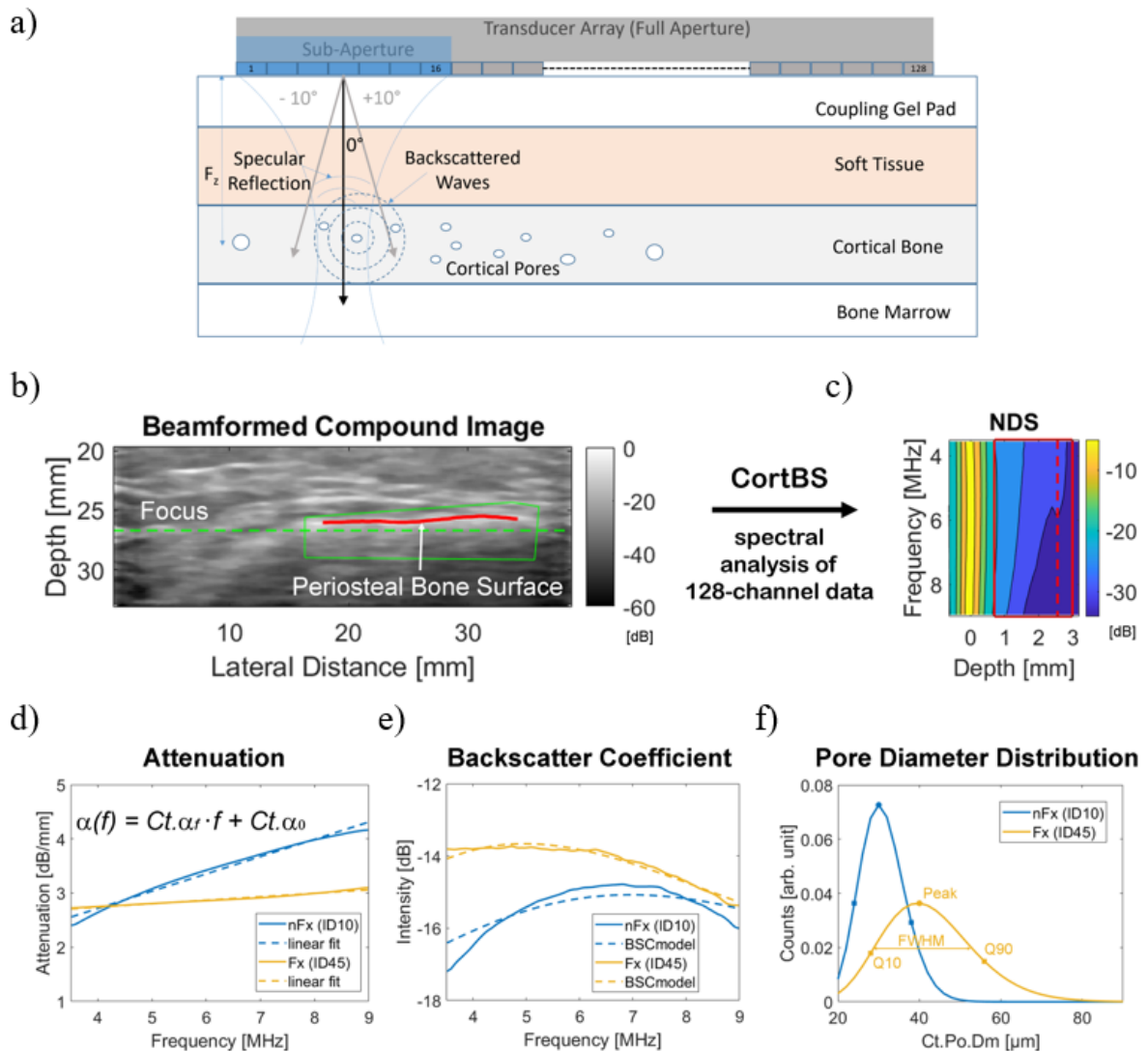
Fig. 8: Representative graphs for the CortBS analysis. "Schematic drawing of the CortBS method (a). A focused beam generated by a 16-element subaperture of the 128-element transducer array is scanned and steered across the bone. The focus depth F_z is positioned approximately 1 mm below the bone surface. Pulse-echo signals are recorded simultaneously with all 128 channels. The reconstructed compound B-mode image (b) shows the anteromedial cross section of the tibia midshaft (green dashed line: focus position; green line: manually selected ROI; red line: detected periosteal interface within ROI). The reconstructed 3D bone surface (red line) is used to calculate a depth-dependent spectrogram. Spectra arising from specular reflections at the bone surface are used for normalization. From the normalized depth-dependent backscatter spectrum (NDS) (c), the depth and frequency ranges of 1 to 3 mm and 4 to 9 MHz, respectively, are used to derive the attenuation and backscatter coefficients $\alpha(f)$ (d) and *BSC(f)* (e). By fitting model-based backscatter coefficients" (68) "to the measured *BSC(f)*, the cortical pore diameter distribution Ct.Po.Dm.D is estimated (f). (e, f) Shown are representative *α(f)*, *BSC(f)*, and Ct.Po.Dm.D data for one subject with (ID45; T-score_Total = -2.0) and one without fragility

fractures (ID10; T-score_Total = -3.5)." (81) (Reprinted from Armbrecht et al. (81) with permission under Creative Commons 4.0 license).

Table 1 summarizes the derived parameter for MF and CortBS measurements.

Tab. 1: Derived cortical bone parameters from MF and CortBS measurements

Method	Parameter	Study
MF	Ct.Th [mm]	A,B
	Ct.v_{11} [m/s]	A,B
CortBS	Ct.α_o [dB/mm]	C
	Ct.α_f [dB/MHz/mm]	C
	Ct.Po.Dm.D$_{Peak}$ [µm]	C
	Ct.Po.Dm.D$_{Q10}$ [µm]	C
	Ct.Po.Dm.D$_{Q90}$ [µm]	C
	Ct.Po.Dm.D$_{FWHM}$ [µm]	C
	Ct.Po.Dm.D$_{FWHM,min}$ [µm]	C
	Ct.Po.Dm.D$_{FWHM,max}$ [µm]	C

2.6 HR-pQCT: reference measurement

For in vivo validation of the measured cortical bone parameters at the marked 50% L$_{Tibia}$ site-matched HR-pQCT scans were conducted with an Xtreme CT II scanner (Scanco medical AG, Bassersdorf, Switzerland). The lower leg of the patient was immobilized in a carbon-fiber cast provided by the manufacturer to minimize patient movement in the gantry (81). The gantry was moved proximally towards the marked 50% L$_{tibia}$ region. A total stack length of 9 mm with a nominal isotropic voxel size of 60.7 µm was scanned and resulted in 168 slices. The total effective radiation dose was less than 5 µSv (90). Cortical properties at the anteromedial surface of the tibia were assessed using a customized protocol modified from (91).

2.7 Statistics

Study A and B used relative error (RE), standard deviation (SD), and the coefficient of variation as precision values. Precision was calculated by the difference between a measured and the reference values divided by the mean of the reference values. The accuracy was assessed by the root-mean-squared error divided by the reference values (77, 78). Study C employed classification algorithm using multivariate PLS discrimination analyses with Leave-One-Out Cross-Validation (PLS-LOOCV) with the libPLS library (92) to study the prediction potential of fracture discrimination of CortBS, DXA and HR-pQCT parameter (81). A Subwindow Permutation Analysis derived significant cortical bone variables. Mean and standard error (SE) of the area under the curve (AUC) of the receiver operating characteristics (ROC) analysis, accuracy,

sensitivity, specificity and Odds Ratio with 95% Confidence Intervals were determined (81). MATLAB R2019b including the Signal Processing, Curve Fitting, and Statistics Toolboxes (The Mathworks, Natick, MA, USA) was used for all statistical tests.

3.   Results

Effect of effective aperture on MF estimations

The MF simulation using a 32-element transducer and 4 mm thick flat bone plate model in Study A was simulated with a realistic in vivo transducer to bone interface distance of 15 mm (77). The tracked FB echoes and ΔTOF between the peak positions of FB echoes over each focus depth are shown in Figure 9a and b. The comparison showed a less sharp confocal peak arising from the FB echoes for larger transducer bone distance. The increase of transducer elements from 32 to 64 resulted in a return to a sharp confocal peak at tracked FB amplitudes (Fig. 9c). The ΔTOF between confocal FB peak positions stayed approximately the same for all three simulation models. In contrast, ΔF_z and semi-aperture angle θ decreased for the simulation model with the 32-element aperture and 15 mm transducer bone distance. The semi-aperture angle is dependent on the element numbers and transducer to bone distance. For the simulation models with 32-element aperture the semi-aperture angle decreased from 19.18° to 11.75° for larger transducer bone distance (Tab. 2). Therefore, the difference between $\Delta\theta = \theta_{crit} - \theta$ will not remain under 10° and an effective aperture will not take into account for the calculation ($k_{eff} = 1$) based on equation [VIII], which results in a false estimation of Ct.Th and Ct.v_{11}. For the appropriate beam opening angle the element number was increased from 32 to 64 (Study B) resulting in a semi-aperture angle of 20.77° and $\Delta\theta$ smaller than 10° for estimation of an effective aperture $k_{eff}\theta$. In comparison to Study A, in Study B the estimation of k_{eff} was not always derived in five iteration steps but interrupted when the threshold value $k_{eff} = 0.6$ was reached. Smaller values lead to an overcorrection of Ct.Th and Ct.v_{11}.
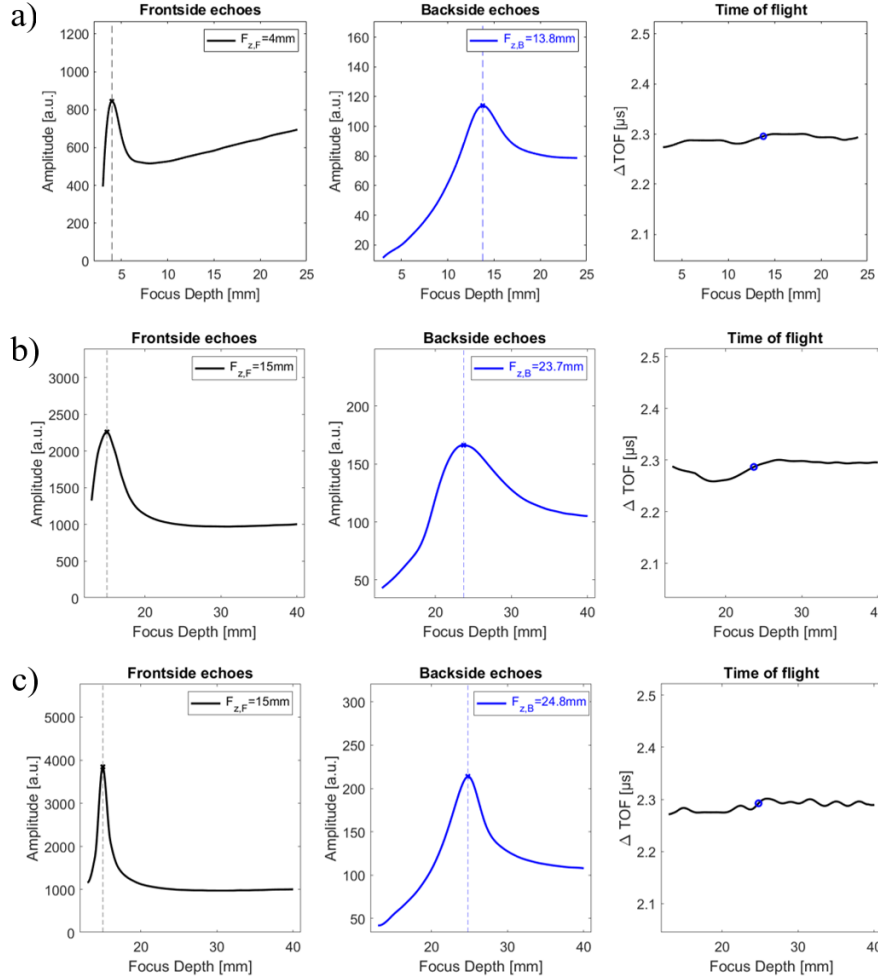
Fig. 9: Tracked FB amplitudes and shift in time of flight between the peak position of FB echoes versus focus depth for 4 mm thick flat bone plate model using a) a 32-element aperture and 4 mm transducer to bone distance, b) a 32-element aperture and 15 mm transducer to bone distance, c) a 64-element aperture and 15 mm transducer to bone distance.

Tab. 2: "Results of Ct.Th^{MF}, Ct.v$_{11}$^{MF} , and relative errors (RE) for the bone plate models with different element apertures" and transducer bone distance "using shift in time of flight between confocal" FB echoes "ΔTOF", semi-aperture angle θ, "critical angle θ$_{crit}$ for the effective aperture k$_{eff}$θ" with correction factor k$_{eff}$ (adapted from Nguyen Minh et al. (78) with permission under Creative Commons 4.0 license)

Transducer bone distance [mm]	Ap	ΔTOF [μs]	θ [°]	θ$_{crit}$ [°]	k$_{eff}$	k$_{eff}$θ [°]	Ct.Th^{MF} [mm]	RE [%]	Ct.v$_{11}$^{MF} [m/s]	RE [%]
4	32	2.296	19.18	25.4	0.62	11.96	4.01	0.25	3495	0.17
15	32	2.287	11.75	25.4	1	25.4	3.79	5.27	3310	5.54
15	64	2.292	20.77	25.4	0.6	13.82	4.00	0.01	3490	0.41

Estimation of confocal backside focus depth F$_{z,B}$ using cross-correlation

The F$_{z,B}$ was retrieved from the peak position of interpolated V$_B$ (x, F$_z$). Figure 9 showed the dependence of F$_{z,B}$ on the sharpness of V$_B$ (x, F$_z$). Peak detection results in an imprecise retrieval of F$_{z,B}$ for models with less sharp confocal peak from their tracked backside amplitude reflections V$_B$ (x, F$_z$). The sharpness of V$_B$ (x, F$_z$) depends on many factors, e.g., porosity, bone flatness, and aperture. Therefore, study B included the

26

cross-correlation method to retrieve the shift in the time of flight for the backside reflections ΔTOF_B compared to the reference channel Rx_{Ref} from pre-beamformed signals before summation. The Rx_{Ref} was defined as the channel with the highest backside amplitude. Figure 5 illustrates the shape of backside echoes for the three cases $F_z < F_{z,B}$, $F_z = F_{z,B}$, and $F_z > F_{z,B}$. The shape transitions from a concave to a convex curvature. The change of the curvature p_1 was determined by a second order fit. As an example, Figure 10 shows the second order fit of ΔTOF_B at different focus depths (Fig. 10a) and the retrieved curvature values $p_1(F_z)$ (Fig. 10b) for a curved bone model with a curvature radius r=40mm. A linear fit on $p_1(F_z)$ was performed to retrieve the confocal backside focal depth $F_{z,B}$ at the zero-crossing point of $p_1 = 0$. A similar figure to show the schematic illustration of the cross-correlation method is shown in the Appendix C of Study B in Figure A3 e and f for a plate shaped bone model without any bone curvature (flat bone plate model) (78). This method resulted in an improved extraction of $F_{z,B}$ instead of using the peak position of $V_B (x, F_z)$, especially when $V_B (x, F_z)$ is less sharp.
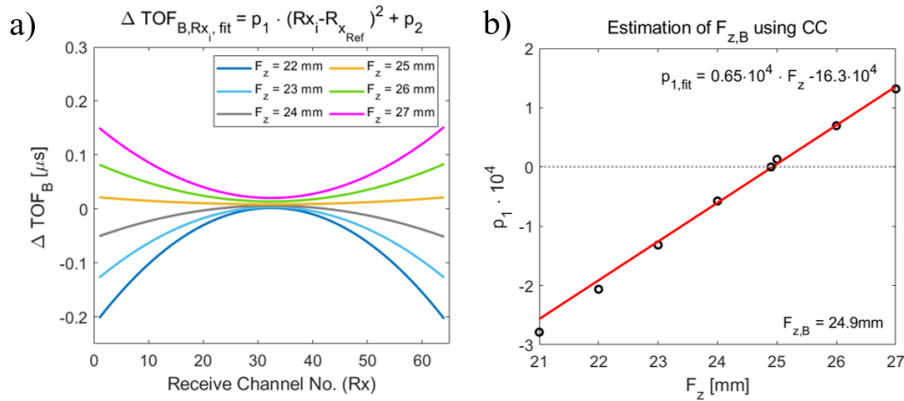
Fig. 10: Example of estimating the confocal backside focus depth $F_{z,B}$ using cross-correlation on curved bone model with curvature radius of 40 mm. a) Second order fit at the tracked shift in the time of flight of backside echoes ΔTOF_B for different focus depths F_z. b) Retrieved curvature value p_1 of the second order fit over F_z (black circles). The red line represents the first order fit to extract zero crossing point of $p_1 = 0$ to retrieve confocal backside focal depth $F_{z,B}$.

Transition into in vivo measurements

The excitation pulse with 5 MHz and "+" pulse shape from ex vivo validations in Study A was changed to 4 MHz with pulse shape "+-" (Fig, 11b green line) to extend the bandwidth to smaller frequencies and to increase the energy of the ultrasound wave. The amplitude for pulse shape "+-" increased when compared to the "+" shape and the bandwidth for the excitation pulse at 5 MHz with "+" pulse shape compared to the

4 MHz with "+-" pulse shape increased from 60.6% to 71.8% using bandpass filter from 0.5 to 8.5 MHz.
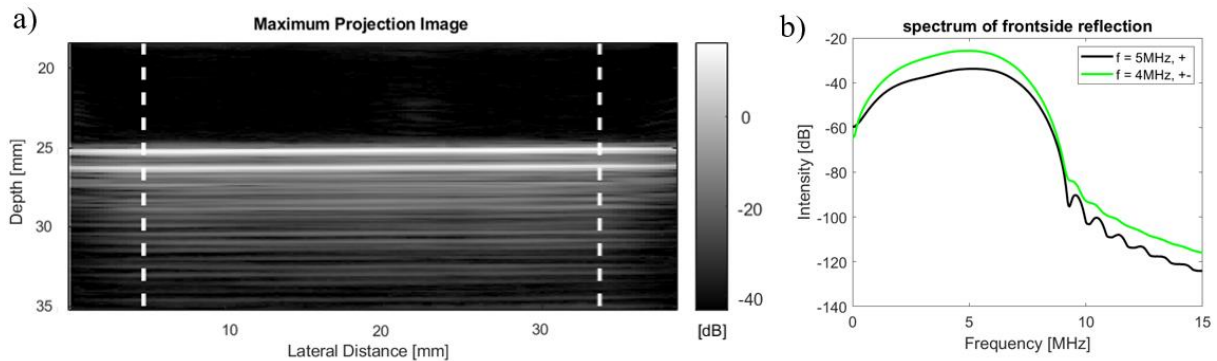
Fig. 11: a) Maximum projection image of 2 mm thick PMMA plate 25 mm below the transducer. The dashed vertical lines mark range of the spectral analysis. b) Mean power spectrum of all gated frontside reflection echoes for 96 channels between the dashed vertical lines in the maximum projection image.

Multifocus in vivo measurements

The results of in vivo MF post-processing for one patient of the in vivo study are shown in Figure 12. The comparison of the maximum projection image with and without phase aberration corrections (Fig. 12a and b) showed an increase of visibility of the endosteal bone interface. The tracked periosteal and endosteal bone interfaces were matched to the HR-pQCT scan (Fig. 12d and 12d). Therefore, all 168 slices were summed, where the tracked periosteal and endosteal bone interfaces are in agreement with the summed HR-pQCT scans. However, a bias occurred at outer endosteal surfaces due to an increased curvature and bone thickness.
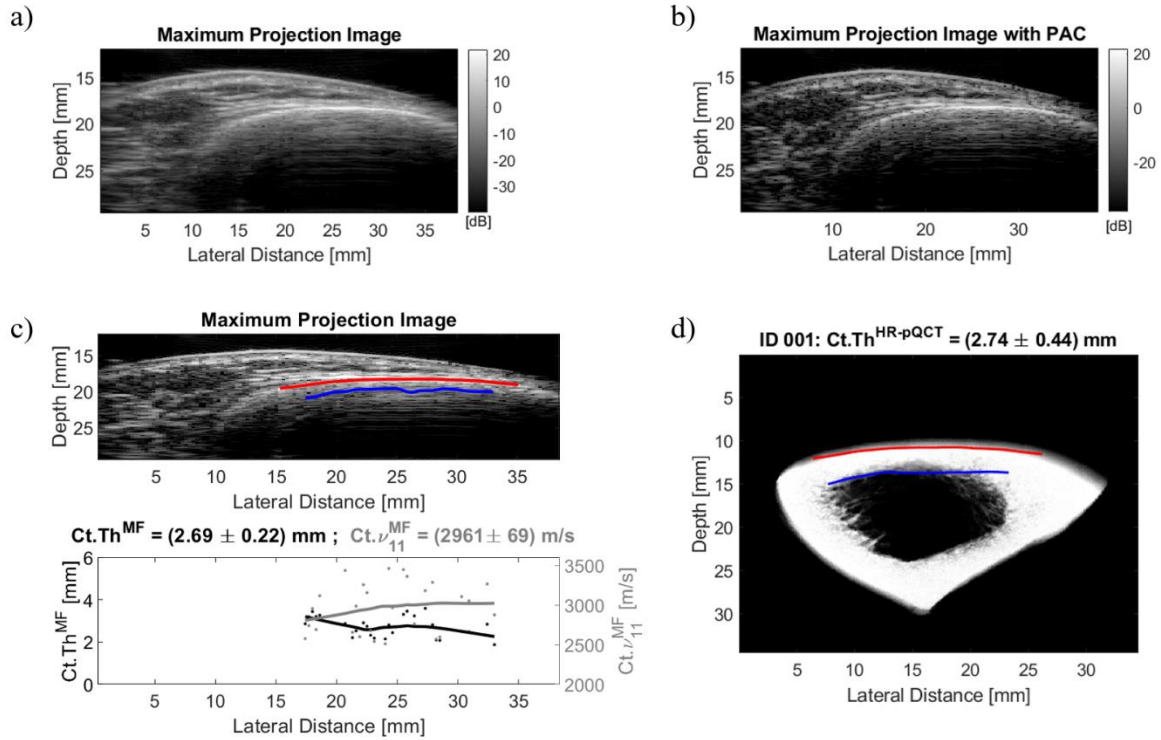
Fig. 12: a) Maximum projection image of patient ID001 from all focus depths with conventional delay and sum beamforming. b) Maximum projection B-mode image reconstructed from all focus depths with phase aberration methods (surface geometry time shift, autocorrelation function and cross-correlation corrections). c) Maximum projection B-mode image with a tracked periosteal and endosteal bone interface (below) and representative plots of $Ct.Th^{MF}(x_i)$ and $Ct.v_{11}^{MF}(x_i)$. The dots show the estimated $Ct.Th^{MF}$ and $Ct.v_{11}^{MF}$ for the individual array position. The straight lines indicate the retrieved $Ct.Th^{MF}$ and $Ct.v_{11}^{MF}$ based on a moving average filter. Smoothed data were used to calculate means and standard deviations. For $Ct.Th^{MF}$ and $Ct.v_{11}^{MF}$ estimation a total of 27 scan position was found. d) Summed HR-pQCT scan slices with the tracked periosteal and endosteal bone interfaces from the MF measurement.

From 55 patients, two patients were excluded from the statistics of Ct.Th. One patient had strong motion artifacts on the HR-pQCT scan (Fig. 13 note by a red circle), so the reference $Ct.Th^{Ref}$ was not reliable. The other patient showed a small thickness value on the HR-pQCT scan with $Ct.Th^{Ref} = (0.99 \pm 0.83)$ mm with high SD (Fig. 13 a red cross). Front- and backside reflections of cortical bones below 1 mm can overlap due to high porosity and the precise and accurate estimation of $Ct.Th^{MF}$ is then problematic. Accuracy and precision for the 53 out of 55 patients were 0.17 mm and 6.03% for $Ct.Th^{MF}$. The linear regression of the derived $Ct.Th^{MF}$ compared to the reference HR-pQCT $Ct.Th^{Ref}$ showed a strong agreement (Fig. 13b).
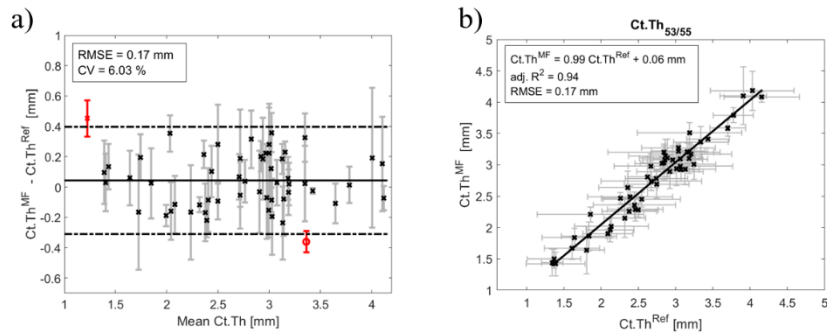
Fig. 13: a) Bland-Altman plot of Ct.Th^{MF} versus Ct.Th^{Ref}. The two outliers are marked in red. One patient had strong motion artifacts on HR-pQCT scans (red circle) and one patient had a Ct.Th^{Ref} smaller than 1 mm (red cross). Both patients were excluded from accuracy and precision estimation and linear regression. b) Derived Ct.Th compared to Ct.Th^{Ref} from HR-pQCT with linear regression (black line) without the two outliers from the Bland-Altmann plot.

Fragility fracture discrimination

In addition to the fragility fracture discrimination performance analyses for CortBS parameters reported in Study C (81), MF parameters were added. The results of discrimination performance analyses using PLS-LOOCV are summarized in Figure 14 and Table 3. For vertebral and all other fractures, additional MF parameters to the CortBS parameters resulted in the same AUC values and the same significant CortBS variables for fracture discrimination (Tab. 3). A slightly higher AUC value of 0.79 was obtained after PLS-LOOCV using CortBS and MF parameters without using anthropometric information for vertebral fractures (Fig. 14a, purple line). Note, only CortBS parameters were selected as significant variables. For other fractures the combination of MF and CortBS parameters resulted in one additional significant variable, the median cortical speed of sound Ct.$v_{11}^{MF}{}_{mean}$. Nevertheless, AUC values remained the same. For all three fracture cases, MF parameters alone showed poor discrimination performance. In summary, MF parameters could not further improve the CortBS discrimination model. The CortBS parameters provided superior fracture discrimination performance compared with DXA and similar fracture discrimination performance compared with HR-pQCT (81).

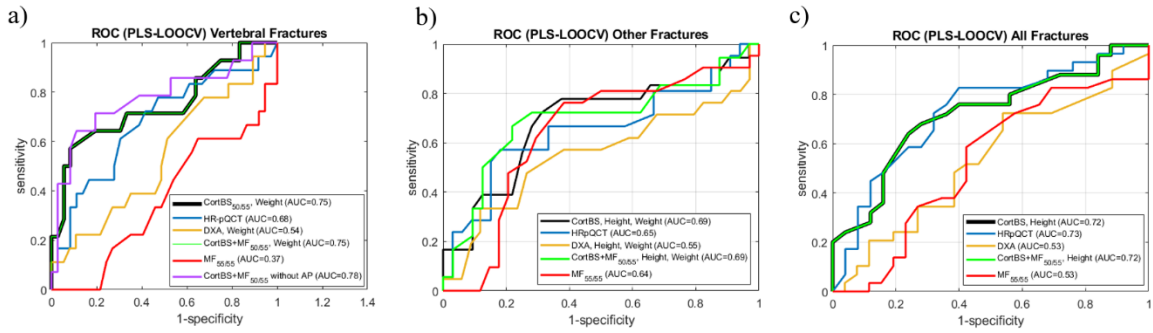**Fig. 14**: Fragility fracture discrimination performance of DXA, HR-pQCT, CortBS, MF and combination of CortBS+MF for a) vertebral fractures, b) other fractures, and c) all fractures. If anthropometric information improved the discrimination model, these ROC curves are shown (extended from Armbrecht et al. (81) with MF results with permission under Creative Commons 4.0 license).

Tab. 3: "Fragility Fracture Discrimination performance. PLS-LOOC discrimination models were developed for the individual measurement modalities both alone and in combination with anthropometric (AP) data and age. Only significant models are listed. The numbers of fractured/non-fractured cases for each model are found in the first column inside of the parenthesis. Significant variables selected by Subwindow Permutation Analysis are listed in the last column." (81) (This Table is extended from Armbrecht et al. (81) with MF results with permission under Creative Commons 4.0 license).

	Sensiti-vity	Specifi-city	AUC	Accuracy	Odds Ratio (95% Confidence Intervals)	Significant Variables
Vertebral Fractures (Fx/nFx)						
DXA + AP (11/36)	0.11	0.94	0.54	0.67	2.2 (0.1 – 4.2)	T-score$_{Femur}$ Weight
HR-pQCT (18/36)	0.27	0.92	0.68	0.70	4.2 (2.7 - 5.8)	Ct.Po.D$_{SD(ROI)}$ Ct.Po.D$_{VAR(ROI)}$ Ct.Po.Dm.D$_{Mean(ROI)}$ Ct.Po.Dm.D$_{SD(ROI)}$ Ct.Po.Dm.D$_{Q90(ROI)}$
MF (18/36)	0	1	0.37	0.67	-	Ct.v$_{11}^{MF}_{median}$ Ct.v$_{11}^{MF}_{mean}$ Ct.Th^{MF}$_{median}$ Ct.Th^{MF}$_{mean}$ Ct.Th^{MF}$_{median}$ / Ct.v$_{11}^{MF}_{median}$ Ct.Th^{MF}$_{mean}$ / Ct.v$_{11}^{MF}_{mean}$ Ct.v$_{11}^{MF}_{median}$ /Ct.Th^{MF}$_{median}$ Ct.v$_{11}^{MF}_{mean}$ / Ct.Th^{MF}$_{mean}$
CortBS (14/36)	0.43	0.92	0.72	0.78	8.2 (6.7 – 9.8)	Ct.Po.Dm.D$_{Q90}$ Ct.Po.Dm.D$_{FWHM}$ Ct.Po.Dm.D$_{FWHM-Max}$ Ct.α_0, Ct.α_f
CortBS + MF (14/36)	0.50	0.92	0.78	0.80	11 (9.4 – 12.6)	Ct.Po.Dm.D$_{FWHM}$ Ct.α_0, Ct.α_f
CortBS + AP (14/36)	0.50	0.94	0.75	0.82	17.0 (15.2 - 18.8)	Ct.Po.Dm.D$_{Q90}$ Ct.Po.Dm.D$_{FWHM}$ Ct.α_0, Ct.α_f Weight
CortBS + MF + AP (14/36)	0.50	0.94	0.75	0.82	17.0 (15.2 - 18.8)	Ct.Po.Dm.D$_{Q90}$ Ct.Po.Dm.D$_{FWHM}$ Ct.α_0, Ct.α_f Weight

Other Fractures (Fx/nFx)

DXA + AP (15/34)	0.33	0.85	0.55	0.65	2.9 (1.6 – 4.2)	$T\text{-score}_{Femur}$ Height, Weight
HR-pQCT (15/33)	0.48	0.85	0.66	0.70	5.1 (3.8-6.4)	$Ct.Po_{BH(ROI)}$ $Ct.Po.D_{skewness(ROI)}$ $Ct.Po.Dn_{(ROI)}$ $Ct.Po_{BH(Full)}$ $Ct.Po.D_{skewness(Full)}$ $Ct.Po.D_{kurtosis(Full)}$ $T.Tb.Th_{(Full)}$
CortBS (12/32)	0.39	0.81	0.65	0.66	2.76 (1.5-4.1)	$Ct.\alpha_0$, $Ct.\alpha_f$
MF (15/34)	0.10	0.85	0.64	0.56	0.6 (-1.1-2.3)	$Ct.v_{11}{}^{MF}{}_{mean}$
MF+AP (15/34)	0.29	0.79	0.59	0.60	1.54 (0.28-2.80)	Weight Height $Ct.v_{11}{}^{MF}{}_{median}$ $Ct.v_{11}{}^{MF}{}_{mean}$
CortBS + MF (12/32)	0.39	0.81	0.66	0.66	2.78 (1.5-4.1)	$Ct.\alpha_0$, $Ct.\alpha_f$
CortBS + AP (12/32)	0.39	0.88	0.69	0.70	4.45 (3.0-5.9)	$Ct.\alpha_0$, $Ct.\alpha_f$ Height Weight
CortBS + MF + AP (12/32)	0.33	0.88	0.69	0.68	3.5 (2.07-4.93)	$Ct.\alpha_0$ $Ct.\alpha_f$ Height Weight $Ct.v_{11}{}^{MF}{}_{median}$

All Fractures (Fx/nFx)

HR-pQCT (29/26)	0.83	0.64	0.73	0.74	8.5 (7.3-9.8)	$Ct.Po.D_{Q90(ROI)}$ $Ct.Po.D_{skewness(Full)}$
CortBS (29/25)	0.68	0.64	0.70	0.66	3.8 (2.6-4.9)	$Ct.PoDm.D_{Peak}$ $Ct.PoDm.D_{Q10}$ $Ct.PoDm.D_{Q90}$ $Ct.PoDm.D_{FWHM-Min}$ $Ct.PoDm.D_{FWHM-Max}$ $Ct.\alpha_0$ $Ct.\alpha_f$
MF (29/26)	0.66	0.50	0.53	0.58	1.90 (0.81-2.99)	$Ct.v_{11}{}^{MF}{}_{median}$ $Ct.v_{11}{}^{MF}{}_{mean}$
MF+AP (29/26)	0.66	0.50	0.53	0.58	1.90 (0.81-2.99)	$Ct.v_{11}{}^{MF}{}_{median}$ $Ct.v_{11}{}^{MF}{}_{mean}$
CortBS + MF (29/25)	0.64	0.60	0.69	0.62	2.7 (1.5-3.8)	$Ct.\alpha_0$ $Ct.\alpha_f$ $Ct.v_{11}{}^{MF}{}_{median}$
CortBS + AP (29/25)	0.72	0.64	0.72	0.68	4.6 (3.4-5.8)	$Ct.\alpha_0$ $Ct.\alpha_f$ Height
CortBS + MF + AP (29/25)	0.72	0.64	0.72	0.68	4.6 (3.4-5.8)	$Ct.\alpha_0$ $Ct.\alpha_f$ Height

4. Discussion

Study A validated the MF approach in silico and ex vivo on plate-shaped materials as a precise and accurate Ct.Th and $Ct.v_{11}$ estimation. For the transition of the MF method into the in vivo measurements, simulations on curved bone shaped with and without cortical pores were performed in Study B. Additional phase aberration caused by the bone interface curvature, bone tilt and scattering, and cortical pores were corrected using three PAC methods. First, surface time correction was performed by calculating the additional time shift of the propagating waves caused by the curvature. Second, the autocorrelation function correction was applied by correcting the tilt wave front of the reflected backside echoes caused by the bone tilt. Lastly, cross correlation between the reflected backside echoes were used to retrieve the confocal backside focus depth. Thickness and speed of sound estimations using the MF post-processing analysis from Study A were not in agreement with reference values. In contrast, using the three PAC methods from Study B, estimations of $Ct.Th^{MF}$ showed precision and accuracy values of 0.25 mm and 5.67%, respectively, and precision and accuracy values for $Ct.v_{11}^{MF}$ were 114.9 m/s and 9.77%, respectively (78). In summary, without phase aberration corrections, the MF methods fails on precise and accurate estimation of Ct.Th and $Ct.v_{11}$ on curved and real bone structures. Another approach that used similar refraction methods with multiple focus depths was proposed by Wydra et al. (93). A 2.5-MHz single-element focused transducer was used to assess thickness and speed of sound on porous plate-shaped bone phantoms of human skulls. Precision values were reported for thickness at 8.5% and for speed of sound at 4.1%. In comparison to their precision values of pore-free plate shaped samples, the precision values from Study A are approximately 50% higher. Renaud et al. (66) proposed another measurement method to retrieve Ct.Th and $Ct.v_{11}$ using a single-element excitation with a 2.5-MHz linear phased array transducer. The method is based on an adaptation of the Kirchhoff migration to reconstruct ultrasound images. Kirchhoff migration was originally developed to image the earth's subsurface. The ultrasound technique proposed by Renaud et al. showed accurate estimation of cortical bone thickness of two healthy volunteers (66). In contrast, the MF method includes an effective aperture considering conversion of compressional waves into shear waves. In addition, the MF approach uses phase aberration correction methods caused by surface geometry and cortical pores. The effect of the focused beam size to the effective aperture should be a target for future studies.

The in vivo estimations of $Ct.Th^{MF}$ for the 53 out of 55 female patients were in agreement with the reference HR-pQCT method with accuracy and precision values of 0.17 mm and 6.03% for $Ct.Th^{MF}$, respectively. In addition, in vivo estimations of $Ct.v_{11}^{MF}$ were in the range of reported speed of sound values for Ct.Po up to 20% (77). This shows that the MF approach can be used for in vivo thickness and speed of sound estimation. However, future studies should target real bone structures to establish appropriate phase aberration for osteoporotic bones. The proposed phase aberration method in Study A and B were only based on simulation results of simplified bone models. Osteoporotic cortical bones show a highly irregular endosteal interface and large cortical pores, where backside reflections diminish throughout due to strong scattering. In addition, the effect for the speed of sound in soft tissue needs to be investigated further to validate the in vivo application on more subjects. In Study C, an average speed of sound value of soft tissue of 1540 m/s was used. Goss et al. (94) have shown that speed of sound values vary up to 10% depending on the composition of soft tissue i.e. fat, muscles, blood etc., which results in additional wave distortion. The ultrasound beam would be diffracted and attenuated by layers of soft tissue and fat. Therefore, received ultrasound waves from the bone interface would be absorbed and the information about the bone structure would be diminished during the wave interaction with soft tissue. A speed of sound measurement of overlaying tissues using ultrasound imaging and an autofocused approach was proposed by Renaud et al. (95). In conclusion, the effect of highly irregular endosteal interface and soft tissue on the ultrasound signal simulation models using real bone structures based on HR-pQCT scan should be further investigated.

During the development of the MF approach, another QUS method was introduced to assess cortical pore diameter distribution by evaluating cortical backscatter (CortBS method) (68). The first in vivo assessments of cortical pore diameter distributions of postmenopausal women showed the good discrimination performance of CortBS ($0.69 \leq AUC \leq 0.75$) compared to DXA ($0.54 \leq AUC \leq 0.55$) and similar discrimination performance compared to HR-pQCT ($0.66 \leq AUC \leq 0.73$) (81). In addition to the CortBS method, the MF approach provides Ct.Th values and viscoelastic property information of the cortical bone from the $Ct.v_{11}$ values. No improvement in the discrimination performance using only the MF parameter was found. The Ct.Th at the tibia midshaft was not a significant variable in this in vivo study, but cortical porosity and pore-size distributions from the CortBS method showed good association with

fragility fractures. For non-vertebral fractures, the combination of CortBS and MF resulted in an additional significant viscoelastic parameter of $Ct.v_{11}{}^{MF}{}_{median}$ for other fracture discrimination after PLS-LOOCV. For vertebral fractures, MF parameters were not significant. In summary, MF parameters could not further improve the CortBS discrimination model. Nevertheless, further studies with a larger study population needs to be performed to obtain statistically robust results. In Study C, PLS-LOOCV was performed with prediction parameter matrices of up to 25 parameters for CortBS and MF on a small cohort size of 55 patients, which resulted in the uncertainty for the selection of significant variables. One example is shown in Figure 14 a (purple curve), where the combination of CortBS and MF parameters without anthropometric data and age resulted in a higher AUC value of 0.79 compared to the AUC value of 0.75, where anthropometric data and age were included. Significant variables were only in CortBS parameters, whereas $Ct.Po.Dm.D_{Q90}$ was not selected as significant variable for CortBS+MF PLS-LOOCV without anthropometric data and age. Another limitation of the in vivo study was the restriction to postmenopausal women with T-scores below -1. Therefore, larger population studies including both sexes with a larger age range, larger BMI, and T-score above -1 would improve stable statistical results (81). Nevertheless, CortBS parameters showed superior discrimination performance. In the future, studies should focus on identifying people at risk of fracture as well as assessing the individual fracture risk with MF and CortBS parameters (81). In addition, real-time detection of the periosteal and endosteal surface of the cortical bone surface should be implemented for MF measurements as real-time feedback for a successful measurement.

In conclusion, this work demonstrates a refraction and phase aberration corrected imaging method that locally resolves the estimation of cortical thickness and speed of sound values at the tibia using a clinical ultrasound scanner. The understanding of ultrasound scattering at soft tissue and the effect of speed of sound values for soft tissue compartments requires investigations in further studies to enable a successful clinical application of the MF method for cortical thickness and speed of sound estimations. The first in vivo estimation of cortical pore properties that quantifies microstructural cortical bone deteriorations from cortical backscatter showed better discrimination performance compared to the standard aBMD. The Multifocus and CortBS techniques are anticipated to have high clinical potential as a low-cost, non-

invasive, non-ionizing and portable imaging tool for fracture risk assessment. Using these techniques, it is possible to identify those at increased risk early on.

References

1. Rodan GA, Rodan SB. The Cells of Bone. in Osteoporosis: Etiology, Diagnosis, and Management, edited by BL Riggs, LJ Melton III, 2nd ed. Lippincot-Raven Publishers, Philadelphia, pp. 1-39. 1995.
2. Ott SM. Cortical or Trabecular Bone: What's the Difference? Am J Nephrol. 2018;47(6):373-5.
3. Katsimbri P. The biology of normal bone remodelling. Eur J Cancer Care (Engl). 2017;26(6).
4. Mehrsheed S. Osteoporosis in Braddom's Physical Medicine and Rehabilitation (Sixth Edition), edited by David X. Cifu, Elsevier 2021, pp 690-714, ISBN 9780323625395. 2021.
5. Zebaze R, Seeman E. Cortical bone: a challenging geography. J Bone Miner Res. 2015;30(1):24-9.
6. Laugier P, Haiat G. Bone Quantitative Ultrasound. Spinger. 2011:p.52-3.
7. Zebaze RM, Ghasem-Zadeh A, Bohte A, Iuliano-Burns S, Mirams M, Price RI, Mackie EJ, Seeman E. Intracortical remodelling and porosity in the distal radius and post-mortem femurs of women: a cross-sectional study. Lancet. 2010;375(9727):1729-36.
8. Bala Y, Zebaze R, Seeman E. Role of cortical bone in bone fragility. Curr Opin Rheumatol. 2015;27(4):406-13.
9. Chen H, Zhou X, Shoumura S, Emura S, Bunai Y. Age- and gender-dependent changes in three-dimensional microstructure of cortical and trabecular bone at the human femoral neck. Osteoporos Int. 2010;21(4):627-36.
10. Johnell O, Kanis JA. An estimate of the worldwide prevalence and disability associated with osteoporotic fractures. Osteoporosis Int. 2006;17(12):1726-33.
11. Wylie CD. Setting a standard for a "silent" disease: defining osteoporosis in the 1980s and 1990s. Stud Hist Philos Biol Biomed Sci. 2010;41(4):376-85.
12. Braddom RL, Chan L, Harrast MA. Physical medicine and rehabilitation. Philadelphia, PA: Saunders/Elsevier. 2011.
13. World Health Organization. Assessment of fracture risk and its application to screening for postmenopausal osteoporosis: report of a WHO study group. WHO technical report series 843. 1994.
14. Hernlund E, Svedbom A, Ivergard M, Compston J, Cooper C, Stenmark J, McCloskey EV, Jonsson B, Kanis JA. Osteoporosis in the European Union: medical management, epidemiology and economic burden. A report prepared in collaboration with the International Osteoporosis Foundation (IOF) and the European Federation of Pharmaceutical Industry Associations (EFPIA). Arch Osteoporos. 2013;8:136.
15. Blake GM, Fogelman I. The role of DXA bone density scans in the diagnosis and treatment of osteoporosis. Postgrad Med J. 2007;83(982):509-17.
16. Avioli LV. The Osteoporotic Syndrome: Detection, Prevention, and Treatment. 4th ed. San Diego: Academic Press. 2000.
17. Howard GA, Schiller PC. Biology of Bone. Biology of bone. In Osteoporosis in Older Persons: Advances in Pathophysiology and Therapeutic Approaches: Second Edition (pp. 1-21). Springer International Publishing. 2016. https://doi.org/10.1007/978-3-319-25976-5_1.
18. Cummings SR, Melton LJ. Epidemiology and outcomes of osteoporotic fractures. Lancet. 2002;359(9319):1761-7.
19. Reginster JY, Burlet N. Osteoporosis: a still increasing prevalence. Bone. 2006;38(2 Suppl 1):S4-9.
20. Schuit SCE, van der Klift M, Weel AEAM, de Laet CEDH, Burger H, Seeman E, Hofman A, Uitterlinden AG, van Leeuwen JPTM, Pols HAP. Fracture incidence and association with bone mineral density in elderly men and women: the Rotterdam Study. Bone. 2004;34(1):195-202.

21. Waugh EJ, Lam MA, Hawker GA, McGowan J, Papaioannou A, Cheung AM, Hodsman AB, Leslie WD, Siminoski K, Jamal SA. Risk factors for low bone mass in healthy 40-60 year old women: A systematic review of the literature. Osteoporosis Int. 2009;20(1):1-21.
22. Kanis JA. Diagnosis of osteoporosis and assessment of fracture risk. Lancet. 2002;359(9321):1929-36.
23. Lips P. Epidemiology and predictors of fractures associated with osteoporosis. Am J Med. 1997;103(2A):3S-8S; discussion S-11S.
24. Siris ES, Chen YT, Abbott TA, Barrett-Connor E, Miller PD, Wehren LE, Berger ML. Bone mineral density thresholds for pharmacological intervention to prevent fractures. Arch Intern Med. 2004;164(10):1108-12.
25. Seeman E. Growth in bone mass and size - Are racial and gender differences in bone mineral density more apparent than real? J Clin Endocr Metab. 1998;83(5):1414-9.
26. Bhudhikanok GS, Wang MC, Eckert K, Matkin C, Marcus R, Bachrach LK. Differences in bone mineral in young Asian and Caucasian Americans may reflect differences in bone size. J Bone Miner Res. 1996;11(10):1545-56.
27. Hans D, Baim S. Quantitative Ultrasound (QUS) in the Management of Osteoporosis and Assessment of Fracture Risk. J Clin Densitom. 2017;20(3):322-33.
28. Kanis JA, Johnell O, Oden A, Johansson H, McCloskey E. FRAX and the assessment of fracture probability in men and women from the UK. Osteoporos Int. 2008;19(4):385-97.
29. Kanis JA, Harvey NC, Cooper C, Johansson H, Oden A, McCloskey EV, Advisory Board of the National Osteoporosis Guideline G. A systematic review of intervention thresholds based on FRAX : A report prepared for the National Osteoporosis Guideline Group and the International Osteoporosis Foundation. Arch Osteoporos. 2016;11(1):25.
30. Kanis JA, Cooper C, Rizzoli R, Reginster JY, Scientific Advisory Board of the European Society for C, Economic Aspects of O, the Committees of Scientific A, National Societies of the International Osteoporosis F. European guidance for the diagnosis and management of osteoporosis in postmenopausal women. Osteoporos Int. 2019;30(1):3-44.
31. Cummins NM, Poku EK, Towler MR, O'Driscoll OM, Ralston SH. clinical risk factors for osteoporosis in Ireland and the UK: a comparison of FRAX and QFractureScores. Calcif Tissue Int. 2011;89(2):172-7.
32. Prevrhal S, Engelke K, Genant HK. Peripheral Quantitative Computed Tomography. In: Grampp S, editor. Radiology of Osteoporosis. Berlin, Heidelberg: Springer Berlin Heidelberg; 2003. p. 115-29.
33. Laib A, Hammerle S, Koller B. A new 100 µm resolution scanner for in vivo 3D-CT of the human forearm and lower leg. 6th International Bone Densitometry Workshop, Annecy, France. 2004.
34. Mikolajewicz N, Bishop N, Burghardt AJ, Folkestad L, Hall A, Kozloff KM, Lukey PT, Molloy-Bland M, Morin SN, Offiah AC, Shapiro J, van Rietbergen B, Wager K, Willie BM, Komarova SV, Glorieux FH. HR-pQCT Measures of Bone Microarchitecture Predict Fracture: Systematic Review and Meta-Analysis. J Bone Miner Res. 2020;35(3):446-59.
35. Iori G, Schneider J, Reisinger A, Heyer F, Peralta L, Wyers C, Graesel M, Barkmann R, Glueer CC, van den Bergh JP, Pahr D, Raum K. Large cortical bone pores in the tibia are associated with proximal femur strength. Plos One. 2019;14(4).
36. Zebaze R, Ghasem-Zadeh A, Mbala A, Seeman E. A new method of segmentation of compact-appearing, transitional and trabecular compartments and quantification of cortical porosity from high resolution peripheral quantitative computed tomographic images. Bone. 2013;54(1):8-20.
37. Kazakia GJ, Hyun B, Burghardt AJ, Krug R, Newitt DC, de Papp AE, Link TM, Majumdar S. In vivo determination of bone structure in postmenopausal women: a comparison of HR-pQCT and high-field MR imaging. J Bone Miner Res. 2008;23(4):463-74.
38. Patsch JM, Burghardt AJ, Kazakia G, Majumdar S. Noninvasive imaging of bone microarchitecture. Ann N Y Acad Sci. 2011;1240:77-87.

39. Li C, Seifert AC, Rad HS, Bhagat YA, Rajapakse CS, Sun W, Lam SC, Wehrli FW. Cortical bone water concentration: dependence of MR imaging measures on age and pore volume fraction. Radiology. 2014;272(3):796-806.

40. Krug R, Carballido-Gamio J, Burghardt AJ, Kazakia G, Hyun BH, Jobke B, Banerjee S, Huber M, Link TM, Majumdar S. Assessment of trabecular bone structure comparing magnetic resonance imaging at 3 Tesla with high-resolution peripheral quantitative computed tomography ex vivo and in vivo. Osteoporos Int. 2008;19(5):653-61.

41. Wear KA, Hoffmeister BK, Laugier P. Quantitative Ultrasound and the Management of Osteoporosis. Acoustics Today. 2018. Available: https://acousticstoday.org/quantitative-ultrasound-management-osteoporosis-keith-wear/. Accessed 04 Jan 2022;14.

42. Hans D, Dargent-Molina P, Schott AM, Sebert JL, Cormier C, Kotzki PO, Delmas PD, Pouilles JM, Breart G, Meunier PJ. Ultrasonographic heel measurements to predict hip fracture in elderly women: the EPIDOS prospective study. Lancet. 1996;348(9026):511-4.

43. Hans D, Downs RW, Jr., Duboeuf F, Greenspan S, Jankowski LG, Kiebzak GM, Petak SM, International Society for Clinical D. Skeletal sites for osteoporosis diagnosis: the 2005 ISCD Official Positions. J Clin Densitom. 2006;9(1):15-21.

44. Marin F, Gonzalez-Macias J, Diez-Perez A, Palma S, Delgado-Rodriguez M. Relationship between bone quantitative ultrasound and fractures: a meta-analysis. J Bone Miner Res. 2006;21(7):1126-35.

45. Moayyeri A, Adams JE, Adler RA, Krieg MA, Hans D, Compston J, Lewiecki EM. Quantitative ultrasound of the heel and fracture risk assessment: an updated meta-analysis. Osteoporos Int. 2012;23(1):143-53.

46. Krieg MA, Barkmann R, Gonnelli S, Stewart A, Bauer DC, Del Rio Barquero L, Kaufman JJ, Lorenc R, Miller PD, Olszynski WP, Poiana C, Schott AM, Lewiecki EM, Hans D. Quantitative ultrasound in the management of osteoporosis: the 2007 ISCD Official Positions. J Clin Densitom. 2008;11(1):163-87.

47. Karjalainen J, Riekkinen O, Toyras J, Kroger H, Jurvelin J. Ultrasonic assessment of cortical bone thickness in vitro and in vivo. IEEE Trans Ultrason Ferroelectr Freq Control. 2008;55(10):2191-7.

48. Greenfield MA, Craven JD, Huddleston A, Kehrer ML, Wishko D, Stern R. Measurement of the velocity of ultrasound in human cortical bone in vivo. Estimation of its potential value in the diagnosis of osteoporosis and metabolic bone disease. Radiology. 1981;138(3):701-10.

49. Singh S. Ultrasonic non-destructive measurements of cortical bone thickness in human cadaver femur. Ultrasonics. 1989;27(2):107-13.

50. Hans D, Metrailler A, Rodriguez EG, Lamy O, Shevroja E. Quantitative Ultrasound (QUS) in the Management of Osteoporosis and Assessment of Fracture Risk: An Update. Adv Exp Med Biol. 2022;1364:7-34.

51. Bossy E, Talmant M, Laugier P. Effect of bone cortical thickness on velocity measurements using ultrasonic axial transmission: a 2D simulation study. J Acoust Soc Am. 2002;112(1):297-307.

52. Dobnig H, Piswanger-Solkner JC, Obermayer-Pietsch B, Tiran A, Strele A, Maier E, Maritschnegg P, Riedmuller G, Brueck C, Fahrleitner-Pammer A. Hip and nonvertebral fracture prediction in nursing home patients: role of bone ultrasound and bone marker measurements. J Clin Endocrinol Metab. 2007;92(5):1678-86.

53. Roggen I, Louis O, Van Biervliet S, Van Daele S, Robberecht E, De Wachter E, Malfroot A, De Waele K, Gies I, Vanbesien J, De Schepper J. Quantitative bone ultrasound at the distal radius in adults with cystic fibrosis. Ultrasound Med Biol. 2015;41(1):334-8.

54. Shenoy S, Chawla JK, Gupta S, Sandhu JS. Prevalence of low bone health using quantitative ultrasound in Indian women aged 41-60 years: Its association with nutrition and other related risk factors. J Women Aging. 2017;29(4):334-47.

55. Hans D, Srivastav SK, Singal C, Barkmann R, Njeh CF, Kantorovich E, Gluer CC, Genant HK. Does combining the results from multiple bone sites measured by a new quantitative

ultrasound device improve discrimination of hip fracture? J Bone Miner Res. 1999;14(4):644-51.

56. Barkmann R, Kantorovich E, Singal C, Hans D, Genant HK, Heller M, Gluer CC. A new method for quantitative ultrasound measurements at multiple skeletal sites: first results of precision and fracture discrimination. J Clin Densitom. 2000;3(1):1-7.

57. Njeh CF, Saeed I, Grigorian M, Kendler DL, Fan B, Shepherd J, McClung M, Drake WM, Genant HK. Assessment of bone status using speed of sound at multiple anatomical sites. Ultrasound Med Biol. 2001;27(10):1337-45.

58. Talmant M, Kolta S, Roux C, Haguenauer D, Vedel I, Cassou B, Bossy E, Laugier P. In vivo performance evaluation of bi-directional ultrasonic axial transmission for cortical bone assessment. Ultrasound Med Biol. 2009;35(6):912-9.

59. Weiss M, Ben-Shlomo A, Hagag P, Ish-Shalom S. Discrimination of proximal hip fracture by quantitative ultrasound measurement at the radius. Osteoporos Int. 2000;11(5):411-6.

60. Nguyen TV, Center JR, Eisman JA. Bone mineral density-independent association of quantitative ultrasound measurements and fracture risk in women. Osteoporos Int. 2004;15(12):942-7.

61. Foiret J, Minonzio JG, Chappard C, Talmant M, Laugier P. Combined estimation of thickness and velocities using ultrasound guided waves: a pioneering study on in vitro cortical bone samples. IEEE Trans Ultrason Ferroelectr Freq Control. 2014;61(9):1478-88.

62. Minonzio JG, Bochud N, Vallet Q, Ramiandrisoa D, Etcheto A, Briot K, Kolta S, Roux C, Laugier P. Ultrasound-Based Estimates of Cortical Bone Thickness and Porosity Are Associated With Nontraumatic Fractures in Postmenopausal Women: A Pilot Study. J Bone Miner Res. 2019;34(9):1585-96.

63. Vallet Q, Bochud N, Chappard C, Laugier P, Minonzio JG. In Vivo Characterization of Cortical Bone Using Guided Waves Measured by Axial Transmission. IEEE Trans Ultrason Ferroelectr Freq Control. 2016;63(9):1361-71.

64. Schneider J, Ramiandrisoa D, Armbrecht G, Ritter Z, Felsenberg D, Raum K, Minonzio JG. In Vivo Measurements of Cortical Thickness and Porosity at the Proximal Third of the Tibia Using Guided Waves: Comparison with Site-Matched Peripheral Quantitative Computed Tomography and Distal High-Resolution Peripheral Quantitative Computed Tomography. Ultrasound Med Biol. 2019;45(5):1234-42.

65. Moilanen P, Talmant M, Kilappa V, Nicholson P, Cheng S, Timonen J, Laugier P. Modeling the impact of soft tissue on axial transmission measurements of ultrasonic guided waves in human radius. J Acoust Soc Am. 2008;124(4):2364-73.

66. Renaud G, Kruizinga P, Cassereau D, Laugier P. In vivo ultrasound imaging of the bone cortex. Phys Med Biol. 2018;63(12):125010.

67. Etgen J, Gray SH, Zhang Y. An overview of depth imaging in exploration geophysics. Geophysics. 2009;74(6):Wca5-Wca17.

68. Iori G, Du J, Hackenbeck J, Kilappa V, Raum K. Estimation of Cortical Bone Microstructure From Ultrasound Backscatter. IEEE Trans Ultrason Ferroelectr Freq Control. 2021;68(4):1081-95.

69. Wang SF, Chang CY, Shih C, Teng MM. Evaluation of tibial cortical bone by ultrasound velocity in oriental females. Br J Radiol. 1997;70(839):1126-30.

70. Eneh CT, Malo MK, Karjalainen JP, Liukkonen J, Toyras J, Jurvelin JS. Effect of porosity, tissue density, and mechanical properties on radial sound speed in human cortical bone. Med Phys. 2016;43(5):2030.

71. Eneh CT, Afara IO, Malo MK, Jurvelin JS, Toyras J. Porosity predicted from ultrasound backscatter using multivariate analysis can improve accuracy of cortical bone thickness assessment. J Acoust Soc Am. 2017;141(1):575.

72. Stegman MR, Heaney RP, Traversgustafson D, Leist J. Cortical Ultrasound Velocity as an Indicator of Bone Status. Osteoporosis Int. 1995;5(5):349-53.

73. Aguado F, Revilla M, Villa LF, Rico H. Cortical bone resorption in osteoporosis. Calcif Tissue Int. 1997;60(4):323-6.

74. Raisz LG. Pathogenesis of osteoporosis: concepts, conflicts, and prospects. J Clin Invest. 2005;115(12):3318-25.
75. Szulc P, Seeman E, Duboeuf F, Sornay-Rendu E, Delmas PD. Bone fragility: failure of periosteal apposition to compensate for increased endocortical resorption in postmenopausal women. J Bone Miner Res. 2006;21(12):1856-63.
76. Bossy E, Talmant M, Laugier P. Three-dimensional simulations of ultrasonic axial transmission velocity measurement on cortical bone models. J Acoust Soc Am. 2004;115(5 Pt 1):2314-24.
77. Nguyen Minh H, Du J, Raum K. Estimation of Thickness and Speed of Sound in Cortical Bone Using Multifocus Pulse-Echo Ultrasound. IEEE Trans Ultrason Ferroelectr Freq Control. 2020;67(3):568-79.
78. Nguyen Minh H, Muller M, Raum K. Estimation of Thickness and Speed of Sound for Transverse Cortical Bone Imaging Using Phase Aberration Correction Methods: An In Silico and Ex Vivo Validation Study. Applied Sciences. 2022;12(10):5283.
79. Iori G, Schneider J, Reisinger A, Heyer F, Peralta L, Wyers C, Gluer CC, van den Bergh JP, Pahr D, Raum K. Cortical thinning and accumulation of large cortical pores in the tibia reflect local structural deterioration of the femoral neck. Bone. 2020;137:115446.
80. Luscher SH, Nocciolino LM, Pilot N, Pisani L, Ireland A, Rittweger J, Ferretti JL, Cointry GR, Capozza RF. Differences in the Cortical Structure of the Whole Fibula and Tibia Between Long-Distance Runners and Untrained Controls. Toward a Wider Conception of the Biomechanical Regulation of Cortical Bone Structure. Front Endocrinol (Lausanne). 2019;10:833.
81. Armbrecht G, Nguyen Minh H, Massmann J, Raum K. Pore-Size Distribution and Frequency-Dependent Attenuation in Human Cortical Tibia Bone Discriminate Fragility Fractures in Postmenopausal Women With Low Bone Mineral Density. JBMR Plus. 2021.
82. Hanel V. Measurement of sound velocity and thickness of thin samples by time-resolved acoustic microscopy. J Appl Phys. 1998;84(2):668-70.
83. Maev RG, Levin VM. Principles of local sound velocity and attenuation measurements using transmission acoustic microscope. Ieee T Ultrason Ferr. 1997;44(6):1224-31.
84. Raum K. Quantitative Akustische Rastermikroskopiemethoden zur Charakterisierung der elastischen Eigenschaften von Knochengewebe. PhD Dissertation. 2002;Martin-Luther-Universität Halle-Wittenberg, Germany, 2002.
85. Takano Y, Turner CH, Burr DB. Mineral anisotropy in mineralized tissues is similar among species and mineral growth occurs independently of collagen orientation in rats: Results from acoustic velocity measurements. J Bone Miner Res. 1996;11(9):1292-301.
86. Takano Y, Turner CH, Owan I, Martin RB, Lau ST, Forwood MR, Burr DB. Elastic anisotropy and collagen orientation of osteonal bone are dependent on the mechanical strain distribution. J Orthop Res. 1999;17(1):59-66.
87. Turner CH, Rho J, Takano Y, Tsui TY, Pharr GM. The elastic properties of trabecular and cortical bone tissues are similar: results from two microscopic measurement techniques. Journal of Biomechanics. 1999;32(4):437-41.
88. Chappard C, Bensalah S, Olivier C, Gouttenoire PJ, Marchadier A, Benhamou C, Peyrin F. 3D characterization of pores in the cortical bone of human femur in the elderly at different locations as determined by synchrotron micro-computed tomography images. Osteoporos Int. 2013;24(3):1023-33.
89. Cobbold RSC. Foundations of Biomedical Ultrasound. Oxford University Press. 2006.
90. Agarwal S, Rosete F, Zhang C, McMahon DJ, Guo XE, Shane E, Nishiyama KK. In vivo assessment of bone structure and estimated bone strength by first- and second-generation HR-pQCT. Osteoporos Int. 2016;27(10):2955-66.
91. Iori G, Heyer F, Kilappa V, Wyers C, Varga P, Schneider J, Grasel M, Wendlandt R, Barkmann R, van den Bergh JP, Raum K. BMD-based assessment of local porosity in human femoral cortical bone. Bone. 2018;114:50-61.
92. Li H, Xu Q, Liang Y. An integrated library for partial least squares regression and linear discriminant analysis. Chemometr Intell Lab. May 15 2018:176:34-43.

93. Wydra A, Malyarenko E, Shapoori K, Maev RG. Development of a practical ultrasonic approach for simultaneous measurement of the thickness and the sound speed in human skull bones: a laboratory phantom study. Phys Med Biol. 2013;58(4):1083-102.
94. Goss SA, Johnston RL, Dunn F. Comprehensive compilation of empirical ultrasonic properties of mammalian tissues. J Acoust Soc Am. 1978;64(2):423-57.
95. Renaud G, Clouzet P, Cassereau D, Talmant M. Measuring anisotropy of elastic wave velocity with ultrasound imaging and an autofocus method: application to cortical bone. Phys Med Biol. 2020;65(23):235016.

Eidesstattliche Versicherung

„Ich, Minh Huong Nguyen-Ullrich (geborene Nguyen), versichere an Eides statt durch meine eigenhändige Unterschrift, dass ich die vorgelegte Dissertation mit dem Thema: *Quantification of structural changes in cortical bone by estimating thickness, speed of sound and pore size distribution (Quantifizierung struktureller Veränderungen im kortikalen Knochen durch Abschätzung von Dicke, Schallgeschwindigkeit und Porengrößenverteilung)* selbstständig und ohne nicht offengelegte Hilfe Dritter verfasst und keine anderen als die angegebenen Quellen und Hilfsmittel genutzt habe. Alle Stellen, die wörtlich oder dem Sinne nach auf Publikationen oder Vorträgen anderer Autoren/innen beruhen, sind als solche in korrekter Zitierung kenntlich gemacht. Die Abschnitte zu Methodik (insbesondere praktische Arbeiten, Laborbestimmungen, statistische Aufarbeitung) und Resultaten (insbesondere Abbildungen, Graphiken und Tabellen) werden von mir verantwortet.

Ich versichere ferner, dass ich die in Zusammenarbeit mit anderen Personen generierten Daten, Datenauswertungen und Schlussfolgerungen korrekt gekennzeichnet und meinen eigenen Beitrag sowie die Beiträge anderer Personen korrekt kenntlich gemacht habe (siehe Anteilserklärung). Texte oder Textteile, die gemeinsam mit anderen erstellt oder verwendet wurden, habe ich korrekt kenntlich gemacht.

Meine Anteile an etwaigen Publikationen zu dieser Dissertation entsprechen denen, die in der untenstehenden gemeinsamen Erklärung mit dem/der Erstbetreuer/in, angegeben sind. Für sämtliche im Rahmen der Dissertation entstandenen Publikationen wurden die Richtlinien des ICMJE (International Committee of Medical Journal Editors; www.icmje.og) zur Autorenschaft eingehalten. Ich erkläre ferner, dass ich mich zur Einhaltung der Satzung der Charité – Universitätsmedizin Berlin zur Sicherung Guter Wissenschaftlicher Praxis verpflichte.

Weiterhin versichere ich, dass ich diese Dissertation weder in gleicher noch in ähnlicher Form bereits an einer anderen Fakultät eingereicht habe.

Die Bedeutung dieser eidesstattlichen Versicherung und die strafrechtlichen Folgen einer unwahren eidesstattlichen Versicherung (§§156, 161 des Strafgesetzbuches) sind mir bekannt und bewusst."

Datum   Unterschrift

Anteilserklärung an den erfolgten Publikationen

Ausführliche Anteilserklärung an der erfolgten Publikation als Top-Journal im Rahmen der Promotionsverfahren zum PhD

Huong Nguyen Minh hatte folgenden Anteil an den folgenden Publikationen.

Publikation 1 (Study A): Top-Journal

Nguyen Minh H, Du J, Raum K. Estimation of Thickness and Speed of Sound in Cortical Bone Using Multifocus Pulse-Echo Ultrasound. IEEE Trans Ultrason Ferroelectr Freq Control. 2020;67(3):568-79. Impact Factor: 2.989

Beitrag im Einzelnen:

Maßgeblich verantwortlich für die Multifokus (MF) Methode und Pulse-Echo (PE) Messung mit Hilfe der akustischen Mikroskopie (SAM), sowie Datenauswertung und Interpretation der Ergebnisse unter Supervision durch Prof. Kay Raum

Einleitung/Methodik/Ergebnisse:

- ✓ Durchführung der Literaturrecherche und Auswahl der relevanten Literatur (zusammen mit Co-Autoren)
- ✓ Auswahl der ex vivo Proben, Probenpräparation der Bovinen Knochen
- ✓ Auswahl, Vergleich und Verifikation geeigneter statistischer Methoden unter fachlicher Unterstützung von Prof. Kay Raum.
- ✓ Entwicklung des Messprotokolls für die MF Messung und der PE Messung mit dem SAM für die Referenzmessung mit dem Ziel der Reproduzierbarkeit der Messparameter
- ✓ Implementierung der Multifokus Sequenz auf ein Ultrasonix System zur Datenerfassung (gemeinsam mit Prof. Kay Raum)
- ✓ Durchführung der MF Messung und der PE Messung
- ✓ Anpassung und Optimierung bestehender Auswertungsalgorithmen in Matlab

Diskussion:

- ✓ Interpretation und Diskussion der gewonnen ex vivo Daten mit fachlicher Unterstützung von Prof. Kay Raum

Manuskript:

- ✓ Initialer Entwurf des Manuskripts, außer den Ergebnissen und dem Diskussionsanteil der Simulationsdaten (durch Prof. Kay Raum durchgeführt)
- ✓ Visuelle Aufarbeitung der Methoden und Ergebnisse
- ✓ Erstellung der Graphen: Fig. 2, Fig. 3, Fig. 4, Fig.5, Fig. 8, Fig. 9 wurden von mir erstellt
- ✓ Erstellung der Tabellen: Tab. 1, Tab. 2, Tab. 3 wurden von mir erstellt
- ✓ Eigenständige Überarbeitung auf Basis der Begutachtung von Prof. Kay Raum und im Rahmen des Review-Prozesses

Publikation 2 (Study B):

Nguyen Minh H, Muller M, Raum K. Estimation of Thickness and Speed of Sound for Transverse Cortical Bone Imaging Using Phase Aberration Correction Methods: An In Silico and Ex Vivo Validation Study. Applied Sciences. 2022;12(10):5283. Impact Factor: 2.679

Beitrag im Einzelnen:

Maßgeblich verantwortlich für die Multifokus (MF) Simulationen und Auswertung unter Supervision durch Prof. Kay Raum und Prof. Marie Muller.

Einleitung/Methodik/Ergebnisse:

- ✓ Durchführung der Literaturrecherche und Auswahl der relevanten Literatur (zusammen mit Co-Autoren)
- ✓ Auswahl und Erstellung der MF Simulationen
- ✓ Implementation der MF Methode in das Ultraschall System und Durchführung der ex vivo Messung
- ✓ Auswahl der Korrektur Methoden (PAC) unter fachlicher Unterstützung von Prof. Kay Raum
- ✓ Programmierung der Auswertungsalgorithmen mit Implementierung der PAC Methoden in Matlab unter fachlicher Unterstützung von Prof. Kay Raum

Diskussion:

- ✓ Interpretation und Diskussion der gewonnen Simulationsdaten und ex vivo Messung mit fachlicher Unterstützung von Prof. Kay Raum

Manuskript:

- ✓ Initialer Entwurf des Manuskripts
- ✓ Visuelle Aufarbeitung der Methoden und Ergebnisse
- ✓ Erstellung aller Graphen: Fig. 1 (angepasst von Publikation 1), Fig. 2, Fig. 3 wurden von mir erstellt
- ✓ Erstellung aller Tabellen: Tab. 1, Tab. 2 (angepasst von Publikation 1), Tab. 3, Tab. 4, Tab. 5 wurden von mir erstellt
- ✓ alle Graphen im Appendix wurden von mir erstellt
- ✓ alle Tabellen im Appendix wurden von mir erstellt
- ✓ Eigenständige Überarbeitung auf Basis der Begutachtung von Prof. Kay Raum und Prof. Marie Muller im Rahmen des Review-Prozesses

Publikation 3 (Study C):

Armbrecht G, <u>Nguyen Minh H</u>, Massmann J, Raum K. Pore-Size Distribution and Frequency-Dependent Attenuation in Human Cortical Tibia Bone Discriminate Fragility Fractures in Postmenopausal Women With Low Bone Mineral Density. JBMR Plus. 2021. Impact Factor: 6.284

Beitrag im Einzelnen:

Maßgeblich verantwortlich für die Implementierung der CortBS Methode in das Ultrasonix System, Validierung der definierten Settings an ex vivo Proben vor der Patientenstudie, Erstellung des Messprotokolls für die in vivo Messungen, Training und Aufsicht der Ultraschallmessung mit Dr. Gabriele Armbrecht.

<u>Einleitung/Methodik/Ergebnisse:</u>
- ✓ Implementierung der CortBS Methode in das Ultrasonix System in Zusammenarbeit mit Matthias Jurgk aus Gampt mbH
- ✓ Validierung von Presettings zur optimalen Datenerfassung der CortBS Methode an ex vivo Proben (PMMA und Bovinen Proben) gemeinsam mit Prof. Kay Raum
- ✓ Erstellung des Messprotokolls (SOP) für die in vivo Messungen
- ✓ Training/On-boarding für Dr. Gabriele Armbrecht zur optimalen Ultraschallmessung
- ✓ Durchführung und Aufsicht der CortBS-Messung mit Dr. Gabriele Armbrecht am CBF
- ✓ Durchführung der Datenerfassung für die Reproduzierbarkeit (CortBS short-term precision)
- ✓ Unterstützung der Analyse und Auswertung der HR-pQCT gemeinsam mit Mathis Joachim Manzel
- ✓ Unterstützung der Analyse der Daten für die Reproduzierbarkeit

<u>Manuskript:</u>
- ✓ Begutachtung des Manuskripts

_____

Unterschrift, Datum und Stempel des/der erstbetreuenden Hochschullehrers/in

Unterschrift des Doktoranden/der Doktorandin

Auszug aus der Journal Summary List

Journal Data Filtered By: **Selected JCR Year: 2020** Selected Editions: SCIE,SSCI
Selected Categories: **'ACOUSTICS'** Selected Category Scheme: WoS
Gesamtanzahl: 32 Journale

Rank	Full Journal Title	Total Cites	Journal Impact Factor	Eigenfactor Score
1	ULTRASONICS SONOCHEMISTRY	26,178	7.491	0.021770
2	ULTRASOUND IN OBSTETRICS & GYNECOLOGY	18,164	7.299	0.018820
3	ULTRASCHALL IN DER MEDIZIN	2,911	6.548	0.003340
4	IEEE-ACM Transactions on Audio Speech and Language Processing	4,568	3.919	0.008150
5	JOURNAL OF SOUND AND VIBRATION	41,178	3.655	0.025350
6	JOURNAL OF VIBRATION AND CONTROL	6,405	3.095	0.006790
7	ULTRASOUND IN MEDICINE AND BIOLOGY	12,787	2.998	0.011140
8	ULTRASONICS	8,026	2.890	0.006980
9	JOURNAL OF LOW FREQUENCY NOISE VIBRATION AND ACTIVE CONTROL	1,084	2.837	0.001490
10	IEEE TRANSACTIONS ON ULTRASONICS FERROELECTRICS AND FREQUENCY CONTROL	11,100	2.725	0.006820
11	APPLIED ACOUSTICS	9,042	2.639	0.008530
12	JOURNAL OF ULTRASOUND IN MEDICINE	9,425	2.153	0.008530
13	WAVE MOTION	2,667	2.020	0.002580
14	SPEECH COMMUNICATION	3,575	2.017	0.003190
15	JOURNAL OF THE ACOUSTICAL SOCIETY OF AMERICA	49,404	1.840	0.021990
16	PHONETICA	806	1.759	0.000600

Druckexemplare der ausgewählten Publikationen

Study A: <u>Nguyen Minh H</u>, Du J, Raum K. Estimation of Thickness and Speed of Sound in Cortical Bone Using Multifocus Pulse-Echo Ultrasound. IEEE Trans Ultrason Ferroelectr Freq Control. 2020;67(3):568-79. Impact Factor: 2.989

Estimation of Thickness and Speed of Sound in Cortical Bone Using Multifocus Pulse-Echo Ultrasound

Huong Nguyen Minh, *Member, IEEE*, Juan Du, *Member, IEEE*, and Kay Raum, *Member, IEEE*

Abstract—Most bone loss during the development of osteoporosis occurs in cortical bone at the peripheral skeleton. Decreased cortical thickness (*Ct.Th*) and the prevalence of large pores at the tibia are associated with reduced bone strength at the hip. *Ct.Th* and cortical sound velocity, i.e., a surrogate marker for changes of cortical porosity (*Ct.Po*), are key biomarkers for the identification of patients at high fracture risk. In this study, we have developed a method using a conventional ultrasound array transducer to determine thickness (*Ct.Th*) and the compressional sound velocity propagating in the radial bone direction ($Ct.v_{11}$) using a refraction-corrected multifocus imaging approach. The method was validated *in-silico* on porous bone plate models using a 2-D finite-difference time-domain method and *ex vivo* on plate-shaped plastic reference materials and on plate-shaped cortical bovine tibia samples. Plane-wave pulse-echo measurements provided reference values to assess precision and accuracy of our method. *In-silico* results revealed the necessity to account for inclination-dependent transmission losses at the bone surface. Moreover, the dependence of $Ct.v_{11}$ on both porosity and pore density was observed. *Ct.Th* and $Ct.v_{11}$ obtained *ex vivo* showed a high correlation ($R^2 > 0.99$) with reference values. The *ex-vivo* accuracy and precision for $Ct.v_{11}$ were 29.9 m/s and 0.94%, respectively, and those for *Ct.Th* were 0.04 mm and 1.09%, respectively. In conclusion, this numerical and experimental study demonstrates an accurate and precise estimation of *Ct.Th* and $Ct.v_{11}$. The developed multifocus technique may have high clinical potential to improve fracture risk prediction using noninvasive and nonionizing conventional ultrasound technology with image guidance.

Index Terms—Medical beamforming and beam steering, medical signal and image processing, medical tissue characterization, pulse-echo ultrasound.

I. INTRODUCTION

OSTEOPOROSIS (OP) is one of the most important global health problems of our aging population, which reduces mobility and quality of life, increases mortality,

and sets a dramatic burden on the healthcare system [1]. The current gold standard to predict bone status and fracture risk is the measurement of bone mineral density (BMD) by means of dual-energy X-ray absorptiometry (DXA) at major fracture sites, i.e., spine and proximal femur. These measurement regions are predominantly composed of trabecular bone. However, ~70% of bone loss occurs after age 65 at peripheral sites and is cortical, not trabecular, which contributes ~80% of the human skeleton and contributes most to bone strength [1], [2]. Unbalanced intracortical remodeling leaves progressively more nonrefilled bone multicellular units (BMUs) in the cortex, which becomes thinner and contains particularly large coalescent basic multicellular units (hereinafter called large BMUs) compared with the Haversian canals. In particular, in the endosteal subcompartment, close clustering of BMUs enhances their chances to merge, leading to the so-called trabecularized cortex [2]. Decreased cortical thickness and the prevalence of large BMU's reduce bone strength [3] and are quantifiable "fingerprints" of structural deterioration [4]. However, cortical bone loss and the resulting structural decay are poorly captured by BMD [5]–[7]. In fact, the majority of individuals who have sustained an OP-related fracture or who are at high risk of fracture are not diagnosed as osteoporotic according to the BMD level [1]. In the past three decades, quantitative ultrasound (QUS) methods have been introduced as nonionizing alternatives for the diagnosis of OP and the prediction of fracture risk. While the early QUS approaches have targeted trabecular sites, e.g., at the heel, and aimed at predicting BMD via empirical associations with the measured speed of sound (SOS) and broadband ultrasound attenuation [8], recent QUS technologies target cortical measurement sites, e.g., distal radius and tibia, and aim at the quantitative assessment of structural cortical bone properties, e.g., cortical thickness *Ct.Th* and cortical porosity *Ct.Po*. One approach proposed by Karjalainen *et al.* [9] uses an unfocused single-element pulse-echo configuration to measure the time delay between waves reflected from the periosteal and endosteal bone interfaces. Using the assumption of a known and invariant radial sound velocity of 3565 m/s, the apparent cortical thickness is derived from the time lag between reflections from the periosteal and endosteal interfaces [10]. The time lag can be determined using autocorrelation, envelope peak detection, or cepstral methods [9], [11]. A multivariable optimization approach was proposed by Tasinkevych *et al.* [12] to determine thickness and compressional wave velocity by fitting experimentally
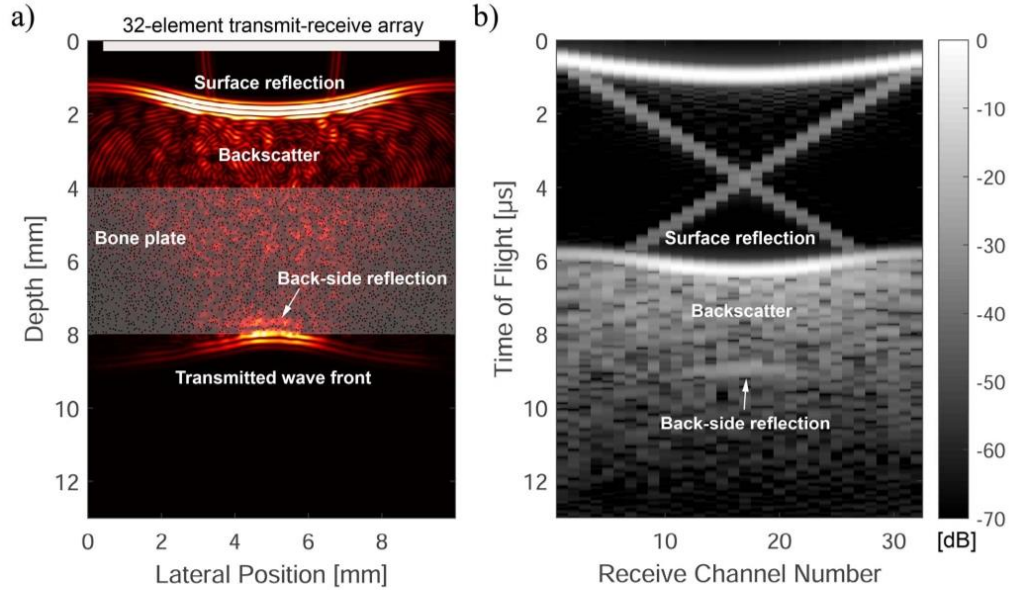
Fig. 1. (a) Snapshot of a numerical simulation model. The bone model contains randomly distributed pores with Po = 9% and Po.Dm = 42.5 μm. (b) Pulse-echo signals (envelope) recorded by the receiver elements. The lateral and temporal increments correspond to the element and pitch sizes of 0.3 mm in the horizontal direction and the temporal sampling increment of 25 ns (after downsampling) in the vertical direction.

measured amplitude and phase spectra of the reflected signals to corresponding simulated spectra. However, the method relies on the assumptions of normal sound incidence on a homogenous material with perfectly flat interfaces and *a priori* knowledge of some material properties, e.g., the attenuation in cortical bone and the reflection coefficient at the bone interfaces. Zheng *et al.* [13] proposed an imaging method of the cortical layer of a bovine tibia bone using a Born-based inversion scattering technique to reconstruct the wave path and to estimate the cortical thickness. The method was demonstrated *ex vivo* on one bovine tibia, but no velocity and thickness values derived from this approach were reported. The combined estimation of cortical thickness and porosity has been achieved by means of full-wave dispersion analysis of guided waves in axial transmission measurements [14]. This method relies on the assumptions as: 1) wave dispersion in long bones can be approximated by a free plate model and 2) that variations of the elastic stiffness tensor at the mm-length scale can be entirely described by the volume fraction of pores pervading the extracellular matrix [15]. However, the application of axial transmission measurements is restricted to patients with low body mass index [16], [17]. Among other reasons, the lack of a direct image-guided measurement results in a high-operator dependence, and underlying assumptions for the parameter estimation may not always be fulfilled. Refraction-corrected bone imaging approach using single-element transmission, and full-array waveform capture has been proposed by Renaud *et al.* [18]. This method provides images of the

periosteal and endosteal bone interfaces and estimates both cortical thickness and an anisotropic sound velocity profile.

The objective of this study was to develop a method that uses conventional, multielement transmit and receive array imaging technology and a refraction-corrected multifocus imaging approach to determine cortical thickness *Ct.Th* and the velocity of the compressional wave propagating in radial bone direction ($Ct.v_{11}$). The method has been validated: 1) *in silico* by means of finite-difference time-domain (FDTD) simulations in academic bone plate models with random microstructures of variable pore sizes and densities and 2) experimentally on nonporous polymer reference material plates and on porous bovine bone plates. Note that for consistency, the variables *Ct.Th* and $Ct.v_{11}$ are used hereinafter for sample thickness and sound velocity, even if the samples were not cortical bone.

II. MATERIALS AND METHODS

A. Numerical Ultrasound Propagation Model

Ultrasound wave propagation in water and bone was simulated using the 2-D FDTD method with Simsonic (www.simsonic.fr) [19]. The elastic simulation model considers multiple scattering, frequency-independent absorption, refraction, diffraction, and wave conversion, which occurs during the wave propagation in a bone. Our model geometry consists of a 4-mm-thick bone plate immersed in water Fig. 1(a)]. Randomly distributed circular pores resemble

50

TABLE I

TISSUE MATERIAL PROPERTIES OF BONE AND PORES USED FOR THE NUMERICAL MODEL. MASS DENSITY ρ AND c_{ij}, I.E., THE COEFFICIENTS OF A TRANSVERSE ISOTROPIC STIFFNESS TENSOR WERE OBTAINED FROM [20] AND THE ABSORPTION VALUE α WAS TAKEN FROM [21]

	BONE	PORES
ρ [g/cm^3]	1.93	1.00
c_{11} [GPa]	23.7	2.25
c_{22} [GPa]	23.7	2.25
c_{12} [GPa]	9.5	2.25
c_{66} [GPa]	6.6	0
v_{11} [m/s]	3504	1500
α [dB/mm]	2.1	0.002

TABLE II

CORTICAL POROSITY ($Ct.Po$) OBTAINED FROM μCT IN BOVINE BONE PLATES. VALUES ARE MEANS ± STANDARD DEVIATION. WIDTH AND LENGTH OF THE SAMPLES ARE REPORTED IN THE LAST TWO COLUMNS

Sample #	$Ct.Po$ (%)	Width (mm)	Length (mm)
1	0.3	23	26
2	0.2	18	28
3	0.9	11	30
4	2.0	12	26

Haversian canals intersecting the image plane. Perfectly matched layers (width: 300 pixels and attenuation: 160 dB) were added at all edges of the map. Material properties for the extracellular bone matrix in human cortical bone are considered to be transverse isotropic [20], with the plane of symmetry parallel to the image plane. The simulation was performed in the isotropic plane with wave propagations in the radial bone direction. Material properties were used from a previous acoustic microscopy study in a human femur [20] and an *ex-vivo* study [21] and are summarized in Table I. A convergence study provided stable results for spatial and temporal grid sizes of 7 µm and 0.93 ns, respectively.

The bone plate was placed 4 mm below the transducer, i.e., a linear array with 32 elements (element and pitch sizes: 0.3 mm). Elements emitted broadband pulses with a center frequency of 5 MHz and a −6-dB bandwidth of 60%. Phase delays were applied to focus the transmit beam subsequently to focus depths of −24 mm with an increment of 1 mm [Fig. 1(a)]. The signals received at all elements were recorded and downsampled to a sampling rate of 80 MHz for further processing [Fig. 1(b)]. Recent *ex-vivo* studies in human cortical bone reported $Ct.Po$ and cortical pore diameter ($Ct.Po.Dm$), defined as the diameter of single Haversian canals or BMU's with a circular shape, values between 2% and 22%, and 7 and 95 µm, respectively [3], [22], [23]. Therefore, two groups were modeled by varying either porosity or pore size: mode I: $Ct.Po.Dm = 38.6$ µm; $Ct.Po \in$ [0%–20%; step size: 2%], cortical pore density $Ct.Po.Dn \in$ [0 mm^{-2}–140 mm^{-2}; step size: 14 mm^{-2}]; and model II: $Ct.Po = 10\%$; $Ct.Po.Dm \in$ [17.7–96.3 µm; variable step size], $Ct.Po.Dn \in$ [408 mm^{-2}–13.7 mm^{-2}; nonlinear decrease with increasing $Ct.Po.Dm$]. Each bone model was generated six times.

B. Sample Collection, Preparation, and Reference Thickness Measurements

A fresh bovine tibia bone was acquired from a local slaughterhouse. A 30-mm disk was extracted from the central shaft region. The disk was further divided into four anatomical quadrants (medial, anterior, lateral, and posterior) using a band saw (EXACT GmbH, Remscheid, Germany).

Ex-vivo studies of the human tibia in the elderly found $Ct.Th$ in the range between ∼1 and 6 mm [3], [24]. Therefore, parallelepiped plates with variable thickness values in the radial direction (i.e., the direction of sound propagation) were prepared by parallel cuts between periosteal and endosteal interfaces. Length (longitudinal bone direction) and width (circumferential direction) of the samples were then further trimmed. The dimensions of all bovine bone plates are summarized in Tables II and III. Moreover, reference material plates of two polycarbonate (PC), one polyvinylchloride (PVC), three polymethylmethacrylate (PMMA), and four short fiber-reinforced epoxy (Sawbone, Malmoe, Sweden) samples with thickness values between 4 and 8 mm were prepared. The Sawbone samples were prepared such that the fiber orientation was perpendicular to the sound propagation direction. The reference thickness $Ct.Th^{\text{Ref}}$ of each sample was measured by means of a micrometer screw (accuracy: ± 0.002 mm) at five different locations.

C. Reference Measurements

1) Plane Wave Pulse-Echo Ultrasound: The 5-MHz plane wave pulse-echo measurements were conducted using a custom-made scanning acoustic microscope (SAM200 Ex, Q-Bam, Halle, Germany) [25]. The samples were immersed in distilled and degassed water at 37 °C. A custom-made unfocused transducer (diameter = 14.5 mm) was used to scan the samples in two dimensions with a scan increment of 112 µm in both the directions. Center frequency and bandwidth of this transducer were 3.6 MHz and 81%, respectively. The distance between the transducer and the sample surface was in the range between 11 and 17 mm. At each scan position, the pulse-echoes from frontside and backside (FB) reflections of the sample [Fig. 2(a)] were captured at 100 MHz using a 12-b A/D card (Gage Compuscope CS12400, Gage Applied Technologies, Lachine, QC, Canada). Bandpass filtering of the radio frequency (RF) signals was done using a Chebyshev Type II filter in the frequency range from 0.1 to 20 MHz. The time-of-flight difference ΔTOF) between FB reflections was determined using cepstral analysis [9], [11]. In contrast to the commonly used smoothing step necessary to remove the spectral characteristics of the transmit pulse from the oscillations caused by repetitive signals in the power spectrum, we have used the gated front-side reflection of each recorded signal as a reference spectrum [26]. First,

| Material		$Ct.Th^{Ref}$ (mm) Mean ± SD	$Ct.Th^{MF}$ (mm) Mean ± SD	CV (%)	$Ct.\nu_{11}{}^{Ref}$ (m/s) Mean ± SD	CV (%)	$Ct.\nu_{11}{}^{MF}$ (m/s) Mean ± SD	CV (%)
Bovine	#1	1.548 ± 0.005	1.60 ± 0.01	0.3	3318 ± 18	0.5	3301 ± 14	0.4
	#2	2.029 ± 0.003	2.03 ± 0.01	0.4	3304 ± 11	0.4	3312 ± 15	0.5
	#3	2.550 ± 0.010	2.54 ± 0.01	0.3	3290 ± 27	0.8	3246 ± 21	0.6
	#4	4.835 ± 0.034	4.81 ± 0.03	0.5	3319 ± 21	0.6	3309 ± 36	1.1
Sawbone®		1.115 ± 0.005	1.13 ± 0.01	1.0	2830 ± 27	1.0	2844 ± 37	1.3
		1.763 ± 0.007	1.80 ± 0.02	1.0	2988 ± 11	0.4	2935 ± 9	0.3
		2.822 ± 0.002	2.83 ± 0.01	0.2	2866 ± 19	0.7	2803 ± 2	0.1
		4.751 ± 0.004	4.78 ± 0.04	0.7	2970 ± 19	0.6	2932 ± 19	0.7
PMMA		0.906 ± 0.003	0.86 ± 0.01	1.0	2745 ± 8	0.3	2715 ± 5	0.2
		1.946 ± 0.001	1.94 ± 0.01	0.3	2707 ± 2	0.1	2699 ± 3	0.1
		3.908 ± 0.001	4.00 ± 0.01	0.3	2714 ± 1	0.1	2701 ± 4	0.1
PVC		8.160 ± 0.003	8.22 ± 0.03	0.4	2299 ± 1	0.1	2325 ± 3	0.1
Polycarbonate		6.237 ± 0.001	6.24 ± 0.03	0.4	2244 ± 1	0.1	2244 ± 8	0.4
		7.181 ± 0.001	7.15 ± 0.03	0.4	2211 ± 3	0.1	2218 ± 5	0.2
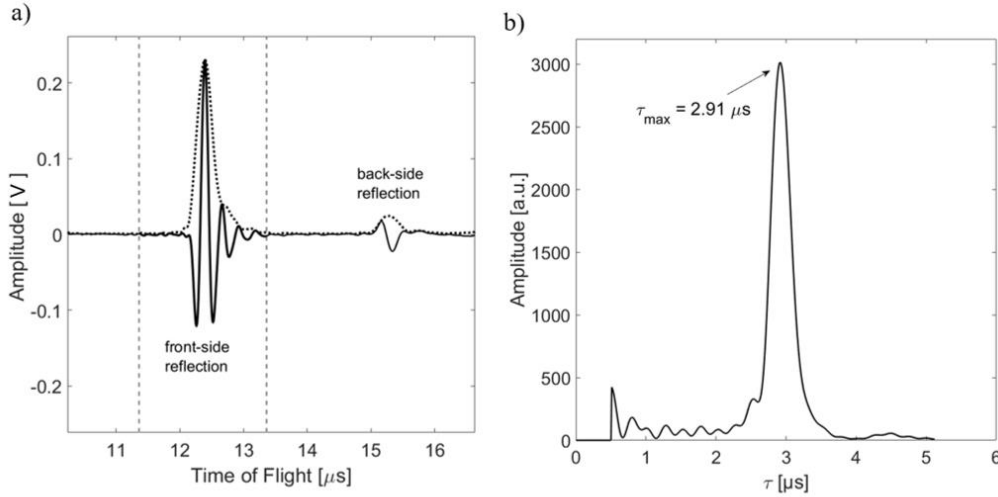
Fig. 2. (a) Pulse-echo signal and Hilbert-transformed envelope signal (black dashed line) from a reference measurement of a 4.84-mm bovine bone plate using an unfocused single-element transducer. A Hanning window (width is indicated by dashed vertical lines) was used to gate the front-side signal. (b) Cepstrum obtained using (1) exhibits a peak at a position that corresponds to the time delay between FB reflections in (a).

the positions of the maxima of FB reflections were determined from the Hilbert-transformed envelope signal using a local peak detection algorithm. Then, Hanning-window gated time segments were created, which extracted either only the front-side reflection (F) or the combined FB signals [Fig. 2(a)]. The power cepstrum $C\tau$) was obtained from the Fast Fourier Transform (FFT) of the normalized power spectrum

$$C(\tau) = \left| \text{FFT}\left(\log_{10} |S_{FB}(f)|^2 - \log_{10} |S_F(f)|^2 \right) \right| \quad (1)$$

whereas $s_i(f)$ is the power spectra of the gated signals F and FB, respectively. Prior to the FFT, the difference spectrum was preconditioned by removing dc and linear components [26]

and the calculation was performed within the −6-dB bandwidth of the transducer. The position of the strongest peak in the power cepstrum [Fig. 2(b)] corresponds to ΔTOF. With the thickness values obtained using the micrometer screw, the compressional sound velocity $Ct.\nu_{11}^{Ref}$ was obtained

$$Ct.\nu_{11}^{Ref} = \frac{2 \cdot Ct.Th^{Ref}}{\Delta \text{ToF}}. \quad (2)$$

Mean, standard deviation, and coefficient of variation were assessed in homogenous image regions for each sample.

2) Microcomputed Tomography (μCT): High-resolution reference values of $Ct.Th^{Ref}$ and $Ct.Po^{Ref}$ of the bovine samples
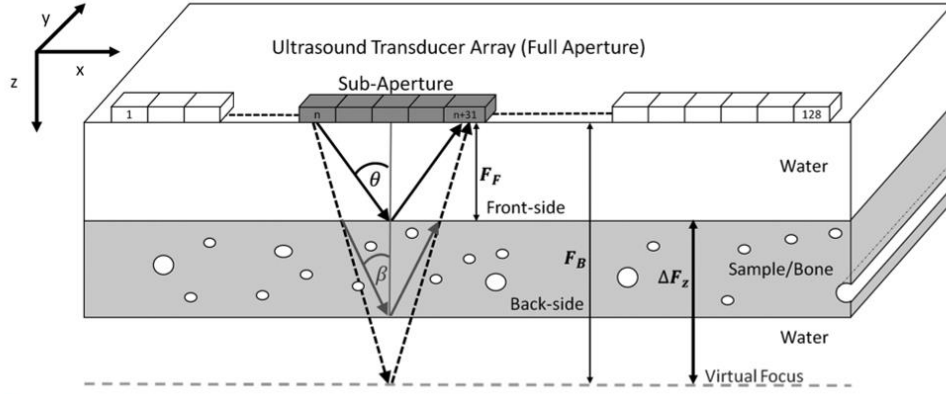
Fig. 3. Schematic illustration of the multifocus measurement in the radial direction (x, z) of a long bone. The transducer is positioned 20 mm above the sample. Focused sound beams are emitted using a 32-element subaperture of a 128-element linear array. The semi-aperture angle θ of the transmit beam is gradually decreased to move the focus from a depth above the sample front side to a position below backside of the sample. Refraction at the front-side interface results in a change the propagation direction of transmitted waves, and thereby, a shift of the focus depth inside the sample. ΔF_z indicates the shift of the focus depth needed to focus from the frontside (F_F) to the backside (F_B). In addition to the scan of the focus depth, subaperture is scanned along the array (x) direction.

were determined using a SkyScan 1172 scanner (Bruker MicroCT, Kontich, Belgium). The scan parameters were— 80 kV; 124 μA; 0.5-mm aluminum filter; exposure time 9.4 s; image averaging over three frames; rotation: 180°; rotation step size: 0.1°; and field of view: 8 × 8 mm^2. The image reconstruction was performed using the NRecon reconstruction software (v.1.10.1, Skyscan NV, Kontich, Belgium) with the following settings—beam hardening correction: 25%; ring artifact reduction: 45; and manual postalignments depending on the samples. The isotropic voxel size of the reconstructed volume data was 11.94 μm. For each examination, a stack of 1.246 cross-sectional images was stored in 8-b file format. A 3-D Gaussian smoothing kernel with standard deviation of 1.2 and a 2-D median filter with a size of 50 × 50 was applied to remove noise from the images. Pores and bone matrix were segmented using Otsu's method [27]. A rectangular volume of interest (VOI) with margins 0.2 mm inside the sample limits was manually defined. Within each VOI, the porosity $Ct.Po^{\text{Ref}}$ was determined by the ratio between pore voxels and total number of voxels within the VOI. The error of the porosity estimation with this setup is in the order of < 0.2% [28].

D. Multifocus Ultrasound Acquisition

Multifocus imaging was performed with a medical ultrasound scanner SonixTOUCH equipped with a 3-D linear array transducer 4DL14-5/38 (consisting of a 1-D 128-element array, center frequency 8 MHz, pitch 0.3 mm, and a sweep motor that allows automatic acquisition of 3-D volumes), and a SonixDAQ single-channel data acquisition system (Ultrasonix, Richmond, BC, Canada). The SonixDAQ is a research add-on that allows simultaneous pre-beamformed single-channel RF data acquisition of all 128 channels. The samples were immersed and degassed in water for 30 min.

Fig. 3 shows the multifocus setup. The transducer array was positioned perpendicular to the bone long axis and parallel to the bone surface. The measurement sequence consisted of a series of conventional B-mode imaging sequences with $N_{\text{Tx}} = 128$ lateral scan positions x_i. At each x_i scan position, sound waves were focused on the radial bone direction into the plates using a 32-element transmit aperture. Subsequent B-mode images were acquired with gradually increasing focus depths F_z (16 steps; starting from 10 mm with a step size of 2 mm). The semi-aperture angle θ was defined by aperture size and focus depth F_z. In order to optimize penetration depth, the transducer elements were not excited at their resonance frequency, but with a single "+" signal at a system transmit frequency of 5 MHz, which produced signals with a center frequency of 5.1 MHz and a bandwidth of 69% [Fig. 4(d)]. Single-channel RF data ($N_{\text{Rx}} = 128$) were captured at a sampling rate of 40 MHz with 12-b resolution, resulting in a 4-D Matrix $V(N_{\text{Tx}}, F_z, N_{\text{Rx}}, t)$ with dimensions 128 × 16 × 128 × 1023. The temperature of the water was measured during the acquisition throughout to calculate sound velocities in water v_{H20} depending on temperature following [29]. All measurements were repeated five times with sample repositioning between measurements.

E. Image and Signal Processing

Beamformed images were reconstructed using the same aperture and focus depth as for the transmit beams, resulting in a 3-D matrix $V_{\text{Rx-focus}}(F_z, x, t)$. For visualization of the confocal reflection amplitudes, a maximum projection image $V_{\text{MPI}}(x, t)$ was created [Fig. 4(a)]. The time of flights [$\text{TOF}_F(x, z)$ and $\text{TOF}_B(x, z)$] and amplitudes [$V_F(x, F_z)$ and $V_B(x, F_z)$] of reflections from the sample's FB, respectively, were tracked for each array scan position and focus depth
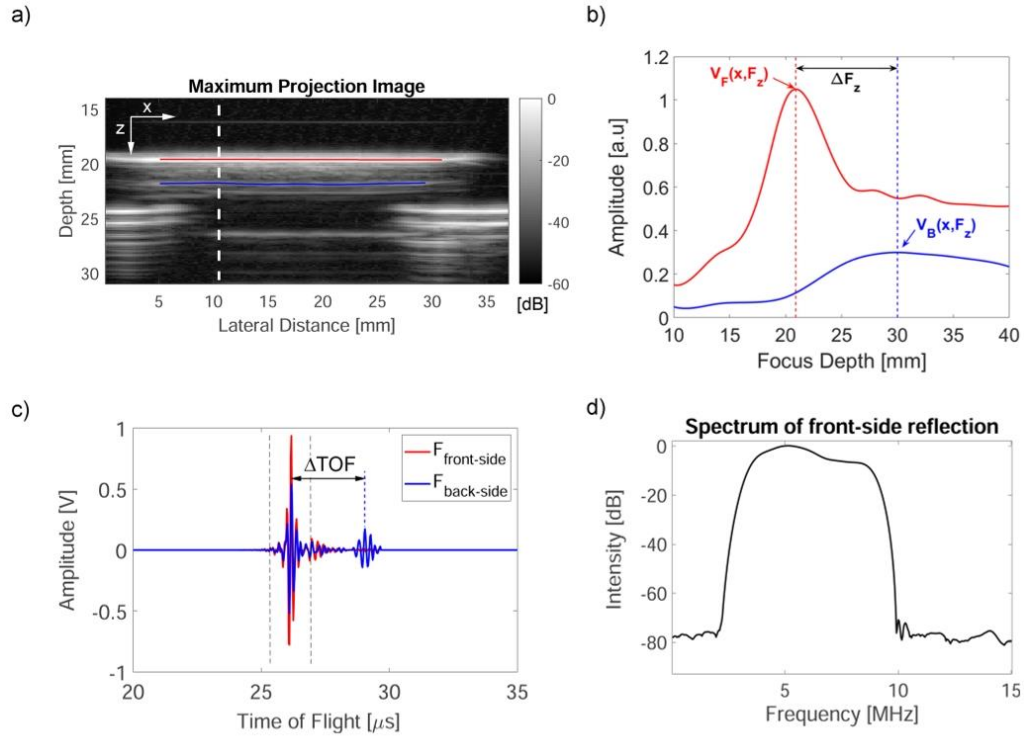
a)

b)

c)

d)

Fig. 4. (a) Maximum projection B-mode image reconstructed from all focus depths with tracked front (red line) and backside surfaces (blue line) of a bovine sample. (b) Tracked amplitudes at the lateral scan position indicated by a white dashed line in (a) of front (red line) and backside surface reflections (blue line) of a 4.79-mm bovine sample versus focus depth. The confocal FB focus positions can be determined from the maxima of $V_F(x, F_z)$ and $V_B(x, F_z)$. (c) Corresponding beamformed pulse-echo signals with confocal beamforming at 21 mm ($F_{frontside}$) and 30 mm ($F_{backside}$). The vertical dashed lines indicate the time gate for the calculation of the power spectrum. (d) Mean power spectrum of all gated front-side echoes.

[Fig. 4(b)] and the ΔTOF between confocal frontside and backside reflections was determined.

For each lateral scan position x_i, the $\Delta\text{TOF}(x_i)$ between confocal FB reflections and the focus shift ΔF_z between confocal FB positions were determined [Fig. 4(c)]. The shift ΔF_z needed to focus from the front to the backside is determined by the sample thickness $Ct.Th$, the semi-aperture angle θ of transmit and receive beams, and the sound velocities in water v_{H2O} and bone $Ct.v_{11}$ [30], [31]

$$Ct.Th = \frac{\Delta F_z}{0.5 \frac{Ct.v_{11}}{v_{H_2O}} \cdot \left(1 - \frac{Ct.v_{11}^2}{v_{H_2O}^2}\right) \cdot (1 - \cos(k_{\text{eff}}\theta)) - \frac{Ct.v_{11}}{v_{H_2O}}}.$$
(3)

The factor k_{eff} in (3) accounts for: 1) the increasing conversion of compressional waves into shear waves with increasing angle of incidence and 2) the complete lack of compressional wave transmission into the solid for inclination angles larger than a critical angle θ_{crit}

$$\theta_{\text{crit}} = \arcsin\left(\frac{v_{H_2O}}{Ct.v_{11}}\right).$$
(4)

$k_{\text{eff}}\theta$ can be interpreted as an effective aperture contributing to the beam focusing on the backside. The factor k_{eff} depends on the semi-aperture θ and the transmittance and reflectance functions. In this study, an algorithm was developed to estimate k_{eff} based on θ and θ_{crit} and k_{eff} was derived for each measurement iteratively.

The scanning of the beams along the array (x_i) direction enables local estimations of sound velocity and thickness. The lateral resolution of the estimates is determined by the lateral beamwidth interrogating the sample while focusing on the backside of the sample. Therefore, $Ct.v_{11}(x_i)$ and $Ct.Th(x_i)$ estimations were smoothed using a robust moving average filter with a span of 21 prior to the calculations of sample means and standard deviations.

F. Statistics

The normality of the parameter distributions was confirmed using the Lilliefors test. Pearson linear regression analysis and Bland–Altman plots [32] were conducted to compare the parameters obtained using the multifocus method with reference values. Precision was defined as the coefficient of
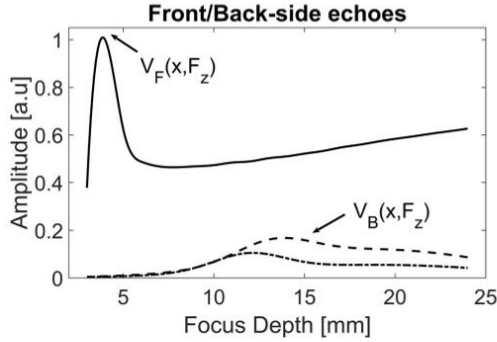
54

Fig. 5. Representative result of the tracking of front (black line) and backside reflections (–: $Po = 0\%$; - ·: $Po = 13\%$) using the multifocus approach.

variation (CV) of the difference between predicted and reference relative to the mean of the reference values. Accuracy was determined by means of the root-mean-squared error compared with the reference values. Reproducibility was assessed as the intrasample CV of repeated measurements. If parameters were normally distributed, paired t-tests were used to evaluate if the parameters estimated using the multifocus method were significantly different compared with the reference methods. Otherwise a Wilcoxon rank-sum test was used. The significance level was defined as $p < 0.05$. All analyses were performed using the MATLAB including the Signal Processing, Curve Fitting, and Statistics Toolboxes (The Mathworks, Natick, MA, USA).

III. Results

A. Numerical Simulations

The FB echo amplitudes and their corresponding TOF could be retrieved from all simulation models. A representative result of the tracking of FB reflections is shown in Fig. 5.

For all simulations, the peak of the surface echo occurred at a focus depth of 4 mm. In contrast, the peak position and amplitude of the backside reflection varied depending on the pore properties. For a homogenous bone plate with 0% porosity, the confocal backside position was at a focus depth of 14 mm. All models which contained pores exhibited decreased confocal backside amplitudes and focus depth positions.

The simulation results of model I revealed a dependence of the estimated sound velocity ($Ct.v_{11}^{MF}$) on the reference velocity ($Ct.v_{11}^{Ref}$) if the semi-aperture θ was close to the critical angle. The following algorithm was applied to all subsequent analyses:

$$k_{\text{eff}} = \begin{pmatrix} 1 \text{ if } \theta < \theta_{\text{crit}} - 10° \\ 0.1 \cdot \Delta\theta \text{ if } \theta > \theta_{\text{crit}} - 10° \end{pmatrix} \quad (5)$$

whereas $\Delta\theta = \theta_{\text{crit}} - \theta$. The factor k_{eff} was determined in five iterations, starting with $k_{\text{eff}} = 1$.

All parameters obtained from model I ($Ct.Po.Dm = 40 \ \mu m$) were normally distributed. $Ct.v_{11}$ decreased with

increasing sample porosity [Fig. 6(a)]. The accuracy and precision of the multifocus method were 36.9 m/s and 1.1%, respectively [Fig. 6(b)]. The $Ct.v_{11}^{MF}$ values were not significantly different from the reference values $Ct.v_{11}^{Ref}$. Accuracy and precision of the estimation of $Ct.Th^{MF}$ were 0.04 mm and 1.0%, respectively [Fig. 6(c)]. The estimations were not significantly different from the model thickness.

Except for the reference velocity values, all parameters obtained from model II ($Ct.Po = 10\%$) were normally distributed. $Ct.v_{11}$ decreased with a decreasing pore size (or increasing pore density) [Fig. 7(a)]. The $Ct.v_{11}^{MF}$ values were not significantly different from the values obtained from reference method [Fig. 7(b)]. The accuracy and precision of the multifocus method were 52 m/s and 1.8%, respectively. Cortical thickness estimations $Ct.Th^{MF}$ were not significantly different from the model thickness. Accuracy and precision were 0.26 mm and 6.3%, respectively [Fig. 7(c)]. It should be noted that both accuracy and precision decreased for very large-pore diameters.

B. Multifocus Measurements

The multifocus method failed on the first and last array scan positions, for which only a part of the 32-channel aperture could be used for beamforming. However, FB echo amplitudes and their corresponding TOF could be retrieved from all samples for at least 40 out of the 128 beamformed scan positions. Cortical thickness and porosity values of the bovine samples are summarized in Table II. Table III contains parameters obtained from reference and multifocus methods for each sample. The reproducibility of $Ct.v_{11}^{MF}$ and $Ct.Th^{MF}$ were 0.52% and 0.44%, respectively.

For the nonporous polymer samples, no variations of $Ct.Th^{MF}$ and $Ct.v_{11}^{MF}$ with respect to the array position were observed [Fig. 8(a)]. A higher variability along the scan position was observed in the bovine samples, particularly in that with the highest porosity of 2% (Table II). It should be noted that pronounced local variations occurred for $Ct.v_{11}^{MF}$ but not for $Ct.Th^{MF}$ [Fig. 8(b)].

All derived mean parameters were normally distributed. The $Ct.v_{11}$ and $Ct.Th$ values obtained from the multifocus method were not significantly different from the values obtained using the reference methods (Fig. 8). Accuracy and precision were 24.1 m/s and 0.89%, respectively, for $Ct.v_{11}^{MF}$ and 0.04 mm and 1.13%, respectively, for $Ct.Th^{MF}$ (Fig. 9).

IV. Discussion

This study describes a simple method that allows the simultaneous estimation of thickness and compressional sound velocity in plate-shaped cortical bone samples using a phased-array ultrasound. The method uses refraction occurring at the interface between the soft and hard materials and refraction-corrected focusing to provide a multifocus image of both interfaces of the plate. We applied confocal transmit and receive beamforming, peak detection, and signal tracking algorithms, and an iterative approximation of an effective aperture to retrieve $Ct.v_{11}^{MF}$ and $Ct.Th^{MF}$. A parametric numerical
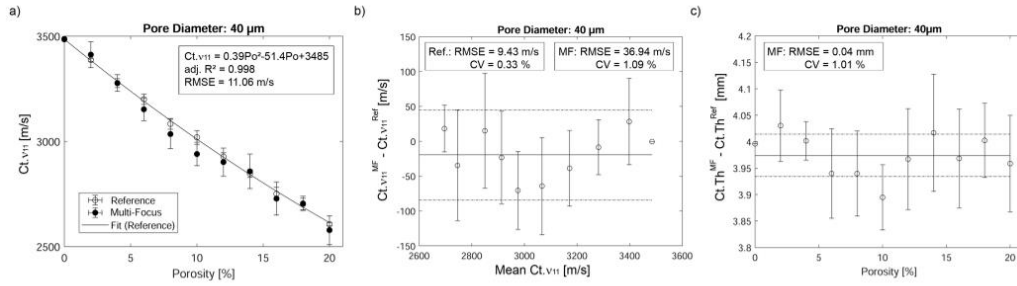
Fig. 6. Estimation of SOS and thickness in model I (pore size: 40 μm, variable pore density). (a) Sound velocity decreased with increasing porosity (white dots: reference method and black dots: multifocus method). (b) Bland–Altman plot of $Ct.\nu_{11}^{MF}$ versus $Ct.\nu_{11}^{Ref}$. (c) Difference between $Ct.Th^{MF}$ and model thickness ($Ct.Th^{Ref} = 4$ mm) as a function of porosity. The mean differences [horizontal straight lines in (b) and (c)] were not significantly different from the reference values.
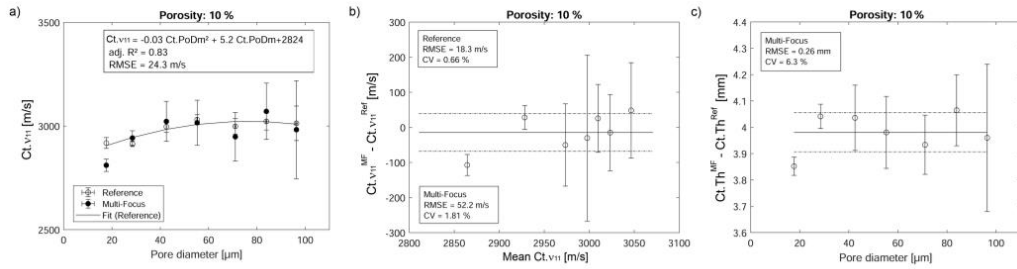

Fig. 7. Estimation of SOS and thickness in model II (porosity: 10%, variable pore size). (a) Sound velocity decreased for small pore sizes ($Ct.Po.Dm < 40$ μm) was smaller than the values for larger pores (white dots: reference method and black dots: multifocus method). (b) Bland–Altman plot of $Ct.\nu_{11}^{MF}$ versus $Ct.\nu_{11}^{Ref}$. (c) Difference between $Ct.Th^{MF}$ and model thickness ($Ct.Th^{Ref} = 4$ mm) as a function of porosity. The mean differences [horizontal straight lines in (b) and (c)] were not significantly different from the reference values.
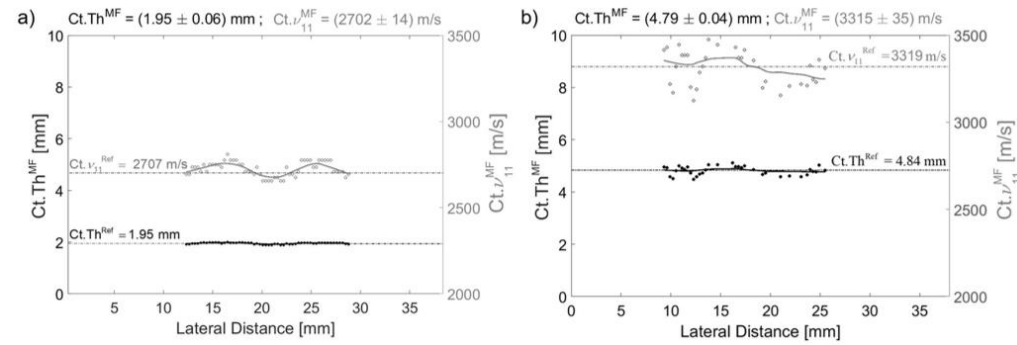

Fig. 8. Representative plots of $Ct.Th^{MF}(x_i)$ and $Ct.\nu_{11}^{MF}(x_i)$ obtained from (a) PMMA plate and (b) bovine bone plate. The dots indicate the estimations for each individual array position, and the straight lines are the estimations using a moving average filter. Means and standard deviations were determined from the smoothed data. The number of individual scan positions contributing to the parameter estimations in (a) and (b) were 56 and 40, respectively.

simulation study was conducted to test the method on idealized porous structures with randomly distributed pores of variable size and density. Reproducibility, accuracy, and precision of the method were assessed experimentally on homogenous and heterogeneous polymer phantoms and on bovine cortical bone plates.

A. Numerical Simulations

The ability to apply the method for a typical cortical bone pore size and variable pore densities resulting in porosities up to 20% was shown in model I. The observed decrease of $Ct.\nu_{11}$ with increasing porosity is consistent with the
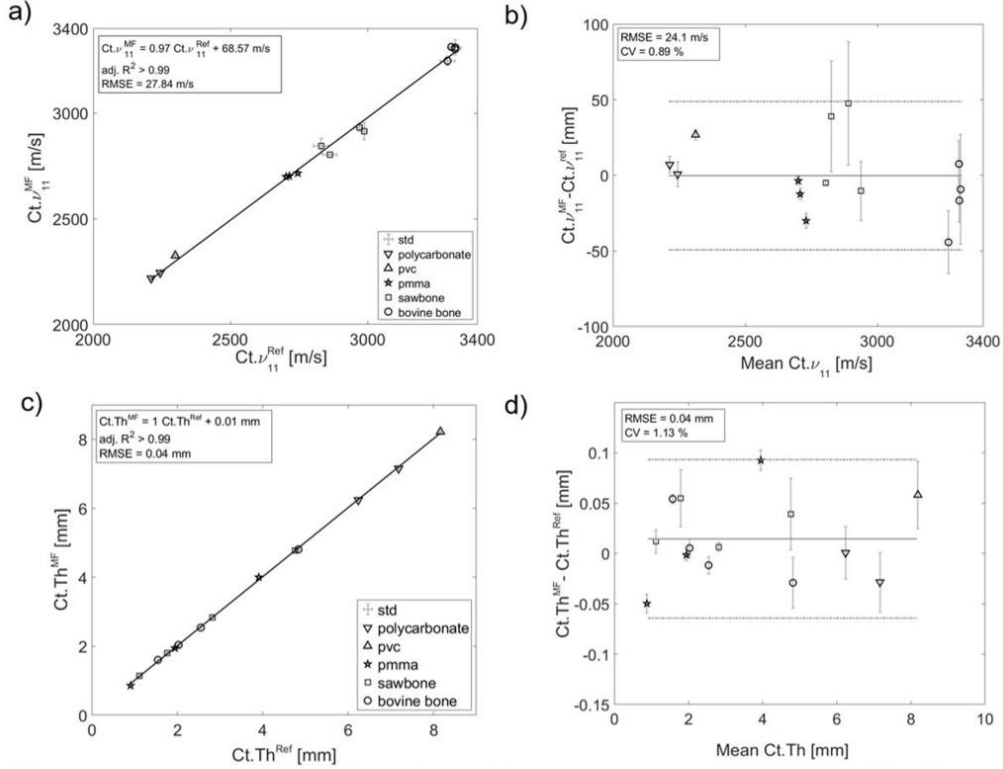
56

Fig. 9.   Experimentally derived $Ct.\nu_{11}$ (a) and (b), and $Ct.Th$ (c) and (d). The mean differences [horizontal straight lines in (c) and (d)] were not significantly different from the reference values.

well-established assumption that elastic properties of cortical bone can be approximated by a two-phase model consisting of a solid extracellular matrix pervaded by fluid-filled pores with a certain pore volume fraction [33]. To compare their values with our data, we calculate the compound mass density using the upper bound rule of mixtures for composites, i.e., $Ct.\rho_{Compound} = Ct.Po \cdot \rho_{H_2O} + (1 - Ct.Po) \cdot \rho_{Tissue}$, whereas ρ_{Tissue} is the density of the bone tissue matrix (Table I). The elastic stiffness coefficients at 0% and 20 % porosity are obtained from $Ct.c_{11}(Ct.Po) = \rho_{Compound}(Ct.Po) \cdot (Ct.\nu_{11}(Ct.Po))^2$. The relative decrease of the elastic coefficient $Ct.c_{11}$ of approximately 38.4% for an increase in $Ct.Po$ from 0% to 20 % reported in [33] was considerably smaller than the decrease of $Ct.c_{11}$ of 59% obtained in our study. The larger decrease with increasing porosity observed in our model suggests that pore density has an impact on $Ct.\nu_{11}$ in addition to porosity. This was also apparent in model II, in which porosity was kept constant. For increasing pore densities realized by a decrease of the pore size, a gradual decrease of $Ct.\nu_{11}$ was observed [Fig. 7(a)]. The resulting variations of $Ct.\nu_{11}$ and $Ct.c_{11}$ in the evaluated pore size range were 2.8% and 5.5%, respectively. A possible explanation is that

an increase of pore density increases the number of multiple scatter events, and thereby, also increases the effective propagation path length, which is in agreement with recent studies of Yousefian et al. [34] and Karbalaeisadegh et al. [35], who investigated the effects of pore size and density on ultrasound attenuation in similar models. It should also be noted that models with very large-pore sizes and low pore densities resulted in high variability of the parameter estimates, both for the reference and the multifocus methods. This is reasonable, as, in these models, the assumption of a random pore distribution was not fulfilled anymore. In summary, the strong dependence of sound velocity in the radial direction on porosity confirms: 1) the necessity to assess this parameter in order to quantify cortical thickness; 2) that a change in $Ct.\nu_{11}$ is a good surrogate parameter for changes in cortical porosity. However, the effects of variable matrix stiffness caused by age [36] or pathologies [37] and the pore architecture on the association between $Ct.\nu_{11}$ and $Ct.Po$ need to be considered.

B. Multifocus Measurements

The experiments using a 128-element linear phased array probe was performed on nonporous, homogeneous plates

(PMMA, PC, and PVC), on a heterogenous Sawbone composite polymer, and on bovine plates with low porosity. The elements were excited with a frequency of 5 MHz to ensure a good combination of penetration depth and temporal resolution. The evaluated samples provided a range of sound velocities and thickness values typically found in human cortical bone. The sound velocity values measured in Sawbone ($Ct.v_{11}^{\mathrm{MF}} = 2883 \pm 57$ m/s) were consistent with our reference measurements and with values reported by others [12], [14]. In the porous bone samples, the variability of $Ct.v_{11}^{\mathrm{MF}}$ along the probe was higher compared with that in the polymer plates (Fig. 9). As the plate thickness was invariant within a sample, it demonstrates the ability of the method to resolve and visualize local variations of $Ct.v_{11}$.

Accuracy and precision observed in the experiments were considerably better than those observed in the simulations. This is not surprising, since *in-silico* estimations of $Ct.Th$ and $Ct.v_{11}$ consisted of six individual model realizations, while the experiments consisted of at least 40 estimations per measurement and five repetitions.

Wydra *et al.* [38] have used a similar refraction measurement approach and reported for measurements on porous plate-shaped skull bone phantoms precision values of 8.5% and 4.1% for thickness and SOS, respectively. Their precision values in pore-free phantoms were approximately 50% lower. In contrast, our experimental precision values were much better (< 1.5% for SOS and thickness), which can be attributed to both the higher frequency (5 versus 2.25 MHz) and the consideration of an effective aperture in our study. An *ex-vivo* accuracy of 0.2 mm of the thickness estimation in human radius bones using 0.5-MHz guided waves in axial transmission at human has been reported by Schneider *et al.* [24]. Although the accuracy of 0.03 mm of the multifocus was considerably better, the different samples' geometries (plates versus real irregular periosteal and endosteal bone boundaries) prohibit a direct comparison. Future studies should, therefore, assess the performance of the multifocus method on real human cortical bones.

However, a fundamental advantage of the proposed method in comparison with the guided-wave method is that it provides direct image guidance. The bone surface is clearly visible in the ultrasound image allowing optimal probe positioning prior to the data acquisition. Although it was not implemented in the current study, multifocus beamforming, reconstruction of the maximum projection image, and interface tracking could, in principle, be performed in real time. Thereby, the operator would have immediate visual feedback about the measurement success and high failure rates, e.g., up to 20% for axial transmission measurements [16], [39] could be avoided. This was not possible with the used system, as the time for the transfer of data from the data acquisition box to the hard drive (27 s), data conversion (42 s), and beamforming on standard CPU (61 s) was too long, but could be achieved with GPU-based ultrafast imaging platforms.

Another approach to measure the cortical bone thickness and SOS using refraction-corrected imaging with a 2.5-MHz linear phased array transducer has been proposed by Renaud *et al.* [18]. In contrast to the multifocus method,

they use single-element excitation, full-array waveform capture, and an ultrasound image reconstruction adapted from seismology, which also provides information about elastic anisotropy. The concept of finding the optimal focus quality by incorporating variable sound velocities along the propagation paths for the delay-and-sum image reconstruction is similar to our approach. Key differences of the multifocus approach are that: 1) transmission losses caused by refraction and mode conversion at the periosteal bone interface are considered to obtain correct thickness and velocity values and 2) 32-element focused beams are used instead beams emitted from single elements. The latter may result in a smaller signal-to-noise ratio compared with multi-element transmit and receive focusing, which should be elaborated in future studies.

C. Limitations

Our study has several limitations. Both the numerical and experimental studies were restricted to simple plate-shaped geometries. The cortical microstructure bone was simulated using randomly distributed circular pores of uniform size. The parameter estimation relies on the estimations of $\Delta\mathrm{TOF}$ and ΔF_z. In particular, the confocal peak arising from the backside reflection was less sharp compared with that from the front side. The sharpness of the backside peak depends on many factors, e.g., frequency, bandwidth, signal-to-noise ratio, aperture angle, critical angle, plate thickness, porosity, flatness, and roughness of FB interfaces. Curved and irregular bone interfaces [38] and heterogenous pore sizes with pore size gradients, typically found in human cortical bones, particularly in osteoporotic bones, will lead to additional phase distortions of the propagating wave. While a comprehensive analysis of individual effects on the accuracy of the estimations $\Delta\mathrm{TOF}$ and ΔF_z was beyond the scope of this study and the incorporation of appropriate phase aberration correction algorithms was not necessary for the current study, these aspects should be considered in the future based on more the realistic simulation models. Moreover, future experimental studies should target human bone instead of the bovine plexiform bone used in this study to demonstrate the applicability of the method also for the clinically relevant tissue types with higher porosities. Another limitation of our simulation model was the frequency-independent absorption. Although the major contribution of frequency-dependent attenuation can be considered to arise from the scattering on pores rather than from absorption [34], other simulation codes may be better suited to investigate their relative impacts.

D. Transition to In Vivo Measurements

This study demonstrates the assessment of $Ct.Th$ and $Ct.v_{11}$ *ex vivo* using a clinical ultrasound scanner. To approve the *in vivo* feasibility of the multifocus imaging technique, the implementation of the aforementioned phase-aberration corrections, more sophisticated algorithms for the detection of the bone surface, eventually in combination with edge-enhancing image filters are required. Moreover, the method can only be applied with the imaging plane

parallel to the plane of transverse isotropy, i.e., the radial direction perpendicular to the long bone axes [40]. Potential measurement regions are shaft regions, in which the cortical thickness is not much smaller than 1 mm, and the geometry is approximately plate-shaped, e.g., the medial portion of the tibia. However, the application to other large long bones, such as radius or femur, or to smaller bones, such as phalanges or jawbones, is also feasible. For the latter, probes with higher frequencies and smaller form factors should be used.

E. Clinical Use of Ultrasound Parameters

The developed technique is anticipated to have high clinical potential since it uses conventional medical ultrasound technology, is noninvasive and nonionizing and can assess locally $Ct.Th$ and $Ct.v_{11}$ with image guidance at multiple skeletal sites. Previous studies have already demonstrated the high relevance of cortical SOS [41]–[43] and thickness [24], [39] measured by axial transmission as biomarkers for bone quality. Cortical bone of the tibia has been proposed as a favorable measurement site for the prediction of bone fracture risk since it is load bearing, can be easily measured by ultrasound, and changes in thickness and pore morphology, i.e., the prevalence of large pores are associated with a mechanical impairment of the hip [3]. Moreover, a recent *in vivo* study by Minonzio et al. [16] has demonstrated that $Ct.Th$ and $Ct.Po$ derived from full-wave dispersion axial transmission at the distal radius in postmenopausal women are suitable biomarkers for the discrimination of nontraumatic fracture from nonfractured cases and that distinct associations of the two biomarkers with fracture location exist, even in cases in which fractures were not associated with any DXA-based parameter. Compared with axial transmission methods, no dedicated hardware is required for the multifocus measurement, and the parameter estimations are locally resolved within the imaging plane and provide image guidance. Therefore, it has a high potential as an add-on or even alternative to X-ray imaging, particularly for longitudinal and pediatric applications. The implementation of $Ct.Th$ and $Ct.v_{11}$ as complementary diagnostic biomarkers may improve fracture risk prediction.

V. CONCLUSION

This work shows that cortical thickness and the compressional sound velocity in the radial direction can be determined precisely using refraction-corrected multifocus imaging. The method was developed and tested *in-silico* and experimentally on plate-shaped polymer samples, cortical bone phantoms, and on bovine tibia bone samples. For reliable parameter estimation, refraction and wave conversion losses at the bone surface must be considered. The derived parameters showed excellent agreement with reference values.

VI. CONFLICTS OF INTEREST

Dr. J. Du and Dr. K. Raum have the patent "CortBS: Ultrasonic method for determining pore dimensions in cortical bone" pending.

REFERENCES

[1] E. Hernlund *et al.*, "Osteoporosis in the European Union: Medical management, epidemiology and economic burden: A report prepared in collaboration with the international osteoporosis foundation (IOF) and the European federation of pharmaceutical industry associations (EFPIA)," *Arch. Osteoporosis*, vol. 8, p. 136, Dec. 2013.

[2] R. Zebaze and E. Seeman, "Cortical bone: A challenging geography," *J. Bone Mineral Res.*, vol. 30, no. 1, pp. 24–29, 2015.

[3] G. Iori *et al.*, "Large cortical bone pores in the tibia are associated with proximal femur strength," *PLoS ONE*, vol. 14, no. 7, 2019, Art. no. e0215405.

[4] K. K. Nishiyama, H. M. Macdonald, H. R. Buie, D. A. Hanley, and S. K. Boyd, "Postmenopausal women with osteopenia have higher cortical porosity and thinner cortices at the distal radius and tibia than women with normal aBMD: An *in vivo* HR-pQCT study," *J. Bone Mineral Res.*, vol. 25, no. 4, pp. 882–890, 2010.

[5] E. S. Siris *et al.*, "Bone mineral density thresholds for pharmacological intervention to prevent fractures," *Arch. Internal Med.*, vol. 164, no. 10, pp. 1108–1112, 2004.

[6] S. C. E. Schuit *et al.*, "Fracture incidence and association with bone mineral density in elderly men and women: The Rotterdam study," *Bone*, vol. 34, no. 1, pp. 195–202, 2004.

[7] S. A. Wainwright *et al.*, "Hip fracture in women without osteoporosis," *J. Clin. Endocrinol. Metabolism*, vol. 90, no. 5, pp. 2787–2793, 2005.

[8] P. H. F. Nicholson, "Ultrasound and the biomechanical competence of bone," *IEEE Trans. Ultrason., Ferroelectr., Freq. Control*, vol. 55, no. 7, pp. 1539–1545, Jul. 2008.

[9] J. Karjalainen, O. Riekkinen, J. Toyras, H. Kroger, and J. Jurvelin, "Ultrasonic assessment of cortical bone thickness *in vitro* and *in vivo*," *IEEE Trans. Ultrason., Ferroelectr., Freq. Control*, vol. 55, no. 10, pp. 2191–2197, Oct. 2008.

[10] J. P. Karjalainen *et al.*, "Multi-site bone ultrasound measurements in elderly women with and without previous hip fractures," *Osteoporosis Int.*, vol. 23, no. 4, pp. 1287–1295, 2012.

[11] K. A. Wear, "Autocorrelation and cepstral methods for measurement of tibial cortical thickness," *IEEE Trans. Ultrason., Ferroelectr., Freq. Control*, vol. 50, no. 6, pp. 655–660, Jun. 2003.

[12] Y. Tasinkevych, J. Podhajecki, K. Falińska, and J. Litniewski, "Simultaneous estimation of cortical bone thickness and acoustic wave velocity using a multivariable optimization approach: Bone phantom and *in-vitro* study," *Ultrasonics*, vol. 65, pp. 105–112, Feb. 2016.

[13] R. Zheng, L. H. Le, M. D. Sacchi, and E. Lou, "Imaging internal structure of long bones using wave scattering theory," *Ultrasound Med. Biol.*, vol. 41, no. 11, pp. 2955–2965, 2015.

[14] J. Foiret, J.-G. Minonzio, C. Chappard, M. Talmant, and P. Laugier, "Combined estimation of thickness and velocities using ultrasound guided waves: A pioneering study on *in vitro* cortical bone samples," *IEEE Trans. Ultrason., Ferroelectr., Freq. Control*, vol. 61, no. 9, pp. 1478–1488, Sep. 2014.

[15] M. Granke, Q. Grimal, A. Saïed, P. Nauleau, F. Peyrin, and P. Laugier, "Change in porosity is the major determinant of the variation of cortical bone elasticity at the millimeter scale in aged women," *Bone*, vol. 49, no. 5, pp. 1020–1026, 2011.

[16] J.-G. Minonzio *et al.*, "Ultrasound-based estimates of cortical bone thickness and porosity are associated with nontraumatic fractures in postmenopausal women: A pilot study," *J. Bone Mineral Res.*, vol. 34, no. 9, pp. 1585–1596, 2019.

[17] P. Moilanen *et al.*, "Modeling the impact of soft tissue on axial transmission measurements of ultrasonic guided waves in human radius," *J. Acoust. Soc. Amer.*, vol. 124, no. 4, pp. 2364–2373, 2008.

[18] G. Renaud, P. Kruizinga, D. Cassereau, and P. Laugier, "*In vivo* ultrasound imaging of the bone cortex," *Phys. Med. Biol.*, vol. 63, no. 12, 2018, Art. no. 125010.

[19] E. Bossy, M. Talmant, and P. Laugier, "Three-dimensional simulations of ultrasonic axial transmission velocity measurement on cortical bone models," *J. Acoust. Soc. Amer.*, vol. 115, no. 5, pp. 2314–2324, 2004.

[20] D. Rohrbach *et al.*, "Spatial distribution of tissue level properties in a human femoral cortical bone," *J. Biomech.*, vol. 45, no. 13, pp. 2264–2270, 2012.

[21] M. Sasso, G. Haïat, Y. Yamato, S. Naili, and M. Matsukawa, "Frequency dependence of ultrasonic attenuation in bovine cortical bone: An *in vitro* study," *Ultrasound Med. Biol.*, vol. 33, no. 12, pp. 1933–1942, 2007.

[22] C. Chappard *et al.*, "3D characterization of pores in the cortical bone of human femur in the elderly at different locations as determined by synchrotron micro-computed tomography images," *Osteoporosis Int.*, vol. 24, no. 3, pp. 1023–1033, 2013.

[23] L. P. Bakalova *et al.*, "Intracortical bone mechanics are related to pore morphology and remodeling in human bone," (in English), *J. Bone Mineral Res.*, vol. 33, no. 12, pp. 2177–2185, 2018.

[24] J. Schneider *et al.*, "*Ex vivo* cortical porosity and thickness predictions at the tibia using full-spectrum ultrasonic guided-wave analysis," *Arch. Osteoporosis*, vol. 14, no. 1, p. 21, 2019.

[25] S. Lakshmanan, A. Bodi, and K. Raum, "Assessment of anisotropic tissue elasticity of cortical bone from high-resolution, angular acoustic measurements," *IEEE Trans. Ultrason., Ferroelectr., Freq. Control*, vol. 54, no. 8, pp. 1560–1570, Aug. 2007.

[26] S. Lakshmanan *et al.*, "Prediction of the intramuscular fat content in loin muscle of pig carcasses by quantitative time-resolved ultrasound," *Meat Sci.*, vol. 90, no. 1, pp. 216–225, 2012.

[27] N. Otsu, "A threshold selection method from gray-level histograms," *IEEE Trans. Syst., Man, Cybern.*, vol. 9, no. 1, pp. 62–66, Jan. 1979.

[28] H. M. Britz, J. Jokihaara, O. V. Leppänen, T. Järvinen, and D. M. L. Cooper, "3D visualization and quantification of rat cortical bone porosity using a desktop micro-CT system: A case study in the tibia," *J. Microsc.*, vol. 240, no. 1, pp. 32–37, 2010.

[29] W. Marczak, "Water as a standard in the measurements of speed of sound in liquids," *J. Acoust. Soc. Amer.*, vol. 102, no. 5, pp. 2776–2779, Nov. 1997.

[30] K. I. Maslov, L. M. Dorozhkin, V. S. Doroshenko, and R. G. Maev, "A new focusing ultrasonic transducer and two foci acoustic lens for acoustic microscopy," *IEEE Trans. Ultrason., Ferroelectr., Freq. Control*, vol. 44, no. 2, pp. 380–385, Mar. 1997.

[31] K. Raum and J. Brandt, "Simultaneous determination of acoustic impedance, longitudinal and lateral wave velocities for the characterization of the elastic microstructure of cortical bone," in *Proc. World Congr. Ultrason.*, Paris, France, 2003, pp. 321–324.

[32] J. M. Bland and D. G. Altman, "Statistical methods for assessing agreement between two methods of clinical measurement," *Lancet*, vol. 327, no. 8476, pp. 307–310, 1986.

[33] M. Granke *et al.*, "To what extent can cortical bone millimeter-scale elasticity be predicted by a two-phase composite model with variable porosity?" *Acta Biomaterialia*, vol. 12, pp. 207–215, Jan. 2015.

[34] O. Yousefian, R. D. White, Y. Karbalaeisadegh, H. T. Banks, and M. Müller, "The effect of pore size and density on ultrasonic attenuation in porous structures with mono-disperse random pore distribution: A two-dimensional *in-silico* study," *J. Acoust. Soc. Amer.*, vol. 144, no. 2, p. 709, 2018.

[35] Y. Karbalaeisadegh, O. Yousefian, G. Iori, K. Raum, and M. Müller, "Acoustic diffusion constant of cortical bone: Numerical simulation study of the effect of pore size and pore density on multiple scattering," *J. Acoust. Soc. Amer.*, vol. 146, no. 2, p. 1015, 2019.

[36] M. K. H. Malo *et al.*, "Longitudinal elastic properties and porosity of cortical bone tissue vary with age in human proximal femur," *Bone*, vol. 53, no. 2, pp. 451–458, 2013.

[37] J. S. Nyman, M. Granke, R. C. Singleton, and G. M. Pharr, "Tissue-level mechanical properties of bone contributing to fracture risk," *Current Osteoporosis Rep.*, vol. 14, no. 4, pp. 138–150, 2016.

[38] A. Wydra, E. Malyarenko, K. Shapoori, and R. G. Maev, "Development of a practical ultrasonic approach for simultaneous measurement of the thickness and the sound speed in human skull bones: A laboratory phantom study," *Phys. Med. Biol.*, vol. 58, no. 4, pp. 1083–1102, 2013.

[39] J. Schneider *et al.*, "*In vivo* measurements of cortical thickness and porosity at the proximal third of the tibia using guided waves: Comparison with site-matched peripheral quantitative computed tomography and distal high-resolution peripheral quantitative computed tomography," *Ultrasound Med. Biol.*, vol. 45, no. 5, pp. 1234–1242, 2019.

[40] D. Rohrbach *et al.*, "Distribution of mesoscale elastic properties and mass density in the human femoral shaft," *Connect Tissue Res.*, vol. 56, no. 2, pp. 120–132, 2015.

[41] M. Talmant *et al.*, "*In vivo* performance evaluation of bi-directional ultrasonic axial transmission for cortical bone assessment," *Ultrasound Med. Biol.*, vol. 35, no. 6, pp. 912–919, Jun. 2009.

[42] P. Moilanen *et al.*, "Discrimination of fractures by low-frequency axial transmission ultrasound in postmenopausal females," *Osteoporosis Int.*, vol. 24, no. 2, pp. 723–730, 2013.

[43] W. P. Olszynski *et al.*, "Multisite quantitative ultrasound for the prediction of fractures over 5 years of follow-up: The Canadian multicentre osteoporosis study," *J. Bone Mineral Res.*, vol. 28, no. 9, pp. 2027–2034, 2013.
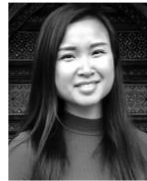
Huong Nguyen Minh (M'19) was born in Berlin, Germany, in 1994. She received the B.Sc. and M.Sc. degrees in medical physics from the Martin Luther University of Halle-Wittenberg, Halle, Germany, in 2015 and 2018, respectively. She is currently pursuing the Ph.D. degree with the Berlin Brandenburg Center for Regenerative Therapies, Charité—Universitätsmedizin Berlin, Berlin.

Ms. Nguyen Minh became a member of the International Bone Ultrasound Society in 2018 and a member of the European Society of Biomechanics in 2019. She was a recipient of the Gustav-Mie-Bachelor-Award for her achievements during the bachelors in 2015.

Juan Du (M'13) was born in Hebei, China, in 1987. She received the B.Sc. degree in control, detection, and navigation from Beihang University, Beijing, China, in 2009, and the M.Sc. and Ph.D. degrees in electrical engineering from the University of Minnesota, Twin Cities, Minneapolis, MN, USA, in 2012 and 2016, respectively.

From 2014 to 2015, she was with the Department of Research and Development, Medtronic, Inc., Minneapolis, developing algorithms for ECG signal processing, the graphic user interface for physicians, and performing ultrasound acoustic field simulation and transducer modeling and optimization, which resulted in four granted U.S. patents. From 2016 to 2018, she was a Postdoctoral Researcher with the Berlin Brandenburg Center for Regenerative Therapies, Charité—Universitätsmedizin Berlin Berlin, Germany. She is currently with Digital Endoscopy GmbH, Friedberg, Germany. Her research interests include ultrasound microvascular imaging, ultrasound acoustics, biomedical-related signal and image processing, DSP design and implementation, and medical device development.

Kay Raum (M'02) was born in Halle, Germany, in 1972. He received the Diploma and Ph.D. (Dr.rer.nat.) degrees in physics from the Martin Luther University of Halle-Wittenberg, Halle, in 1997 and 2002, respectively.

He was a Visiting Scholar with the Bioacoustics Research Laboratory, University of Illinois at Urbana–Champaign, Champaign, IL, USA, from 1995 to 1996. From 1997 to 2003, he was a Research Assistant with the Medical Faculty, Martin Luther University of Halle-Wittenberg. In 2004, he was a Postdoctoral Fellow with the French National Center of Scientific Research, Paris, France, and joined the Laboratoire d'Imagerie Paramétrique, Sorbonne University Pierre and Marie Curie Campus, Paris, France. In 2006, he became the Research Head of the Interdisciplinary Center for Musculoskeletal Diseases, Medical Department, Martin Luther University. In 2009, he was appointed as a Full Professor for engineering basis of regeneration with the Berlin Brandenburg Center for Regenerative Therapies, Charité—Universitätsmedizin Berlin, Berlin, Germany. He has authored over 75 original papers and several book chapters. His research interests include the development and applications of ultrasound and X-ray tomography in musculoskeletal research, diagnosis, and therapy.

Dr. Raum is a Founding Member and a Treasurer of the International Bone Ultrasound Society, a member of the Acoustical Society of America, the Bone Ultrasound Society, the German Society for Biomedical Technology (VDE-DGBMT), and the German Osteology Society. He is an Associate Editor of the journals *Ultrasound in Medicine and Biology* and *Ultrasonic Imaging*.

60

Study B: <u>Nguyen Minh H</u>, Muller M, Raum K. Estimation of Thickness and Speed of Sound for Transverse Cortical Bone Imaging Using Phase Aberration Correction Methods: An In Silico and Ex Vivo Validation Study. Applied Sciences. 2022;12(10):5283. Impact Factor: 2.679

Article

Estimation of Thickness and Speed of Sound for Transverse Cortical Bone Imaging Using Phase Aberration Correction Methods: An In Silico and Ex Vivo Validation Study

Huong Nguyen Minh [1], Marie Muller [2] and Kay Raum [1,*]

[1] Center for Biomedicine, Charité—Universitätsmedizin Berlin, 12203 Berlin, Germany; huong.nguyen-minh@charite.de
[2] Department of Mechanical and Aerospace Engineering, NC State University, Raleigh, NC 27695, USA; mmuller2@ncsu.edu
* Correspondence: kay.raum@charite.de

Abstract: Delay-and-sum (DAS) beamforming of backscattered echoes is used for conventional ultrasound imaging. Although DAS beamforming is well suited for imaging in soft tissues, refraction, scattering, and absorption, porous mineralized tissues cause phase aberrations of reflected echoes and subsequent image degradation. The recently developed refraction corrected multi-focus technique uses subsequent focusing of waves at variable depths, the tracking of travel times of waves reflected from outer and inner cortical bone interfaces, the estimation of the shift needed to focus from one interface to another to determine cortical thickness (*Ct.Th*), and the speed of sound propagating in a radial bone direction (*Ct.v_{11}*). The method was validated previously in silico and ex vivo on plate shaped samples. The aim of this study was to correct phase aberration caused by bone geometry (i.e., curvature and tilt with respect to the transducer array) and intracortical pores for the multi-focus approach. The phase aberration correction methods are based on time delay estimation via bone geometry differences to flat bone plates and via the autocorrelation and cross correlation of the reflected ultrasound waves from the endosteal bone interface. We evaluate the multi-focus approach by incorporating the phase aberration correction methods by numerical simulation and one experiment on a human tibia bone, and analyze the precision and accuracy of measuring *Ct.Th* and *Ct.v_{11}*. Site-matched reference values of the cortical thickness of the human tibia bone were obtained from high-resolution peripheral computed tomography. The phase aberration correction methods resulted in a more precise (coefficient of variation of 5.7%) and accurate (root mean square error of 6.3%) estimation of *Ct.Th*, and a more precise (9.8%) and accurate (3.4%) *Ct.v_{11}* estimation, than without any phase aberration correction. The developed multi-focus method including phase aberration corrections provides local estimations of both cortical thickness and sound velocity and is proposed as a biomarker of cortical bone quality with high clinical potential for the prevention of osteoporotic fractures.

Keywords: medical beamforming; phase aberration correction; medical tissue characterization; pulse-echo ultrasound; medical signal and image processing

1. Introduction

The current standard method for bone strength assessment and fracture risk prediction is based on areal bone mineral density (*aBMD*) measured by dual-energy absorptiometry (DXA) [1]. Although *aBMD* is an important biomarker of bone quality, additional bone factors, including macro- and micro-structural bone parameters, as well as viscoelastic properties, are known to determine individual bone strength; therefore, to quantify these parameters for bone assessment, quantitative ultrasound (QUS) methods have been introduced as nonionizing alternatives. Early bone QUS technologies used dedicated hardware to measure acoustic properties, such as the speed of sound (*SOS*) and broadband ultrasound

attenuation (*BUA*), at anatomical sites that contain mostly trabecular bone, such as the heel [2]. More recent QUS devices are aimed at imaging bone by using dedicated hardware electronics and ultrasound probes. An example of this by Lasaygues et al. developed ultrasonic image reconstruction methods to image the cortical diaphysis of long bones using quantitative ultrasonic tomography [3,4]. Another tomographic approach to image long bones is based on full-waveform inversion [5]. Additionally, Li et al. used Split-Step Fourier imaging to image bone fractures and to monitor bone healing [6]. Furthermore, a Born-based inversion method has been implemented on an ultrasonic wavefield imaging technique to reconstruct internal structures of long bones [7]. Limitations of these studies were that either the speed of sound or the thickness needed to be assumed a priori. Axial transmission devices can retrieve cortical parameters (i.e., porosity, thickness, and speed of sound), by measuring the propagating velocity of dispersive guided waves [8–12]; however, this technique is challenged by large soft tissue thickness, irregular bone shapes, and it does not provide direct image guidance.

A few recent technologies utilize sophisticated array-based pulse-echo imaging technology to estimate *BMD* in trabecular bones at major fracture sites (i.e., spine and proximal femur [13]), or to measure structural and material properties in the cortical bone (i.e., tibia and radius) [14,15]. Most medical ultrasound scanners on the market implement the standard delay-and-sum (DAS) beamforming method to reconstruct the brightness mode (hereinafter called B-mode) images. This technique uses a transducer array to transmit and receive focused ultrasound signals inside the body. Conventionally, the reconstruction of B-mode images using DAS is done by adding time specific delays to the individual ultrasound signals which are received at each element of the receiver array before summing all signals to create a beamformed received signal; therefore, the sensitivity of the beamformed signal can be maximized to a certain depth and direction. In medical ultrasound scanners, transmit and receive focusing is performed by assuming a constant speed of sound of soft tissue (1540 m/s) along the entire sound propagation path. This approximation provides satisfactory image quality for most soft tissues, because the true velocities only vary within 10% when compared with the assumed value [16]; however, this is not the case for mineralized tissues, such as cortical bones. The radial speed of sound in cortical bone is between the range of 2800 to 3500 m/s [17], which results in a substantial refraction at the soft tissue and cortical bone interface. In case of a wrong assumption on the constant sound velocity, the delay estimation, which is necessary to focus on a particular image location, is incorrect, subsequently leading to a phase-distorted DAS signal. As a result, in a conventional B-mode image reconstructed by medical ultrasound scanners, the internal bone structures appear blurred or cannot be reconstructed at all. Aside from radiofrequency echographic multispectrometry (REMS) technology [18], this conventional DAS beamforming is currently used for bone strength assessment and fracture risk prediction. There have been efforts to overcome this false assumption of a constant speed of sound in cortical bone. Renaud et al. [14] proposed the first in vivo image reconstruction of cortical bone using a conventional medical ultrasound scanner and seismic image reconstruction. This reconstruction method provides local estimations of *Ct.Th* and anisotropic sound velocity.

Consequently, the need for further methods brought about the multi-focus (MF) imaging technique, that was developed by our group to measure cortical thickness (*Ct.Th*) and the compressional sound velocity propagating in the radial bone direction ($Ct.v_{11}$) [19]. Our method aims at imaging cortical bone at the central anteromedial tibia. This anatomical site is of clinical interest, as it is easy to access, and is composed of a thick and regular cortical bone shell. Alterations, such as reduced cortical thickness and the occurrence of large intracortical pores, have shown to be associated with reduced hip strength [20] and increased fracture risk [21]. The ultrasonic speed of sound in cortical bone has been proposed as a biomarker of bone quality since the 1970s [22], and is related to bone density and elastic constants, which are correlated to bone quality and fracture risk [23]. The MF method is based upon the consecutive focusing of ultrasound waves at varying depths, followed by the retrieval of focus locations and pulse-travel times of signals reflected from the

periosteal (frontside) and endosteal (backside) cortical bone interfaces using conventional DAS beamforming (Figure 1). So far, the MF method has been validated on plates with constant thickness, positioned parallel to the probe array; however, it is important to extend this, as typical human cortical bones exhibit curvatures at their periosteal and endosteal interfaces. These curvatures introduce a distortion of the propagating wavefronts and the round-trip travel time, resulting in phase distorted beamformed signals. The objective of this research is to analyze the effect of the phase aberration caused by (a) bone curvature, (b) bone tilt with respect to the beam axis, and (c) material inhomogeneities due to the presence of cortical pores on the estimations of $Ct.Th$ and $Ct.v_{11}$. The phase aberration from bone surface curvature leads to a different round-trip travel time when compared with a flat plate bone model (surface time shift, ST), and was corrected using the concept of refraction compensation proposed by Yasuda et al. [24]. Bone tilt, with respect to the beam axis of the transducer array, shows orientation dependence of the received echoes compared with a flat bone interface. Additional time shifts caused by the orientation dependence of received echoes were corrected using autocorrelation analysis (ACF). Differences in the round travel time of the received echoes based on the interaction of ultrasound wave refractions with cortical pores were determined using cross correlation analysis (CC). We show the need to incorporate three phase-aberration correction (PAC) methods for non-plate shaped bone structures by means of numerical finite-difference time-domain (FDTD) simulation models, as well as measurements on a human tibia bone. Precision and accuracy values of estimated $Ct.Th$ and $Ct.v_{11}$ with and without corrections were compared.
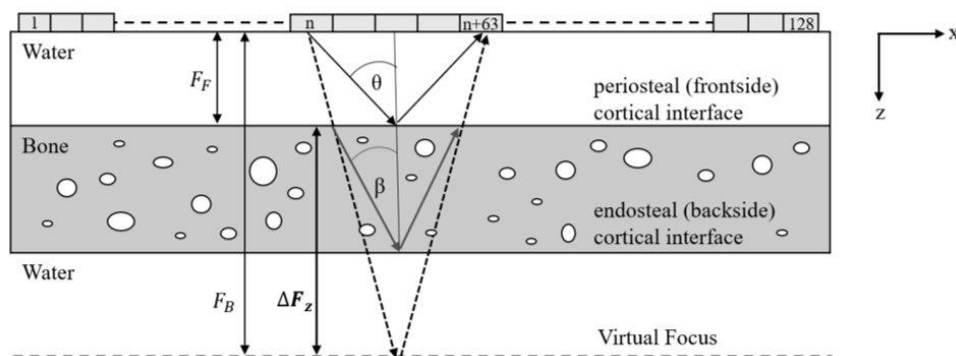

Figure 1. Schematic representation of the multi-focus measurement in the radial direction (x, z) of a long bone. The transducer is placed 15 mm above the sample. Focused sound beams are emitted using a 64-element sub-aperture of a 128-element linear array. The focus is shifted from a depth above the periosteal cortical interface to a depth below the endosteal cortical interface by gradually decreasing the semi-aperture angle θ of the transmit beam. Refraction at the periosteal interface changes the direction of the transmitted waves and results in a shift of the focus depth inside the bone. ΔFz is the focus depth shift required to focus from the periosteal (frontside F_F) to the endosteal (backside F_B) interface. In addition to scanning the focus depth, sub-aperture is scanned in the x-direction along the transducer array (adapted from [19] under the Creative Commons Attribution 4.0 license).

2. Materials and Methods

An overview for all used abbreviations is summarized in Table 1.

Table 1. List of abbreviations.

Abbreviation	Description
$Ct.Th$	Cortical thickness
$Ct.v_{11}$	Cortical compressional sound velocity propagating in the radial bone direction
v_{H2O}	Speed of sound in water
dx	Lateral shift of center of mass of curved bone plate model relative to beam axis
r	Bone plate curvature radius
$Ct.Po$	Cortical porosity
F_z	Focus depth in z-direction
$H_F(F_z)$	Amplitude of Hilbert-transformed envelope signal of beamformed frontside reflection at focus depth F_z
$H_B(F_z)$	Amplitude of Hilbert-transformed envelope signal of beamformed backside reflection at focus depth F_z
FB	Front- and backside reflection
ΔTOF	Shift in time-of-flight between peak position of $H_F(F_z)$ and $H_B(F_z)$
ΔF_z	Shift in focus depth between peak position of $H_F(F_z)$ and $H_B(F_z)$
$F_{z,B}$	Confocal focus depth position of backside reflection
θ	Semi-aperture angle of transmit and receive beams
k_{eff}	Correction factor k_{eff} for effective aperture $k_{eff}\theta$
θ_{crit}	Critical angle based on Snell's law
$\Delta\theta$	Difference of the semi-aperture angle to the critical angle
Tx_i, Rx_i	Transmit or receive channel number
Rx_{ref}	Reference receive channel with maximum amplitude at envelope signal of pre-beamformed backside reflection
V_{gb}	Gated pre-beamformed backside reflection signals
V_{ACF}	Signal after using autocorrelation function (ACF)
$\|V_{ACF}\|$	Magnitude of the ACF signal
α_{ACF}	Inclination angle of the fitted ellipsoid on V_{ACF} to the major semi-axis
Δt_{ACF}	Time shift correction based on α_{ACF}

2.1. Numerical Ultrasound Propagation Model

Ultrasound wave propagation in bone and water was simulated using a 2D finite-difference time-domain (FDTD) code (Simsonic, www.simsonic.fr, accessed on 10 March 2022) [25]. The simulation model considers elastic wave propagation including mode conversion, multiple scattering, frequency-independent absorption, refraction, and diffraction. A convergence study, as described in [19], provided stable results at grid sizes of 7 μm and time steps of 0.93 ns. Table 2 shows the material properties used for the models in this study. Material properties were used from an ex vivo study [26] and a previous acoustic microscopy study in a human femoral cortical bone [27]. All bone models were simulated as hollow cylinders immersed in water. The cylinders were defined by an outer curvature radius r and a wall thickness d. All bone models were placed 15 mm below a linear array with 64 transmitter and receiver elements (element and pitch sizes: 0.3 mm); therefore, the models assumed the sound propagation in the transverse image plane (i.e., perpendicular to the bone's long axis, at the antero-medial midshaft of a tibia, where the outer bone surface is flat or slightly curved and the sound velocity of the tissue matrix can be assumed to be isotropic in the simulation plane). The transducer elements emitted broadband pulses with a center frequency of 4 MHz and a −6-dB bandwidth of 60%. Phase delays were applied to focus the transmit beam consecutively, at depths ranging from 13 mm to 40 mm, with an increment of 1 mm. The signals received by all elements were captured and downsampled to a sampling rate of 80 MHz for further processing. The sufficient aperture size of 64 was chosen based on a side study, which can be found in Appendix A.

Table 2. Tissue material properties of bone and pores used for the numerical model. Mass density ρ, and c_{ij} (i.e., the coefficients of a transverse isotropic stiffness tensor were taken from [27] and the absorption value α was obtained from [26]) (adapted from [19] under the Creative Commons Attribution 4.0 license).

	Bone	Pores/Water
ρ [g/cm^3]	1.93	1.00
c_{11} [GPa]	23.7	2.25
c_{22} [GPa]	23.7	2.25
c_{12} [GPa]	9.5	2.25
c_{66} [GPa]	6.6	0
v_{11} [m/s]	3504	1500
α [dB/mm]	2.1	0.002

2.1.1. Reference Bone Model: Flat Bone Plate

The reference model consisted of a 4 mm thick bone plate ($Ct.Th^{Ref}$ = 4 mm) without pores. The material properties of the homogenous bone material results in a reference speed of sound of $Ct.v_{11}{}^{Ref}$ = 3504 m/s. The curvature radius of r = 10 m was used to simulate a flat bone plate (hereinafter simply called 'flat bone plate'). The radius of 10 m was deemed sufficiently large to exhibit a negligible curvature within the simulation region (Figure 2a).
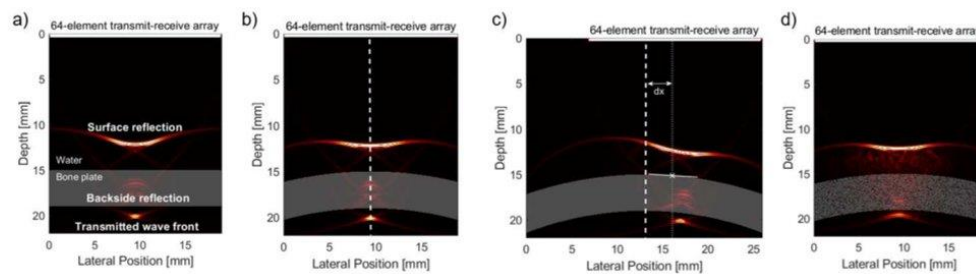

Figure 2. (**a**) Snapshot of the flat bone plate simulation model at 13.5 µs. Transmitted and reflected wavefronts of a beam generated with a 64-element aperture and focused to a depth of 25 mm can be seen. (**b**) Snapshot of the curved plate model with a curvature radius of 40 mm. (**c**) Snapshot of the curved plate model *r40dx3.11* with vertical bone symmetry axes being marked by a white dashed line, beam axis is shown by the grey dashed line, and the cross point of the beam axis with the frontside surface is marked as white. (**d**) Snapshot of *r40dx0Po16* with a cortical porosity of 16% and pore diameter 60 µm at focal depth of 25 mm.

2.1.2. Bone Curvature

To investigate the effect of bone curvature, curved bone plate models were simulated and compared with the flat bone plate model (Figure 2b). Five curved bone models with radii of r = 60 mm, 50 mm, 40 mm, 30 mm, and 20 mm were simulated. The radius range was defined based on a previous study, in which human tibia midshaft bones of 55 postmenopausal women were measured by means of high-resolution peripheral computed tomography (HR-pQCT) [15]. In that study, the anteromedial tibia midshaft region had been chosen as the ultrasound measurement site due to the small amount of overlying soft tissue and the small curvature of the bone surface compared with other tibia regions. To estimate the curvature radius, circular fits were performed on the central anteromedial tibia region. Tibia bone curvature radii were found to be in the range between 12.6 mm and 68.8 mm with a mean radius of 30.3 mm. Three examples of the circular fits on the HR-pQCT scans are shown in Figure A2 of Appendix B, where the subjects with a minimum (Figure A2a), mean (Figure A2b), and maximum curvature radius (Figure A2c) were selected.

2.1.3. Bone Tilt

To study the effect of the angle of incidence, a bone surface tilt was incorporated by shifting the lateral position of the transducer array by dx (Figure 2c). The bone surface tilt was defined as the angle between the normal vector of the periosteal bone surface and the beam axis at their crossing point.

2.1.4. Material Inhomogeneity: Cortical Pores

To study the effect of material inhomogeneity, cortical pores were included in the curved bone plate models (Figure 2d). Previous ex vivo studies in human cortical bone reported cortical porosity ($Ct.Po$) and cortical pore diameter ($Ct.Po.Dm$) values between 2% and 22% and 7 and 95 μm, respectively [28–30]. Cortical pores were defined as circular pores with $Ct.Po.Dm$ = 60 μm and varying pore densities, resulting in models with $Ct.Po$ values ranging from 0% to 20% with an increment of 2%.

For the simulation models with cortical pores, transmission measurements were performed to calculate the reference speed of sound $Ct.v_{11}^{Ref}$. An unfocused single-element transducer with a width of 0.3 mm emitted ultrasound waves with a center frequency of 4 MHz and a −6-dB bandwidth of 60%. The unfocused ultrasound wave traveled though the bone and the transmitted ultrasound wave was captured by a single element detector with a width of 0.3 mm, which was placed below the bone. The transducer and detector were placed at the beam axis of the reference MF simulation. In addition, a simulation was performed with the same configuration without the bone to measure the reference signal transmitted though water. The time-of-flight of the ultrasound wave transmitted through water TOF_{H20} and bone TOF_{bone} was defined at the time of the maximum of the signal envelope. The $Ct.v_{11}^{Ref}$ of the bone models with pores were calculated using the following equation from [31].

$$Ct.\degree_{11}^{Ref} = \frac{Ct.Th_{bone}}{\frac{Ct.Th_{bone}}{\degree_{H_2O}} + \left(TOF_{bone} - TOF_{H_2O}\right)}, \tag{1}$$

with $Ct.Th_{bone}$ = 4 mm.

2.2. Ex Vivo Measurement on a Human Tibia Bone

One left tibia bone from a human cadaver (female, age 85) was used for the ex vivo validation. The bone sample was received without the soft tissue and distal end (cut off at approximately 50%). The sample was collected by the institute of Anatomy, University of Lübeck, Germany, in accordance with the German law "Gesetz über das Leichen-, Bestattungs- und Friedhofswesen des Landes Schleswig-Holstein II Abschnitt, §9 Leichen-öffnung, anatomisch", from 2 April 2005. A 30 mm disk was cut from the tibia midshaft using a band saw (EXACT GmbH, Remscheid, Germany). A HR-pQCT scan was performed (XtremeCT II, Scano Medical AG, Bassersdorf, Switzerland) with a total scan length of 10.2 mm in the axial direction and an isotropic voxel size of 60.7 μm. Cortical thickness at the anteromedial tibia section was extracted using a custom protocol adapted from Iori et al. [32] and used as reference value. Cortical porosity was calculated from the HR-pQCT scan using the algorithm proposed by Burghardt et al. [33]. A site-matched multi-focus measurement was performed using a medical scanner SonixTouch equipped with a 3D linear array transducer 4DL14-5/38 (consisting of a 1D 128 element array) and a SonixDAQ single-channel data acquisition system (Ultrasonix, Richmond, BC, Canada). The SonixDAQ allows the pre-beamformed single-channel radio frequency (RF) data acquisition of all channels without any signal processing. The sample was immersed in water and the transducer array was positioned perpendicular to the bone's long axis. The multi-focus measurement sequence consisted of a series of conventional B-mode imaging sequences with 128 lateral scan positions. At each scan position, sound waves were focused on the radial bone where the direction was into the tibia sample using a 64-element transmit aperture. Subsequent B-mode images were acquired using 17 gradually increasing focus

depths (starting from 14 mm with a step size of 2 mm). The transducer elements were excited with a "+−" signal at a system transmit frequency of 4 MHz to optimize the penetration depth. Single-channel RF data were captured with all 128 array elements at a sampling rate of 40 MHz with a 12-bit resolution.

2.3. Signal Processing

2.3.1. Reference Bone Model: Flat Bone Plate

Details of the multi-focus signal processing steps have been described previously [19]. From the delay and beamformed (DAS) Hilbert-transformed envelope signal, the amplitudes [$H_F(F_z)$ and $H_B(F_z)$] and pulse travel times [$TOF_F(F_z)$ and $TOF_B(F_z)$] of the signals reflected from the front- and backsides of the plate were tracked for each beam focus position F_z. The time-of-flight difference between front- and backside reflections was defined as $\Delta TOF = TOF_B(F_z) - TOF_F(F_z)$. Spline interpolation was used to estimate $H_F(F_z)$ and $H_B(F_z)$ at an F_z increment of 0.1 mm. The interpolated data, and the front- and backside focus positions F_F and F_B, respectively, were retrieved from the peak positions of $H_F(F_z)$ and $H_B(F_z)$, and ΔF_z (i.e., the shift needed to focus either on the front- or backside of the plate, and to estimate the time delay between front- and backside reflections ΔTOF). $Ct.Th$ and $Ct.v_{11}$ were estimated using Equation (3) in [19] with sound velocity in water v_{H20}:

$$Ct.Th = \frac{\Delta F_z}{0.5 \cdot \frac{Ct.v_{11}}{v_{H_2O}} \cdot \left(1 - \frac{Ct.v_{11}^2}{v_{H_2O}^2}\right) \cdot \left(1 - \cos\left(k_{eff}\theta\right)\right) - \frac{Ct.v_{11}}{v_{H_2O}}}, \tag{2}$$

where θ is the semi-aperture angle of the transmitting and receiving beams, and k_{eff} is an effective aperture contributing to the beam focusing on the backside of the plate. The effective aperture accounts for the increased conversion of compressional waves into shear waves with increasing inclination angles and the absence of compressional wave transmission into the bone tissue for inclination angles larger than the critical angle θ_{crit} [19]:

$$\theta_{crit} = \sin^{-1}\left(\frac{v_{H_2O}}{Ct.v_{11}}\right). \tag{3}$$

In contrast to our previous study [19], we have used an aperture size of 64 elements and adjusted the factor to estimate the effective aperture k_{eff} from 0.1 to 0.122:

$$k_{eff} = \begin{pmatrix} 1 & if \ \theta < \theta_{crit} - 10° \\ 0.122 \cdot \Delta\theta & if \ \theta > \theta_{crit} - 10° \end{pmatrix}. \tag{4}$$

More details on the estimation for k_{eff} can be found in Appendix A.

2.3.2. Phase Aberration Correction

Phase aberrations caused by bone curvature, bone tilt and material inhomogeneities are corrected for signals reflected from the backside cortical bone interface. Three phase-aberration correction (PAC) methods are used: (1) The curved bone surface geometry results in different round-trip travel times compared with the flat bone model. A time-shift correction based on the periosteal bone surface geometry (hereinafter called 'surface time correction' ST), was used to correct for the additional ultrasound wave propagation paths in the water due to the bone curvature. The ST correction used the concept of refraction compensation proposed by Yasuda et al. [24]. Further details are summarized in Figure A3a in Appendix C. (2) For tilted bone models, the reflected wavefront exhibits a tilt with respect to the beam axis (Figure 2c). To correct the phase aberration caused by surface inclination, an autocorrelation function (ACF) analysis on the reflected backside echoes was performed (Figure A3b–d in Appendix C). (3) Local variations of the sound velocity caused by material inhomogeneities lead to small fluctuations of the transit time measured at individual receiver elements and subsequently to a distortion of the summed signal;

therefore, the following method was used to estimate the backside focus depth. The arrival times for all receiver elements was estimated using a cross-correlation (CC) method. The receiver channel that measured the highest signal amplitude was used as the reference signal. The inter-element arrival times exhibit either a concave, flat, or a convex shape, depending on the distance of the beam focus relative to the backside bone interface. A second-order polynomial was fitted to the inter-element arrival times, and the confocal focus depth was determined by finding the zero-crossing point of the second order fit coefficients (Figure A3e,f in Appendix C). This zero-crossing point was used to determine ΔF_z, and to estimate $Ct.Th^{MF}$ and $Ct.v_{11}^{MF}$ using Equation (2).

2.4. Statistics

For each model, the retrieved $Ct.Th^{MF}$ and $Ct.v_{11}^{MF}$ values were compared with the reference $Ct.Th^{Ref} = 4$ mm and $Ct.v_{11}^{Ref}$. Simulation models without cortical pores had the reference speed of sound of $Ct.v_{11}^{Ref} = 3504$ m/s. The bone models with cortical pores $Ct.v_{11}^{Ref}$ were extracted from the transmission measurements. Pearson linear regression analysis was performed to compare the parameters obtained using the multi-focus method with reference values. For all models with a 64-element aperture, the relative error (RE), precision, and accuracy values for each PAC method were determined and compared with the values without any PAC. Precision was defined as the coefficient of the variation of the difference between the predicted $Ct.Th^{MF}$, $Ct.v_{11}^{MF}$ and the reference values for $Ct.Th^{Ref}$, $Ct.v_{11}^{Ref}$. Accuracy was determined by means of the root mean square error (RMSE) compared with the reference values. All analyses were performed using MATLAB R2019b, including the Signal Processing, Curve Fitting, and Statistics Toolboxes (The Mathworks, Natick, MA, USA).

3. Results

3.1. Numerical Simulations

A total of 22 bone models were simulated (Table A2 in Appendix D). The reference sound velocities $Ct.v_{11}^{Ref}$ of the porous models, as determined by transmission simulations, are summarized in Table A3 in Appendix D. The estimated $Ct.Th^{MF}$ and $Ct.v_{11}^{MF}$ values for all models and the relative errors are summarized in Table A4 in Appendix D. Without PAC, all deviations from the ideal flat plate geometry led to deteriorations of precision and accuracy. In most situations, PAC improved both the precision and accuracy (Tables 3 and 4), which will be described in more detail in the following sections.

Table 3. Precision of $Ct.Th^{MF}$ and $Ct.v_{11}^{MF}$ after each PAC method.

	Model	No PAC	ST	ST + ACF	ST + ACF + CC
$Ct.Th^{MF}$	Curved bone plate	4.3%	1.7%	1.4%	2.0%
	Curved tilt bone plate	2.3%	7.3%	4.3% (4.2%) *	4.3% (1.1%) *
	Material inhomogeneity	18.5%	1.4%	4.7%	7.2% (1.9%) **
$Ct.v_{11}^{MF}$	Curved bone plate	4.3%	1.6%	1.4%	2.0%
	Curved tilt bone plate	2.3%	7.1%	4.2% (2.5%) *	4.3% (0.8%) *
	Material inhomogeneity	15.9%	7.9%	7.9%	8.2% (7.9%) **

* Exclusion of bone models with tilt angles over 7°. ** Exclusion of bone model with porosity 20%.

Table 4. Accuracy of $Ct.Th^{MF}$ and $Ct.v_{11}^{MF}$ after each PAC method.

	Model	No PAC	ST	ST + ACF	ST + ACF + CC
$Ct.Th^{MF}$	Curved bone plate	10.2%	2.2%	1.9%	1.8%
	Curved tilt bone plate	9.6%	10.3%	5.2% (1.3%) *	5.2% (1.2%) *
	Material inhomogeneity	23.2%	14.6%	6.3%	8.3% (3.5%) **
$Ct.v_{11}^{MF}$	Curved bone plate	10.4%	2.4%	2.1%	1.9%
	Curved tilt bone plate	9.8%	10.1%	5.1% (1.4%) *	5.1% (1.2%) *
	Material inhomogeneity	25.3%	3.4%	3.4%	2.8% (3.0%) **

* Exclusion of bone models with tilt angles over 7°. ** Exclusion of bone model with porosity 20%.

3.1.1. Effect of Bone Curvature

All three PAC methods showed improvements of $Ct.Th^{MF}$ and $Ct.v_{11}{}^{MF}$ estimations with respect to precision and accuracy (Tables 3 and 4). Although the ST correction alone showed the strongest improvement, the combination of all three PAC only yielded slight further improvements.

3.1.2. Effect of Bone Tilt

To correct for the bone tilt, using ST correction was not sufficient, and it even degraded accuracy and precision values (Tables 3 and 4). The wavefront inclination caused by the tilted surface was effectively corrected using the ACF; however, for bone models with tilt angles above 7°, the CC correction method failed, because no zero-crossing point for the estimation of confocal focus depth could be retrieved (Figure A4c in Appendix D). After excluding these models, precision values for $Ct.Th^{MF}$ and $Ct.v_{11}{}^{MF}$ were 1.1% and 0.8%, respectively, and accuracy values were 1.2% for both the $Ct.Th^{MF}$ and $Ct.v_{11}{}^{MF}$ estimations.

3.1.3. Effect of Material Inhomogeneities

The presence of pores strongly degraded accuracy and precision values without PAC. The ST correction strongly improved precision and accuracy. Additional ACF correction had no effect in the evaluated simulations, because all porous bone models were modeled without a tilt. The CC further improved precision and accuracy values for $Ct.Th^{MF}$ and $Ct.v_{11}{}^{MF}$. For the bone model with the highest porosity value of 20%, all PAC methods did not result in a precise and accurate estimation of $Ct.Th^{MF}$ and $Ct.v_{11}{}^{MF}$ (Table A4 and Figure A5 in Appendix D).

3.1.4. Overall Effect of PAC

Table 5 shows the precision and accuracy values for all 22 simulation models. Note that precision values are defined as the coefficient of variation of the difference between the estimated and reference value of the flat bone plate model and accuracy is defined as RMSE as a percentage. That means the smaller the precision and accuracy value, the more precise and accurate the parameter estimation is with respect to the reference value. Overall, the combination of the three PAC methods results in an improved precision and accuracy estimation $Ct.Th^{MF}$ and $Ct.v_{11}{}^{MF}$. Precision values for $Ct.Th^{MF}$ and $Ct.v_{11}{}^{MF}$ were 5.7% and 9.8%, respectively. Accuracy values for $Ct.Th^{MF}$ and $Ct.v_{11}{}^{MF}$ were 6.3% and 3.4%, respectively.

Table 5. Precision and accuracy of $Ct.Th^{MF}$ and $Ct.v_{11}{}^{MF}$ for each PAC method for all 64-element aperture models. Reference thickness for all models is $Ct.Th^{Ref}$ = 4 mm. Models without cortical pores have $Ct.v_{11}{}^{Ref}$ = 3504 m/s. Reference values $Ct.v_{11}{}^{Ref}$ for models including cortical pores can be found in Table A3 in Appendix D.

	Correction	Precision	Accuracy
$Ct.Th^{MF}$	No	17.4%	17.1%
	ST	10.3%	11.2%
	ST + ACF	4.1%	5.2%
	ST + ACF + CC	5.7% (2.1%) *	6.3% (2.6%) *
$Ct.v_{11}{}^{MF}$	No	11.6%	18.5%
	ST	9.5%	5.9%
	ST + ACF	9.5%	3.7%
	ST + ACF + CC	9.8% (9.6%) *	3.4% (2.3%) *

* Exclusion of bone models with tilt angles over 7° and/or porosity above 20%.

3.2. Ex-Vivo Multi-Focus Measurement

Reference cortical thickness and porosity values of the human tibia bone at the central anteromedial part were found to be $Ct.Th^{Ref}$ = (2.65 ± 0.61) mm and 15.1%, respectively, using HR-pQCT. For the MF measurement, $Ct.Th^{MF}$ and $Ct.v_{11}{}^{MF}$ were determined in a manually selected region of interest (Figure 3a green ROI). The maximum amplitudes over

all focus depths with and without PAC methods (ST + ACF + CC) are shown in Figure 3a,b. The endosteal surface of the human tibia sample is more blurred in the maximum projection image without PAC methods (Figure 3a). Without PAC, $Ct.Th^{MF}$ and $Ct.v_{11}^{MF}$ could be retrieved at 14 lateral scan positions, whereas with PAC, cortical parameter estimations were achieved at 29 scan positions. The mean and standard deviation of $Ct.Th^{MF}$ without PAC was (2.39 ± 0.25) mm, which was significantly different from the reference value. In contrast, the estimation of $Ct.Th^{MF}$ with PAC of (2.71 ± 0.22) mm was not significantly different from the reference value. The estimated cortical speed without and with PAC were (2870 ± 95) m/s and (2857 ± 52) m/s, respectively.
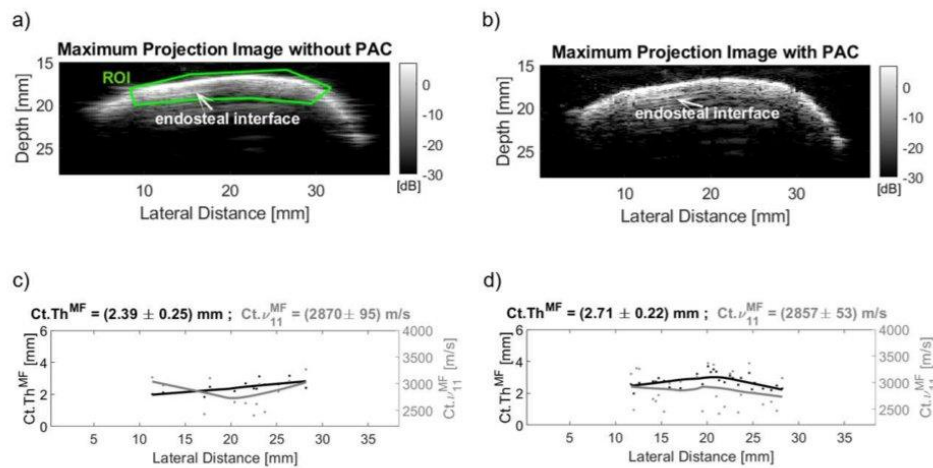

Figure 3. (**a**) Maximum projection B-mode image of human tibia bone at the central anteromedial region. The image was reconstructed and spatially compounded (by means of maximum projection) from measurements at all focus depths using conventional DAS beamforming. The range of interest (ROI) was manually selected (green lines). (**b**) Maximum projection B-mode image reconstructed from all focus depths with PAC (ST, ACF, CC). (**c**) Representative plots of $Ct.Th^{MF}(x_i)$ and $Ct.v_{11}^{MF}(x_i)$ without PAC and (**d**) with PAC. The dots indicate the estimations for each individual lateral scan position x_i, and the straight lines are the estimations using a moving average filter. Means and standard deviations were determined from smoothed data. The number of individual scan positions contributing to the parameter estimations in (**c**,**d**) were 14 and 29, respectively.

4. Discussion

In this study, we have extended the estimations of thickness and speed of sound in cortical bone in a transverse plane using the multi-focus approach to realistic bone geometries. For this, several phase aberration corrections were proposed. The effects of bone curvature, surface inclination relative to the beam axis, and the presence of intracortical pores' parameter estimations were analyzed.

4.1. Numerical Simulation

4.1.1. Effect of Bone Curvature

For curved bone models positioned parallel to the probe array (without bone tilt), the ST correction was sufficient and corrected the additional geometrical time shifts for curved bone interfaces compared to a flat bone plate. For the correction, it was assumed that ultrasound waves propagate in a straight direction, as described in ray theory [34].

4.1.2. Effect of Bone Tilt

Additional phase aberration corrections on the backside echoes were necessary for the curved models with bone tilt relative to the beam axis, to correct the orientation dependence of the reflected wavefront. Here, autocorrelation function was used on the backside echoes to estimate the inclination of the backside echoes; therefore, an ellipsoid was fitted on the magnitude of the backside signals after autocorrelation analysis.

4.1.3. Effect of Material Inhomogeneities

Cortical pores result in scattering and subsequent diffusion of the ultrasound waves. This causes local fluctuations of the arrival time of the received backside echoes compared with the reference flat bone plate model. The backside confocal depth, which is required for the simultaneous estimation of both thickness and sound velocity, has been estimated in our previous work by detecting the peak position of the DAS beamformed backside echoes with respect to the focusing depth [19]. Phase aberration induced by cortical pores cause a decrease in the intensity of the beamformed signal. With increasing porosity, the confocal peak arising from the backside reflection becomes less sharp and the peak position is harder to detect; therefore, we have developed another method to extract the confocal backside position by analyzing the curvature of the backside echo wavefront prior to the summation of all receive channels at each focus depth. The curvature of the wavefront was extracted by analyzing the cross correlation of the backside echoes relative to the backside echo with the highest signal amplitude. The change of the wavefront curvature from a convex shape (negative curvature) to a concave shape (positive curvature) was used to extract the focus position. The zero-crossing point was calculated using a linear fit of the retrieved curvature values over the focus depth. Incorporating cross correlation analysis prior to the summation of the beamformed signals improved the accuracy of the estimation of the backside confocal position, as well as precision and accuracy in simulations including pores (Table 5). Moreover, this method improved the backside signal detection rate and the accuracy of the estimation of cortical thickness in the ex-vivo measurement.

4.1.4. Combination of Phase Aberration Methods

For the transition to in-vivo applications of the multi-focus method, the combination of all three PAC methods is necessary, because all the investigated deviations from an ideal flat homogenous plate are present in real cortical bone. Overall, the combination of the three PAC showed a strong improvement of precision and accuracy values for cortical thickness and speed of sound estimations than when compared to the values without PAC.

4.2. Ex Vivo Measurement

The endosteal surface of the human tibia sample was tracked with and without PAC methods; however, more endosteal surface locations were retrieved when PAC was used. The cortical thickness measured by ultrasound was consistent with the reference value measured by HR-pQCT. The cortical sound velocity of (2857 ± 53) m/s was in the range of the cortical speed of sound values typically found in human cortical bone [17]. Our previous study showed a dependency of cortical speed of sound on cortical porosity (Po) $Ct.\nu_{11}^{fit} = 0.39 \cdot Po^2 - 51.4 \cdot Po + 3485$ [m/s], Figure 6a in [19]). By inserting the reference cortical porosity value of 15.1% obtained from HRpQCT into this equation a speed of sound value of $Ct.\nu_{11}^{fit} = 2804$ m/s was determined for the human tibia sample. The MF-based estimation was in the range of the expected speed of sound value; however, this observation needs to be confirmed in a larger sample size. In conclusion, the ex vivo measurement on a human tibia sample suggests the ability to measure cortical thickness and speed of sound using the MF approach by incorporating PAC methods.

4.3. Transition to In Vivo Application

Cortical bone has been proposed as significant predictor of a bone's mechanical strength because mechanical force given to a bone is carried primally by cortical bone [35].

Clinical studies showed an improvement of fracture prediction by measuring cortical thickness [36–38]. HR-pQCT is the most precise modality to measure cortical thickness at the tibia with a precision of 1.6% [38]. Our study showed a thickness precision estimation of 5.7%. We expect that the clinical precision of the MF approach could be larger than for controlled simulations; however, HR-pQCT uses ionizing radiation and is extremely expensive compared with ultrasound imaging. Wydra et al. [39] proposed a similar refraction measurement method and reported precision values for *Ct.Th* of 8.5% for measurements on porous plate-shaped skull bone phantoms. In contrast, our study considered bone curvature and bone tilt with a better precision value of 5.67%, which can be attributed to the PAC methods, the use of a higher frequency (4 vs. 2.25 MHz), and the consideration of an effective aperture [19].

In addition to cortical thickness, ultrasonic wave-speed in cortical bone has been proposed as a biomarker for bone quality [10,40–42]. Bidirectional axial transmission techniques use a probe with several ultrasonic transmitters and receivers to measure waves traveling in the longitudinal direction of long bones. An in vivo study by Minonzio et al. used a bidirectional axial transmission technique (BDAT) to estimate the cortical thickness and porosity, and they reported those parameters as suitable biomarkers for fracture discrimination in postmenopausal women [43]. The QUS device Bindex$^{®}$ calculates the apparent cortical thickness at the distal radius and tibia using BDAT and reported the correlation with BMD (r $\geq$ 0.71, p < 0.001, 0.20 < R^2 < 0.55) [44]. Talmant et al. [41] showed that the velocity of the first arriving signal (vFAS) is a significant biomarker for fracture discrimination and to predict fracture risk in vivo. Inter-operator precision (repeated measurements by different operators) for FAS velocities were reported at ~7%, respectively. In our study we report the precision value for different simulation models (precision of radial cortical speed of sound was 9.8%), which have been simulated only once. Compared with axial transmission techniques, the multi-focus measurement estimates cortical thickness and speed of sound within the imagined plane and provides image guidance.

Another approach to measure *Ct.Th* and $Ct.v_{11}$ using corrected refraction was proposed by Renaud et al. [14] using a single-element excitation, full-array waveform capture, and an adapted Kirchhoff migration developed by seismologists to image the earth subsurface. The method was validated in vivo on two young healthy subjects. No precision or accuracy values were reported. In two separate studies, Karjalainen et al. [11,45] proposed the estimation of an apparent *Ct.Th* from *TOF* between periosteal and endosteal bone interface at the tibia using a constant predefined speed of sound in cortical bone of 3565 m/s. This approach fails to capture the microstructural changes in porous bone structures and changes in $Ct.v_{11}$. In contrast, our method estimates *Ct.Th* and $Ct.v_{11}$ independently; however, in this study, a very simple pore structure was assumed. Further studies should therefore target bone models with more realistic pore diameter distributions.

Recently, Iori et al. proposed a cortical backscatter model to retrieve the intracortical pore size distribution non-invasively in the tibia midshaft [46]. These findings were further supported by another study on the same set of bones, which suggested that cortical thinning and backscatter parameters describing the presence and accumulation of large cortical pores in the tibia provide similar or better predictions of proximal femur stiffness and ultimate force than *aBMD* [20]. The cortical backscatter (CortBS) method has been applied for the first time in vivo by Armbrecht et al. [15] on postmenopausal women with low bone mineral density. The study reported a better discrimination performance for vertebral and non-vertebral fragility factures using cortical backscatter parameters (0.69 $\leq$ AUC $\leq$ 0.73) compared with DXA based *aBMD* (0.54 $\leq$ AUC $\leq$ 0.55). As the CortBS and multi-focus measurement modalities can be implemented in the same device, future in-vivo studies should be performed to evaluate if such a multiparametric assessment of macro- and microstructural (i.e., *Ct.Th* and intracortical pore size, respectively) and viscoelastic (i.e., $Ct.v_{11}$ and attenuation coefficient $\alpha(f)$) cortical bone properties can improve the discrimination and risk prediction performance for distinct types of fragility fractures.

The combined estimation of *Ct.Th*, *Ct.v*$_{11}$ and pore size distribution using nonionizing and noninvasive technique may have a high clinical potential to prevent osteoporotic fractures.

4.4. Limitations

Several limitations of the proposed PAC methods were observed in this study. The methods fail for bone inclination angles larger than 7° with respect to the beam axis, as well as for the bones with high porosity values (20% or more). For bone models with tilt angles larger than 7°, most backside echoes were not captured by the receiver array resulting in a much smaller DAS beamformed signal and the transition from convex to concave shape of the backside signal wavefront disappeared. Subsequently, the zero-crossing point could not be retrieved (Figure A4c in Appendix D). As the bone surface inclination in the imaging plane can be reliably reconstructed, the application of the PAC methods can be easily restricted to locations, in which the surface inclination is within ±7°. Second, the simulation study was restricted to one scan position for one multi-focus measurement, while the ex vivo measurement performed the multi-focus measurement at 128 scan positions along the lateral distance; therefore, future in silico studies should simulate multi-focus measurements with more scan positions along the lateral distance and include simulation models with real bone curvature, tilt, and porosity. Moreover, compound imaging with beam steering [15,46] should be used to ensure that the bone area of interest is probed with sufficiently small beam inclinations. Third, for high porosity values, large amounts of scattering of ultrasound waves resulted in a strong attenuation and distortion of the backside signal, yielding an imprecise estimation of the confocal backside position (Figure A5c in Appendix D).

Another limitation is the use of simplified bone models. For in vivo transition, the effect of heterogeneous cortical pores and heterogeneous backside surface on the phase aberration should be investigated. Cortical pores lead to increased scattering, and there-fore, increased phase aberration, which could be corrected with cross correlation analysis. Furthermore, the effect of changes regarding the speed of sound in soft tissue should be considered in the future, based on realistic simulation models. Conventional image reconstruction assumes an invariant speed of sound of 1540 m/s. Although the higher and variable velocity in bone was considered, soft tissue velocities can also vary by up to 10% between subjects depending on the relative distribution of skin, fat, and connective tissue along the bone length [16]. This leads to additional wave distortion, defocusing of bone regions, and misalignments of beamformed signals. Anderson et al. [47] showed on a tissue-mimicking phantom that a speed of sound error up to ±8% degrades the lateral resolution of the image by up to a factor of three. The mismatch between the assumed and actual speed of sound could be compensated for by evaluating the focus quality using the coherence factor proposed by Hasegawa et al. [48] or by using the minimum average sum of absolute differences between all pre-beamformed radio frequency channel data proposed by [49]. Renaud et al. proposed an autofocused method to estimate the optimal speed of sound of the overlaying soft tissue [50]. Additional phase aberration corrections by tissue structure may improve lateral resolution, signal quality and the accuracy and precision of the measured time-of-flight through the bone for in vivo transition measurements.

Another limitation of this study is the non-repeated measurement design. Only one simula-tion was performed for each simulation model and the ex vivo measurement was performed once; therefore, for the reproducibility and precision of the multi-focus method for realistic bone simulations, ex vivo and in vivo measurements should be investigated in the future, by repeating the measurements by repositioning of the transducer between each measurement.

5. Conclusions

This study demonstrates the assessment of cortical thickness and speed of sound in the radial direction using refraction- and phase-aberration corrected MF imaging. Conventional DAS beamforming was improved using phase aberration correction methods to account for bone curvature, bone tilt, and bone material homogeneities from cortical pores. The

method was developed and validated using in silico simplified bone models with and without pores, and one ex vivo measurement was performed on a human tibia cadaver. For a reliable in vivo estimation of cortical thickness and speed of sound values, the real bone structures and soft tissue velocity inhomogeneity must be considered. The derived parameters showed an improvement in precision and accuracy using phase aberration corrections and demonstrated good agreement with reference values.

6. Patent

K.R. has the patent "CortBS: Ultrasonic method for determining pore dimensions in cortical bone" pending.

Appendix A. Effect of Aperture and Semi-Aperture Angle θ

The multi-focus (MF) method was introduced in [19] using a 32 element transducer for in silico validation. The bone plates were placed 4 mm below the linear array transducer. In vivo ultrasound measurements on postmenopausal women demonstrated in the study of Armbrecht et al. [15] showed larger bone to transducer ranges up to 30 mm; therefore, simulation models in this study were performed for a realistic transducer/bone distance of 15 mm. To study the effect of the aperture size on the estimations of cortical thickness ($Ct.Th$) and cortical speed of sound ($Ct.v_{11}$), simulation models were created with different transducer array sizes (varying from 32 to 72 elements in increments of 4 elements). For all models a flat bone plate was placed 15 mm below the transducer.

The tracked backside echo amplitudes for the bone plate model with aperture from 32- to 72-element are shown in Figure A1.
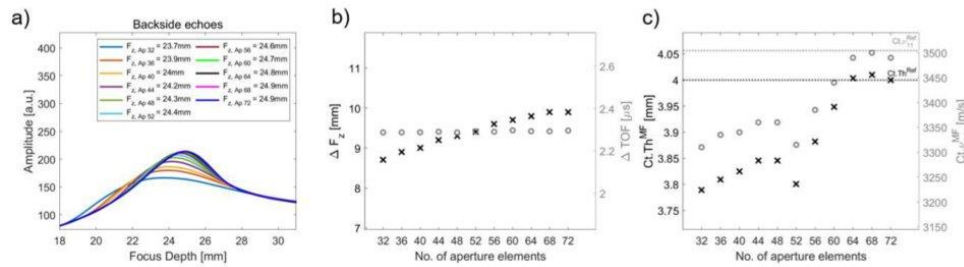
Figure A1. (**a**) Backside echoes simulated with different aperture sizes of a 4-mm flat bone plate model versus focus depth. (**b**) Confocal focus shift ΔF_z (black crosses) and shift in time-of-flight ΔTOF (grey circles) between the peak positions of FB echoes versus aperture size (number of aperture elements). (**c**) Estimated $Ct.Th^{MF}$ (black crosses) and $Ct.\nu_{11}^{MF}$ (grey circles) compared to the reference values $Ct.Th^{Ref}$ (dashed black line) and $Ct.\nu_{11}^{Ref}$ (dashed grey line) with respect to number of aperture elements.

The peak of the frontside echo occurred for all models at a focal depth of 15 mm. In contrast, the peak position varied for each aperture size and increased from 23.7 mm for the 32-element aperture to 24.9 mm for the 72-element aperture (Figure A1a). Moreover, the tracked front and backside (FB) amplitudes increased with an increasing aperture element number because more receiving signals were captured for delay and sum beamforming. For frontside and backside echoes, the tracked FB echo amplitudes showed a sharpening of the backside peaks with increasing aperture element number. Figure A1b shows an increase of the confocal focus shift ΔF_z with increasing aperture element number, but ΔTOF remained unchanged. The comparison of the estimated $Ct.Th^{MF}$ and $Ct.\nu_{11}^{MF}$ to the reference values in Figure A1c shows that the reference values were reached, both for $Ct.Th^{MF}$ and $Ct.\nu_{11}^{MF}$ for 64-, 68-, and 72-element apertures.

Table A1 summarizes the estimated ΔTOF between confocal FB reflection echoes, semi-aperture angle θ, the critical angle θ_{crit} defined by Snell's law, the effective aperture $k_{eff}\theta$, and $Ct.Th^{MF}$ and $Ct.\nu_{11}^{MF}$. For apertures larger than 44 elements, the difference of the semi-aperture angle to the critical angle $\Delta\theta = \theta_{crit} - \theta$ was smaller than 10° and the effective aperture was derived iteratively using [19]. For apertures less than or equal to 44-elements, no effective aperture was derived due to $\Delta\theta$ being larger than 10. In summary, the comparison of the bone plate model with different aperture element numbers revealed a dependence of the estimated $Ct.Th^{MF}$ and $Ct.\nu_{11}^{MF}$ on the semi-aperture angle. The previous study determined the effective aperture $k_{eff}\theta$ with $k_{eff} = 0.1 \cdot \Delta\theta$ for $\Delta\theta < 10°$ in five iteration steps (Equation (5) in [19]). Due to the larger element number and distance of the transducer to the bone surface compared with the previous study, an adapted factor of 0.122 was used instead 0.1 for k_{eff}. For $k_{eff} < 0.6$, the iteration resulted in incorrect $Ct.Th^{MF}$ and $Ct.\nu_{11}^{MF}$ values; therefore, the factor k_{eff} was not determined in five iterations as the iterative process was interrupted when k_{eff} reached values smaller than 0.6. For simulation models with 64-, 68-, and 72 elements the RE of $Ct.Th^{MF}$ and $Ct.\nu_{11}^{MF}$ was smaller than 0.5%. As simulation models with an aperture size greater than or equal to 64-elements showed no difference in $Ct.Th^{MF}$ and $Ct.\nu_{11}^{MF}$, all further simulations were performed with a 64-element aperture transducer.

Table A1. Results of $Ct.Th^{MF}$, $Ct.v_{11}^{MF}$ and relative errors (RE) for the bone plate models with different element apertures using shift in time-of-flight between confocal front-and back reflections ΔTOF, semi-aperture angle θ_{crit} for the effective aperture $k_{eff}\theta$.

Ap	ΔTOF [μs]	θ [°]	θ_{crit} [°]	$k_{eff}\theta$ [°]	$Ct.Th^{MF}$ [mm]	RE [%]	$Ct.v_{11}^{MF}$ [m/s]	RE [%]
32	2.287	11.75	26.95	11.75	3.79	5.27	3310	5.54
36	2.287	13.06	26.73	13.06	3.81	4.78	3335	4.83
40	2.287	13.77	26.69	13.77	3.82	4.39	3340	4.69
44	2.290	14.96	26.51	14.96	3.85	3.87	3360	4.12
48	2.286	16.19	26.51	26.51	3.85	3.87	3360	4.12
52	2.291	17.39	26.90	20.18	3.80	4.99	3315	5.40
56	2.290	18.50	26.30	17.61	3.88	2.96	3385	3.40
60	2.297	19.65	25.85	14.97	3.95	1.30	3440	1.83
64	2.292	20.77	25.38	12.46	4.00	0.01	3490	0.41
68	2.292	21.87	24.92	13.12	4.01	0.25	3500	0.21
72	2.296	23.03	25.45	13.82	4.00	0.01	3490	0.41

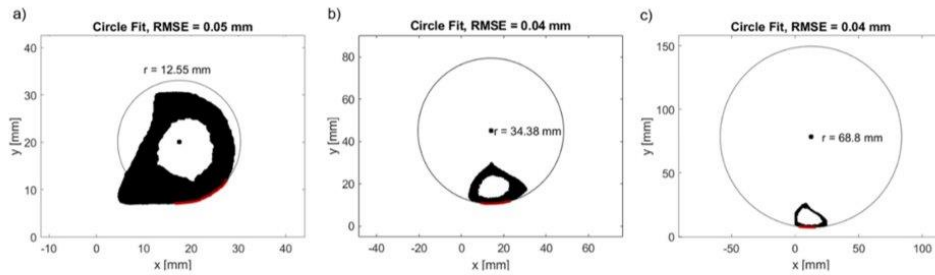## Appendix B. Estimation of Bone Curvature on HR-pQCT Bone Images

Figure A2. Three representative HR-pQCT scans of tibia midshaft bones of postmenopausal women. Circles were fitted to the anteromedial side to estimate the local bone surface radius. The red line indicates the central anteromedial tibia region, where ultrasound measurements were performed. The images in (**a**–**c**) show subjects with a minimum (12.6 mm), mean (34.38 mm), and maximum (68.8 mm) curvature radius, respectively.

Appendix C. Phase Aberration Correction (PAC) Methods

Appendix C.1. PAC I: Time-Shift Correction Based on Periosteal Bone Surface Geometry, Surface Time Correction (ST)

Figure A3a shows an ultrasound wave transmitted from the transducer element 1 to the backside bone surface position F. For the curved model, the waves travel along a longer path in water (red arrows in Figure A3a) compared with the flat bone model, resulting in a shift ΔTOF_{geo} caused by the different surface geometries. These were determined using the concept of refraction compensation proposed by Yasuda et al. [24].

For each transmit channel Tx_i and focus depth F below the frontside surface, the crossing point of the straight ultrasound wave path and the frontside surface was determined to calculate the height length of the flat plate $h_{1,plate}$ and curved plate $h_{1,curved}$, and the width length of the flat plate $w_{1,plate}$ and curved plate $w_{1,curved}$ between the crossing point and channel position (Figure A3a). In addition, the time-of-flight from the transmitted channel to the focus point F was calculated for the flat bone plate by

$$TOF_{Tx_i,plate} = \frac{\sqrt{w_{1,plate}^2 + h_{1,plate}^2}}{v_{H_2O}} + \frac{\sqrt{w_{1,plate}^2 + h_{1,plate}^2}}{Ct.v_{11}} \tag{5}$$

77

and for the curved bone plate using $w_{1,curved}$ and $w_{2,curved}$ instead of $w_{1,plate}$ and $w_{2,plate}$ (Figure A3a), respectively. The assumption of $Ct.v_{11}$ to calculate $TOF_{Txi,\,plate}$, was performed by implementing a loop for retrieving $Ct.Th^{MF}$ and $Ct.v_{11}{}^{MF}$. The starting value of $Ct.v_{11,assump}$ was defined at 2500 m/s based on the previous study [19], where $Ct.v_{11}$ values smaller than 2600 m/s were reported for cortical porosity values larger than 20%. If the difference between the calculated $Ct.v_{11}{}^{MF}$ and the assumed input $Ct.v_{11,assump}$ was larger than 10 m/s, the loop continued by replacing the new assumed $Ct.v_{11,assump}$ with the previously calculated $Ct.v_{11}{}^{MF}$. The loop stopped if the difference between calculated $Ct.v_{11}{}^{MF}$ and assumed $Ct.v_{11,assump}$ was smaller than 10 m/s. The total time-of-flight from one transmit channel to the receiving channel Rx_i for the plate and curved models was calculated by

$$TOF_{Rx_i,plate} \; = \; TOF_{Tx_i,plate} \; + \; TOF_{64 \,-\, Tx_{i \,+\, 1},plate}, \tag{6}$$

under the assumption of a straight ultrasound transmitted and reflected travel paths, from transmit channel Tx_i to the focus position F, and back to the receiving channel $Rx_i = 64 - Tx_{i+1}$.

After calculating all TOF_{Rx} for all channels 1 to 64, the corrected delay is determined for each element by

$$TOF_{geo,Rx_i} \; = \; TOF_{Rx_i,curve} \; + \; TOF_{Rx_i,plate}. \tag{7}$$

In summary, *PAC I* corrects for the different propagation travel times caused by the bone curvature compared to a flat plate geometry at each receiving channel.

Appendix C.2. PAC II: Tilt Correction (ACF)

An autocorrelation function (ACF) analysis was used to correct for phase distortions caused by surfaces inclination. The ACF analysis was performed in the Fourier domain using the Wiener-Khinchine theorem implemented in the '*autocorr2d.m*' function [51]:

$$|V_{ACF}| \; = \; \left| F_d^{-1}\Big(F_d(V_{gb})conj\big(F_d(V_{gb})\big)\Big)\right|, \tag{8}$$

where V_{ACF} is the ACF signal, $|V_{ACF}|$ the magnitude of V_{ACF}, and $F_d()$ and $F_d^{-1}()$ are the discrete Fourier and inverse Fourier transforms, respectively, of the gated backside signals V_{gb} using Hanning-window. For each receiving channel, the backside echoes were gated after adding the beamforming delay shift, PAC I correction, and before summation (Figure A3b). From all received backside signals, the maximum signal from all received signals was used to define a threshold value for ACF correction. The threshold was defined at 40% of the maximum signal. All backside signals above the threshold were used to fit an ellipsoid on $|V_{ACF}|$ using the '*regionprops.m*' function of the Matlab Image Processing Toolbox (Figure A3c). The inclination angle of the ellipsoid to the major semi-axis α_{ACF} (Figure A3c) was used to apply a linear time shift correction Δt_{ACF} to remove the tilt such that Δt_{ACF} at the channel with the highest backside amplitude was zero. The proper correction of the wavefront tilt was verified by repeating the ACF analysis after PAC II correction (Figure A3d).

Appendix C.3. PAC III: Cross-Correlation (CC)

The cross-correlation method was used to correct for small fluctuations in travel times caused by intracortical pores to determine $F_{z,B}$ after ACF correction. The shift in the time-of-flight of the backside signals $\Delta TOF_{B,Rxi}$ from each receiving channel were estimated with respect to the time-of-flight of the reference channel Rx_{Ref}. For a focus depth smaller than the depth of the backside surface, backside echoes were not in phase. The $\Delta TOF_{B,Rxi}$ showed a concave shape with negative curvature (Figure A3e for focal depth of 23 mm and 24 mm). When focus positions converged towards confocal backside focus position $F_{z,B}$, the negative curvature of the concave shape of $\Delta TOF_{B,Rxi}$ decreased. At $F_{z,B}$ the backside

signals were in phase by means of $\Delta TOF_{B,Rxi} = 0$. For a focus depth larger than $F_{z,B}$, the reflected backside signals were defocused and $\Delta TOF_{B,Rxi}$ transitioned to a convex shape with increasing positive curvature towards larger focus depths (Figure A3e for focal depths of 25 mm and 26 mm).

On the retrieved $\Delta TOF_{B,Rxi}$ a second order fit was performed to estimate the curvature parameter p_1 (Figure A3f) using the following equation.

$$\Delta TOF_{B, Rx_i} = p_1 \cdot \left(R_{x_i} - R_{x_{ref}} \right)^2 + p_2. \tag{9}$$

The parameter p_2 represents the value of $\Delta TOF_{B,Rxref}$ at the reference channel, which was not used for further analysis. The parameter p_1 represents the curvature of the second order fit. The change of the curvature of $\Delta TOF_{BS,Rxi}$ from negative values for focus depth smaller than the confocal focus depth towards positive values for focus depth larger than the confocal focus depth, showed a linear dependence of p_1 over the focus depth. The focus position where p_1 remained zero was defined as $F_{z,B}$ position. It was determined by a linear fit, $p_1 = m \cdot F_z + n$, from ± 2 focus position around the focus depth, where p_1 had the smallest distance to zero (Figure A3e). Instead of using the amplitude of $H_B(F_z)$ for focus shift ΔF_z between confocal frontside and backside bone reflections, the zero-crossing value of p_1 (Figure A3f) was used for $F_{z,B}$ to estimate ΔF_z for $Ct.Th$ and $Ct.v_{11}$ calculation.
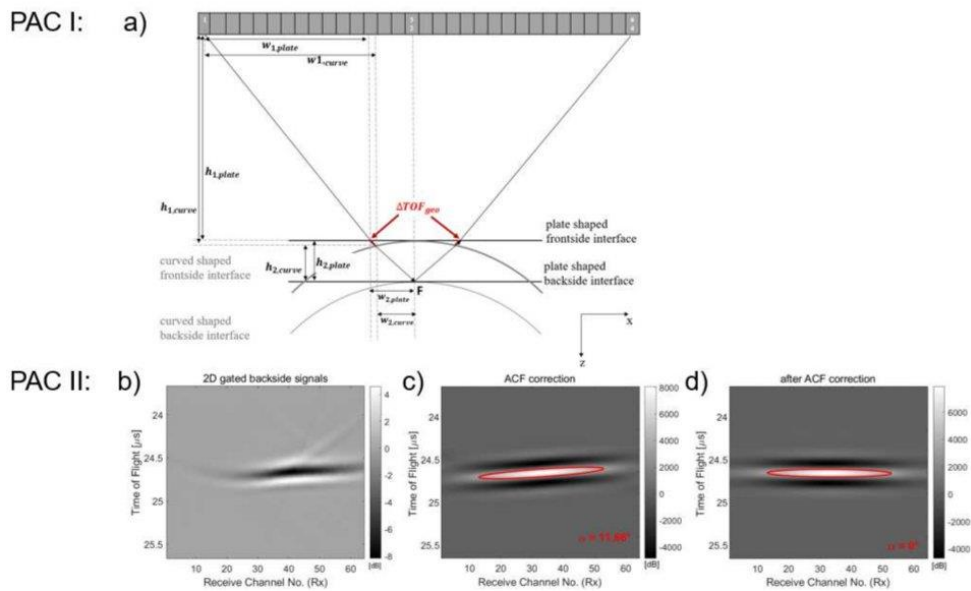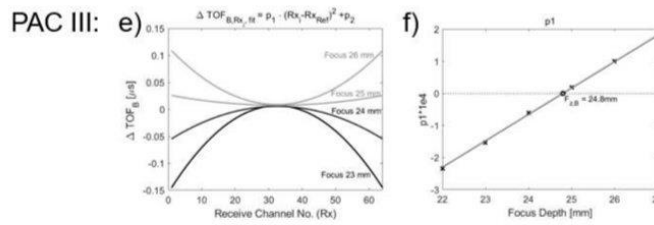

Figure A3. *Cont.*

Figure A3. PAC I: (**a**) Schematic illustration of the additional shift ΔTOF_{geo} (red line) of a wave traveling from element 1 to focus *F* and back to element 64 for a curved shaped bone surface compared with a flat bone plate. Note, that a focused beam of 64 elements was used and only the propagation path of the ultrasound wave of one receiving channel is shown. PAC II: Details of 2D ACF analysis for model *r40dx3.11*. (**b**) Two-dimensional image of the gated backside signals at confocal depth (25 mm) after PAC I. (**c**) Two-dimensional magnitude of ACF backside signal. The fitted ellipsoid is shown in red. (**d**) Two-dimensional magnitude of ACF backside signal after the ACF correction. PAC III: Schematic illustration to estimate $\Delta F_{z,B}$ using cross-correlation for the *flat plate* model. (**e**) Second order fit from ΔTOF_B of the backside signals using cross-correlation. (**f**) Curvature parameter of the second order fit p_1 (black crosses) over the focus depth and the linear fit (grey line) to estimate the zero-crossing point (black circle) for the estimation of $\Delta F_{z,B}$.

Appendix D. Results

Table A2. Summary of simulation models. '*r*' and '*dx*' in the model abbreviations represent the curvature radius of the bone model and the lateral shift of the transmit and receive arrays relative to the beam axis, respectively. '*Po*' represents the porosity value when pores were simulated.

Effect of.	Model Abbreviation	Curvature Radius r (mm)	Lateral Shift to Beam Axis dx (mm)	Bone Surface Tilt (°)	Porosity [%]
	flat plate	10,000	0	0	0
curvature	*r60dx0*	60	0	0	0
	r50dx0	50	0	0	0
	r40dx0	40	0	0	0
	r30dx0	30	0	0	0
	r20dx0	20	0	0	0
curvature and tilt	*r40dx1.11*	40	1.11	1.4	0
	r40dx2.11	40	2.11	3.1	0
	r40dx3.11	40	3.11	4.5	0
	r40dx4.11	40	4.11	5.9	0
	r40dx5.11	40	5.11	7.4	0
	r40dx6.11	40	6.11	8.9	0
curvature and porosity	*r40dx0Po2*	40	0	0	2
	r40dx0Po4	40	0	0	4
	r40dx0Po6	40	0	0	6
	r40dx0Po8	40	0	0	8
	r40dx0Po10	40	0	0	10
	r40dx0Po12	40	0	0	12
	r40dx0Po14	40	0	0	14
	r40dx0Po16	40	0	0	16
	r40dx0Po18	40	0	0	18
	r40dx0Po20	40	0	0	20

Table A3. Results of $Ct.Th^{Ref}$ and $Ct.v_{11}^{Ref}$ of transmission simulation.

Model	$Ct.v_{11}^{Ref}$ [m/s]
r40dx0Po2	3428.6
r40dx0Po4	3321.8
r40dx0Po6	3189.4
r40dx0Po8	3127.0
r40dx0Po10	3038.0
r40dx0Po12	2953.8
r40dx0Po14	2848.7
r40dx0Po16	2774.6
r40dx0Po18	2704.2
r40dx0Po20	2681.6

Table A4. Results of $Ct.Th^{MF}$, $Ct.v_{11}^{MF}$ and relative errors (RE) for each PAC method.

Model	Correction	$Ct.Th^{MF}$ [mm]	$RE_{Ct.Th}$ [%]	$Ct.v_{11}^{MF}$ [m/s]	$RE_{Ct.v11}$ [%]
flat plate	No	4.00	0.01	3490	0.41
(reference)	ST	4.00	0.01	3490	0.41
	ST + ACF	4.00	0.01	3490	0.41
	ST + ACF + CC	4.00	0.01	3490	0.41
r60dx0	No	3.77	5.77	3330	5.83
	ST	3.99	0.32	3470	0.98
	ST + ACF	3.99	0.32	3470	0.98
	ST + ACF + CC	4.00	0.01	3490	0.41
r50dx0	No	3.72	6.91	3255	7.11
	ST	3.98	0.48	3475	0.83
	ST + ACF	3.98	0.48	3475	0.83
	ST + ACF + CC	4.00	0.01	3495	0.26
r40dx0	No	3.65	8.70	3180	9.25
	ST	3.96	1.07	3460	1.26
	ST + ACF	3.96	1.07	3460	1.26
	ST + ACF + CC	4.02	0.51	3510	0.16
r30dx0	No	3.57	10.80	3120	10.97
	ST	3.94	1.49	3440	1.83
	ST + ACF	3.93	1.65	3445	1.69
	ST + ACF + CC	4.06	1.48	3545	1.16
r20dx0	No	3.37	15.66	2955	15.67
	ST	3.82	4.49	3340	4.69
	ST + ACF	3.85	3.78	3360	4.12
	ST + ACF + CC	3.85	3.78	3360	4.12
r40dx1.11	No	3.67	8.26	3210	8.40
	ST	3.96	0.91	3455	1.41
	ST + ACF	3.96	1.07	3460	1.26
	ST + ACF + CC	4.03	0.67	3505	0.02
r40dx2.11	No	3.69	7.66	3235	7.68
	ST	3.93	1.65	3445	1.69
	ST + ACF	3.96	0.91	3455	1.41
	ST + ACF + CC	3.96	0.91	3455	1.41
r40dx3.11	No	3.67	7.50	3205	7.83
	ST	3.79	5.23	3325	5.12
	ST + ACF	3.95	1.19	3465	1.12
	ST + ACF + CC	3.95	1.19	3465	1.12
r40dx4.11	No	3.64	8.99	3175	9.40
	ST	3.58	10.45	3140	10.39
	ST + ACF	3.93	1.86	3445	1.69
	ST + ACF + CC	3.93	1.86	3445	1.69

81

Table A4. *Cont.*

| Model	Correction	$Ct.Th^{MF}$ [mm]	$RE_{Ct.Th}$ [%]	$Ct.v_{11}^{MF}$ [m/s]	$RE_{Ct.v11}$ [%]
r40dx5.11	No	3.61	9.84	3150	10.11
	ST	3.47	13.28	3040	13.25
	ST + ACF	3.80	4.91	3335	4.83
	ST + ACF + CC	3.80	4.91	3335	4.83
r40dx6.11	No	3.47	13.37	3030	13.53
	ST	3.29	17.74	2895	17.39
	ST + ACF	3.54	11.48	3110	11.25
	ST + ACF + CC	3.54	11.48	3110	11.25
r40dx0Po2	No	3.60	10.02	3065	10.60
	ST	3.88	3.08	3310	3.46
	ST + ACF	3.90	2.45	3330	2.88
	ST + ACF + CC	3.93	1.83	3350	2.29
r40dx0Po4	No	4.39	9.67	3640	9.58
	ST	3.82	4.57	3165	4.72
	ST + ACF	3.81	4.47	3170	4.57
	ST + ACF + CC	3.76	6.08	3135	5.62
r40dx0Po6	No	3.57	10.79	2830	11.27
	ST	3.85	3.79	3050	4.37
	ST + ACF	3.85	3.87	3055	4.21
	ST + ACF + CC	3.92	1.92	3120	2.18
r40dx0Po8	No	3.54	11.49	2805	10.30
	ST	3.79	5.27	3015	3.58
	ST + ACF	3.83	4.18	3010	3.74
	ST + ACF + CC	3.89	2.87	3055	2.30
r40dx0Po10	No	5.16	29.12	3950	30.02
	ST	3.98	0.48	3030	0.26
	ST + ACF	3.95	1.24	3015	0.76
	ST + ACF + CC	3.98	0.48	3030	0.26
r40dx0Po12	No	5.58	39.69	4090	38.47
	ST	3.86	3.46	2835	4.02
	ST + ACF	3.87	3.23	2830	4.19
	ST + ACF + CC	3.92	1.94	2870	2.84
r40dx0Po14	No	4.78	19.54	3440	20.76
	ST	3.78	5.40	2760	3.11
	ST + ACF	3.78	5.40	2760	3.11
	ST + ACF + CC	3.78	5.40	2760	3.11
r40dx0Po16	No	4.82	20.55	3870	39.48
	ST	3.79	5.36	2635	5.03
	ST + ACF	3.79	5.14	2630	5.21
	ST + ACF + CC	3.90	2.58	2695	2.87
r40dx0Po18	No	3.82	4.52	2585	4.41
	ST	3.98	0.56	2680	0.89
	ST + ACF	3.97	0.79	2685	0.71
	ST + ACF + CC	3.83	4.21	2640	2.37
r40dx0Po20	No	5.65	41.24	3750	39.84
	ST	2.22	44.45	2675	0.25
	ST + ACF	3.33	16.66	2730	1.80
	ST + ACF + CC	3.03	24.14	2670	0.43

82
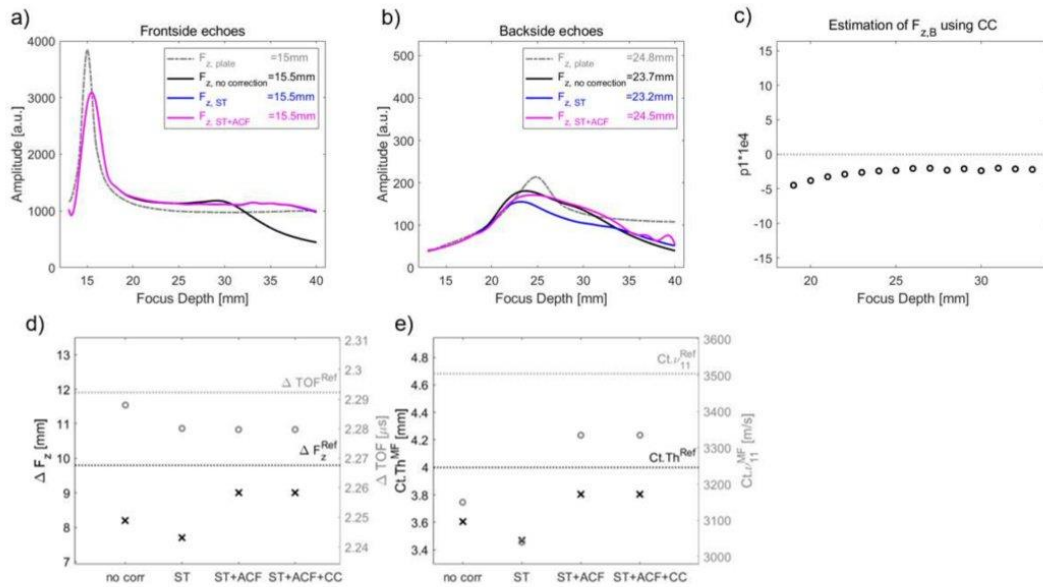
Figure A4. Model *r40dx5.11*: (**a**) Comparison of tracked amplitude at each correction step for frontside amplitudes (tracked amplitude after ST, ST + ACF and ST + ACF + CC correction overlap). The reference-tracked amplitude of the plate model was shown by the grey dashed line (**b**) and backside amplitudes (tracked amplitude after ST and ST + ACF correction overlap), respectively. (**c**) Curvature parameter p_1, retrieved from second order fit of using CC, as a function of focal depth (black circles). Linear fit (red line) was used to retrieve $F_{z,B}$ at zero-crossing point. (**d**) Comparison of focus shift ΔF_z and shift (black crosses) in time-of-flight ΔTOF (grey circles) to the reference $\Delta F_z{}^{Ref}$ (dashed black line) and ΔTOF^{Ref} (dashed grey line) of the plate model. (**e**) Estimated $Ct.Th^{MF}$ and $Ct.v_{11}{}^{MF}$ after each correction step compared to the reference $Ct.Th^{Ref}$ (dashed black line) and $Ct.v_{11}{}^{Ref}$ (dashed grey line) value.
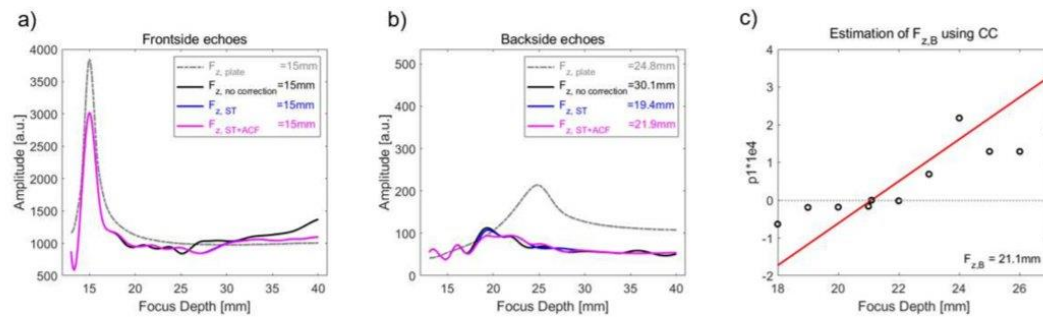

Figure A5. *Cont.*
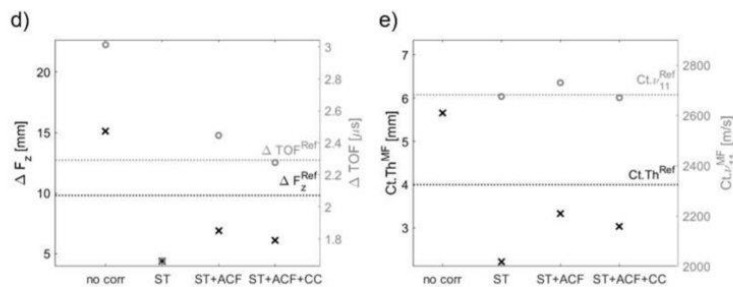
Figure A5. Model *r40dx0Po20*: (**a**) Comparison of tracked amplitude at each correction step for frontside amplitudes (tracked amplitude after ST, ST + ACF and ST + ACF + CC correction overlap). The reference-tracked amplitude of the plate model was shown by the grey dashed line (**b**) and backside amplitudes (tracked amplitude after ST and ST + ACF correction overlap), respectively. (**c**) Curvature parameter p_1, retrieved from second order fit of using CC, as a function of focal depth (black circles). Linear fit (red line) was used to retrieve $F_{z,B}$ at zero-crossing point. (**d**) Comparison of focus shift ΔF_z and shift (black crosses) in time-of-flight ΔTOF (grey circles) to the reference ΔF_z^{Ref} (dashed black line) and ΔTOF^{Ref} (dashed grey line) of the plate model. (**e**) Estimated $Ct.Th^{MF}$ and $Ct.v_{11}^{MF}$ after each correction step compared to the reference $Ct.Th^{Ref}$ (dashed black line) and $Ct.v_{11}^{Ref}$ (dashed grey line) value.

References

1. Miller, P.D.; Siris, E.S.; Barrett-Connor, E.; Faulkner, K.G.; Wehren, L.E.; Abbott, T.A.; Chen, Y.T.; Berger, M.L.; Santora, A.C.; Sherwood, L.M. Prediction of fracture risk in postmenopausal white women with peripheral bone densitometry: Evidence from the National Osteoporosis Risk Assessment. *J. Bone Miner. Res.* **2002**, *17*, 2222–2230. [CrossRef] [PubMed]
2. Njeh, C.F.; Hans, D.; Li, J.; Fan, B.; Fuerst, T.; He, Y.Q.; Tsuda-Futami, E.; Lu, Y.; Wu, C.Y.; Genant, H.K. Comparison of six calcaneal quantitative ultrasound devices: Precision and hip fracture discrimination. *Osteoporos. Int.* **2000**, *11*, 1051–1062. [CrossRef] [PubMed]
3. Lasaygues, P.; Ouedraogo, E.; Lefebvre, J.P.; Gindre, M.; Talmant, M.; Laugier, P. Progress towards in vitro quantitative imaging of human femur using compound quantitative ultrasonic tomography. *Phys. Med. Biol.* **2005**, *50*, 2633–2649. [CrossRef] [PubMed]
4. Lasaygues, P. Assessing the cortical thickness of long bone shafts in children, using two-dimensional ultrasonic diffraction tomography. *Ultrasound Med. Biol.* **2006**, *32*, 1215–1227. [CrossRef] [PubMed]
5. Bernard, S.; Monteiller, V.; Komatitsch, D.; Lasaygues, P. Ultrasonic computed tomography based on full-waveform inversion for bone quantitative imaging. *Phys. Med. Biol.* **2017**, *62*, 7011–7035. [CrossRef]
6. Li, H.; Le, L.H.; Sacchi, M.D.; Lou, E.H. Ultrasound imaging of long bone fractures and healing with the split-step fourier imaging method. *Ultrasound Med. Biol.* **2013**, *39*, 1482–1490. [CrossRef]
7. Zheng, R.; Le, L.H.; Sacchi, M.D.; Lou, E. Imaging Internal Structure of Long Bones Using Wave Scattering Theory. *Ultrasound Med. Biol.* **2015**, *41*, 2955–2965. [CrossRef]
8. Schneider, J.; Ramiandrisoa, D.; Armbrecht, G.; Ritter, Z.; Felsenberg, D.; Raum, K.; Minonzio, J.G. In Vivo Measurements of Cortical Thickness and Porosity at the Proximal Third of the Tibia Using Guided Waves: Comparison with Site-Matched Peripheral Quantitative Computed Tomography and Distal High-Resolution Peripheral Quantitative Computed Tomography. *Ultrasound Med. Biol.* **2019**, *45*, 1234–1242. [CrossRef]
9. Giangregorio, L.M.; Webber, C.E. Speed of sound in bone at the tibia: Is it related to lower limb bone mineral density in spinal-cord-injured individuals? *Spinal Cord* **2004**, *42*, 141–145. [CrossRef]
10. Moilanen, P.; Maatta, M.; Kilappa, V.; Xu, L.; Nicholson, P.H.; Alen, M.; Timonen, J.; Jamsa, T.; Cheng, S. Discrimination of fractures by low-frequency axial transmission ultrasound in postmenopausal females. *Osteoporos. Int.* **2013**, *24*, 723–730. [CrossRef]
11. Karjalainen, J.P.; Riekkinen, O.; Toyras, J.; Hakulinen, M.; Kroger, H.; Rikkonen, T.; Salovaara, K.; Jurvelin, J.S. Multi-site bone ultrasound measurements in elderly women with and without previous hip fractures. *Osteoporos. Int.* **2012**, *23*, 1287–1295. [CrossRef] [PubMed]
12. Vallet, Q.; Bochud, N.; Chappard, C.; Laugier, P.; Minonzio, J.G. In Vivo Characterization of Cortical Bone Using Guided Waves Measured by Axial Transmission. *IEEE Trans. Ultrason. Ferroelectr. Freq. Control* **2016**, *63*, 1361–1371. [CrossRef] [PubMed]
13. Casciaro, S.; Peccarisi, M.; Pisani, P.; Franchini, R.; Greco, A.; De Marco, T.; Grimaldi, A.; Quarta, L.; Quarta, E.; Muratore, M.; et al. An Advanced Quantitative Echosound Methodology for Femoral Neck Densitometry. *Ultrasound Med. Biol.* **2016**, *42*, 1337–1356. [CrossRef] [PubMed]
14. Renaud, G.; Kruizinga, P.; Cassereau, D.; Laugier, P. In vivo ultrasound imaging of the bone cortex. *Phys. Med. Biol.* **2018**, *63*, 125010. [CrossRef] [PubMed]

15. Armbrecht, G.; Nguyen Minh, H.; Massmann, J.; Raum, K. Pore-Size Distribution and Frequency-Dependent Attenuation in Human Cortical Tibia Bone Discriminate Fragility Fractures in Postmenopausal Women With Low Bone Mineral Density. *JBMR Plus* **2021**, *5*, e10536. [CrossRef]
16. Goss, S.A.; Johnston, R.L.; Dunn, F. Comprehensive compilation of empirical ultrasonic properties of mammalian tissues. *J. Acoust. Soc. Am.* **1978**, *64*, 423–457. [CrossRef]
17. Granke, M.; Grimal, Q.; Saied, A.; Nauleau, P.; Peyrin, F.; Laugier, P. Change in porosity is the major determinant of the variation of cortical bone elasticity at the millimeter scale in aged women. *Bone* **2011**, *49*, 1020–1026. [CrossRef]
18. Di Paola, M.; Gatti, D.; Viapiana, O.; Cianferotti, L.; Cavalli, L.; Caffarelli, C.; Conversano, F.; Quarta, E.; Pisani, P.; Girasole, G.; et al. Radiofrequency echographic multispectrometry compared with dual X-ray absorptiometry for osteoporosis diagnosis on lumbar spine and femoral neck. *Osteoporos. Int.* **2019**, *30*, 391–402. [CrossRef]
19. Nguyen Minh, H.; Du, J.; Raum, K. Estimation of Thickness and Speed of Sound in Cortical Bone Using Multifocus Pulse-Echo Ultrasound. *IEEE Trans. Ultrason. Ferroelectr. Freq. Control* **2020**, *67*, 568–579. [CrossRef]
20. Iori, G.; Schneider, J.; Reisinger, A.; Heyer, F.; Peralta, L.; Wyers, C.; Gluer, C.C.; van den Bergh, J.P.; Pahr, D.; Raum, K. Cortical thinning and accumulation of large cortical pores in the tibia reflect local structural deterioration of the femoral neck. *Bone* **2020**, *137*, 115446. [CrossRef]
21. Bjornerem, A.; Bui, Q.M.; Ghasem-Zadeh, A.; Hopper, J.L.; Zebaze, R.; Seeman, E. Fracture risk and height: An association partly accounted for by cortical porosity of relatively thinner cortices. *J. Bone Miner. Res.* **2013**, *28*, 2017–2026. [CrossRef] [PubMed]
22. Greenfield, M.A.; Craven, J.D.; Wishko, D.S.; Huddleston, A.L.; Friedman, R.; Stern, R. The modulus of elasticity of human cortical bone: An in vivo measurement and its clinical implications. *Radiology* **1975**, *115*, 163–166. [CrossRef] [PubMed]
23. Stegman, M.R.; Heaney, R.P.; Traversgustafson, D.; Leist, J. Cortical Ultrasound Velocity as an Indicator of Bone Status. *Osteoporos. Int.* **1995**, *5*, 349–353. [CrossRef] [PubMed]
24. Yasuda, J.; Yoshikawa, H.; Tanaka, H. Phase aberration correction for focused ultrasound transmission by refraction compensation. *Jpn. J. Appl. Phys.* **2019**, *58*, SGGE22. [CrossRef]
25. Bossy, E.; Talmant, M.; Laugier, P. Three-dimensional simulations of ultrasonic axial transmission velocity measurement on cortical bone models. *J. Acoust. Soc. Am.* **2004**, *115*, 2314–2324. [CrossRef]
26. Sasso, M.; Haiat, G.; Yamato, Y.; Naili, S.; Matsukawa, M. Frequency dependence of ultrasonic attenuation in bovine cortical bone: An in vitro study. *Ultrasound Med. Biol.* **2007**, *33*, 1933–1942. [CrossRef]
27. Rohrbach, D.; Lakshmanan, S.; Peyrin, F.; Langer, M.; Gerisch, A.; Grimal, Q.; Laugier, P.; Raum, K. Spatial distribution of tissue level properties in a human femoral cortical bone. *J. Biomech.* **2012**, *45*, 2264–2270. [CrossRef]
28. Iori, G.; Schneider, J.; Reisinger, A.; Heyer, F.; Peralta, L.; Wyers, C.; Grasel, M.; Barkmann, R.; Gluer, C.C.; van den Bergh, J.P.; et al. Large cortical bone pores in the tibia are associated with proximal femur strength. *PLoS ONE* **2019**, *14*, e0215405. [CrossRef]
29. Chappard, C.; Bensalah, S.; Olivier, C.; Gouttenoire, P.J.; Marchadier, A.; Benhamou, C.; Peyrin, F. 3D characterization of pores in the cortical bone of human femur in the elderly at different locations as determined by synchrotron micro-computed tomography images. *Osteoporos. Int.* **2013**, *24*, 1023–1033. [CrossRef]
30. Bakalova, L.P.; Andreasen, C.M.; Thomsen, J.S.; Bruel, A.; Hauge, E.M.; Kiil, B.J.; Delaisse, J.M.; Andersen, T.L.; Kersh, M.E. Intracortical Bone Mechanics Are Related to Pore Morphology and Remodeling in Human Bone. *J. Bone Miner. Res.* **2018**, *33*, 2177–2185. [CrossRef]
31. Haïat, G. Linear Ultrasonic Properties of Cortical Bone: In Vitro Studies. In *Bone Quantitative Ultrasound*; Laugier, P., Haïat, G., Eds.; Springer: Dordrecht, The Netherlands, 2011; pp. 331–360.
32. Iori, G.; Heyer, F.; Kilappa, V.; Wyers, C.; Varga, P.; Schneider, J.; Grasel, M.; Wendlandt, R.; Barkmann, R.; van den Bergh, J.P.; et al. BMD-based assessment of local porosity in human femoral cortical bone. *Bone* **2018**, *114*, 50–61. [CrossRef] [PubMed]
33. Burghardt, A.J.; Buie, H.R.; Laib, A.; Majumdar, S.; Boyd, S.K. Reproducibility of direct quantitative measures of cortical bone microarchitecture of the distal radius and tibia by HR-pQCT. *Bone* **2010**, *47*, 519–528. [CrossRef] [PubMed]
34. Hudimac, A.A. Ray Theory Solution for the Sound Intensity in Water Due to a Point Source above It. *J. Acoust. Soc. Am.* **1957**, *29*, 916–917. [CrossRef]
35. Bala, Y.; Zebaze, R.; Seeman, E. Role of cortical bone in bone fragility. *Curr. Opin. Rheumatol.* **2015**, *27*, 406–413. [CrossRef]
36. Chevalley, T.; Bonjour, J.P.; van Rietbergen, B.; Ferrari, S.; Rizzoli, R. Fracture history of healthy premenopausal women is associated with a reduction of cortical microstructural components at the distal radius. *Bone* **2013**, *55*, 377–383. [CrossRef]
37. Yang, L.; Udall, W.J.M.; McCloskey, E.V.; Eastell, R. Distribution of bone density and cortical thickness in the proximal femur and their association with hip fracture in postmenopausal women: A quantitative computed tomography study. *Osteoporos. Int.* **2014**, *25*, 251–263. [CrossRef]
38. Mikolajewicz, N.; Bishop, N.; Burghardt, A.J.; Folkestad, L.; Hall, A.; Kozloff, K.M.; Lukey, P.T.; Molloy-Bland, M.; Morin, S.N.; Offiah, A.C.; et al. HR-pQCT Measures of Bone Microarchitecture Predict Fracture: Systematic Review and Meta-Analysis. *J. Bone Miner. Res.* **2020**, *35*, 446–459. [CrossRef]
39. Wydra, A.; Malyarenko, E.; Shapoori, K.; Maev, R.G. Development of a practical ultrasonic approach for simultaneous measurement of the thickness and the sound speed in human skull bones: A laboratory phantom study. *Phys. Med. Biol.* **2013**, *58*, 1083–1102. [CrossRef]
40. Njeh, C.F.; Saeed, I.; Grigorian, M.; Kendler, D.L.; Fan, B.; Shepherd, J.; McClung, M.; Drake, W.M.; Genant, H.K. Assessment of bone status using speed of sound at multiple anatomical sites. *Ultrasound Med. Biol.* **2001**, *27*, 1337–1345. [CrossRef]

41. Talmant, M.; Kolta, S.; Roux, C.; Haguenauer, D.; Vedel, I.; Cassou, B.; Bossy, E.; Laugier, P. In vivo performance evaluation of bi-directional ultrasonic axial transmission for cortical bone assessment. *Ultrasound Med. Biol.* **2009**, *35*, 912–919. [CrossRef]
42. Olszynski, W.P.; Brown, J.P.; Adachi, J.D.; Hanley, D.A.; Ioannidis, G.; Davison, K.S.; CaMos Research, G. Multisite quantitative ultrasound for the prediction of fractures over 5 years of follow-up: The Canadian Multicentre Osteoporosis Study. *J. Bone Miner. Res.* **2013**, *28*, 2027–2034. [CrossRef] [PubMed]
43. Minonzio, J.G.; Bochud, N.; Vallet, Q.; Ramiandrisoa, D.; Etcheto, A.; Briot, K.; Kolta, S.; Roux, C.; Laugier, P. Ultrasound-Based Estimates of Cortical Bone Thickness and Porosity Are Associated With Nontraumatic Fractures in Postmenopausal Women: A Pilot Study. *J. Bone Miner. Res.* **2019**, *34*, 1585–1596. [CrossRef] [PubMed]
44. Behrens, M.; Felser, S.; Mau-Moeller, A.; Weippert, M.; Pollex, J.; Skripitz, R.; Herlyn, P.K.; Fischer, D.C.; Bruhn, S.; Schober, H.C.; et al. The Bindex((R)) ultrasound device: Reliability of cortical bone thickness measures and their relationship to regional bone mineral density. *Physiol. Meas.* **2016**, *37*, 1528–1540. [CrossRef] [PubMed]
45. Karjalainen, J.; Riekkinen, O.; Toyras, J.; Kroger, H.; Jurvelin, J. Ultrasonic assessment of cortical bone thickness in vitro and in vivo. *IEEE Trans. Ultrason. Ferroelectr. Freq. Control* **2008**, *55*, 2191–2197. [CrossRef] [PubMed]
46. Iori, G.; Du, J.; Hackenbeck, J.; Kilappa, V.; Raum, K. Estimation of Cortical Bone Microstructure From Ultrasound Backscatter. *IEEE Trans. Ultrason. Ferroelectr. Freq. Control* **2021**, *68*, 1081–1095. [CrossRef] [PubMed]
47. Anderson, M.E.; McKeag, M.S.; Trahey, G.E. The impact of sound speed errors on medical ultrasound imaging. *J. Acoust. Soc. Am.* **2000**, *107*, 3540–3548. [CrossRef]
48. Hasegawa, H.; Nagaoka, R. Initial phantom study on estimation of speed of sound in medium using coherence among received echo signals. *J. Med. Ultrason.* **2019**, *46*, 297–307. [CrossRef]
49. Lee, J.; Yoo, Y.; Yoon, C.; Song, T.K. A Computationally Efficient Mean Sound Speed Estimation Method Based on an Evaluation of Focusing Quality for Medical Ultrasound Imaging. *Electronics* **2019**, *8*, 1368. [CrossRef]
50. Renaud, G.; Clouzet, P.; Cassereau, D.; Talmant, M. Measuring anisotropy of elastic wave velocity with ultrasound imaging and an autofocus method: Application to cortical bone. *Phys. Med. Biol.* **2020**, *65*, 235016. [CrossRef]
51. Ursell, T. autocorr2d.m, MATLAB Central File Exchange. Available online: https://www.mathworks.com/matlabcentral/fileexchange/67348-autocorr2d (accessed on 3 December 2020).

Study C: Armbrecht G, Nguyen Minh H, Massmann J, Raum K. Pore-Size Distribution and Frequency-Dependent Attenuation in Human Cortical Tibia Bone Discriminate Fragility Fractures in Postmenopausal Women With Low Bone Mineral Density. JBMR Plus. 2021. Impact Factor: 6.284

CLINICAL TRIAL

Pore-Size Distribution and Frequency-Dependent Attenuation in Human Cortical Tibia Bone Discriminate Fragility Fractures in Postmenopausal Women With Low Bone Mineral Density

Gabriele Armbrecht,[1] ⓘ Huong Nguyen Minh,[2] ⓘ Jonas Massmann,[2] ⓘ and Kay Raum[2] ⓘ

[1]Charité—Universitätsmedizin Berlin, Corporate Member of Freie Universität Berlin, Humboldt-Universität zu Berlin, and Berlin Institute of Health, Department of Radiology, Center for Muscle and Bone Research, Berlin, Germany
[2]Charité—Universitätsmedizin Berlin, Corporate Member of Freie Universität Berlin, Humboldt-Universität zu Berlin, and Berlin Institute of Health, Center for Regenerative Therapies, Berlin, Germany

ABSTRACT

Osteoporosis is a disorder of bone remodeling leading to reduced bone mass, structural deterioration, and increased bone fragility. The established diagnosis is based on the measurement of areal bone mineral density by dual-energy X-ray absorptiometry (DXA), which poorly captures individual bone loss and structural decay. Enlarged cortical pores in the tibia have been proposed to indicate structural deterioration and reduced bone strength in the hip. Here, we report for the first time the in vivo assessment of the cortical pore-size distribution together with frequency-dependent attenuation at the anteromedial tibia midshaft by means of a novel ultrasonic cortical backscatter (CortBS) technology. We hypothesized that the CortBS parameters are associated with the occurrence of fragility fractures in postmenopausal women ($n = 55$). The discrimination performance was compared with those of DXA and high-resolution peripheral computed tomography (HR-pQCT). The results suggest a superior discrimination performance of CortBS (area under the receiver operating characteristic curve [AUC]: $0.69 \leq AUC \leq 0.75$) compared with DXA ($0.54 \leq AUC \leq 0.55$) and a similar performance compared with HR-pQCT ($0.66 \leq AUC \leq 0.73$). CortBS is the first quantitative bone imaging modality that can quantify microstructural tissue deteriorations in cortical bone, which occur during normal aging and the development of osteoporosis. © 2021 The Authors. *JBMR Plus* published by Wiley Periodicals LLC on behalf of American Society for Bone and Mineral Research.

KEY WORDS: CORTICAL BONE; FRACTURE DISCRIMINATION; CLINICAL TRIAL; DXA; QUANTITATIVE BONE ULTRASOUND

1. Introduction

Osteoporosis (OP) is an age-associated disorder of bone remodeling leading to reduced bone mass, structural deterioration, and increased bone fragility.[1] Although OP is generally thought of as a "woman's disease,"[2] men account for a third of OP-related hip fractures in Europe.[3] An estimated 1.0 million quality-adjusted life years (QALYs) were lost in 2017 due to fragility fractures. According to a recent systematic review of burden and management of fragility fractures in the largest EU countries,[4] fragility fractures are ranked number four among 16 common noncommunicable diseases with respect to the disability-adjusted life years (DALYs). For individuals aged >50 years, DALYs were higher than those for stroke. Established guidelines for the diagnosis of OP recommend the assessment of fracture risk factors and

the *T*-score, which is derived from the measurement of areal bone mineral density (aBMD) by means of dual-energy X-ray absorptiometry (DXA) at major fracture sites, ie, spine and proximal femur.[5] OP is defined for aBMD values 2.5 SD or more below the mean assessed in young adults (ie, *T*-score ≤ -2.5). Low bone mass (osteopenia, $-1 \geq$ *T*-score > -2.5) is currently not considered as a disease,[5] although a specific osteoprotective therapy is recommended if additional clinical risk factors are present.[6] However, bone strength is determined by a plethora of factors, including size, shape, architecture, and composition.[7] Today, there is increasing evidence that the majority of individuals who have sustained an osteoporosis-related fracture or who are at high risk of fracture are not diagnosed as osteoporotic according to the BMD level.[8,9]

Bone tissue undergoes permanent remodeling. Under normal conditions, osteoclasts create resorption canals in the cortical

bone tissue matrix, which are refilled by osteoblasts leaving a Haversian canal with a diameter of approximately 30 μm.[10] Bone loss occurs in both women and men as part of the natural aging process.[11] Unbalanced intracortical remodeling typically starts in the endosteal subcompartment and leaves partially refilled or even nonrefilled bone multicellular units (BMUs). Clustering of BMUs enhances their chances to merge, creating "giant" pores with diameters larger than 385 μm,[12] leading to the so-called trabecularized cortex[13] and ultimately to a thinning of the cortical bone shell. In the femoral neck of elderly people (aged 57 to 98 years), decreases of cortical thickness (Ct.Th) and increases of porosity (Ct.Po) by ~4% and ~32%, respectively, per decade have been observed.[14] In contrast, pore density (Ct.Po.Dn) was only reduced in the elderly (aged 87 to 98 years) compared with the middle-aged group (aged 57 to 68 years).[14] Postmenopausal women with osteopenia have higher cortical porosity and thinner cortices at the distal radius and tibia than women with normal aBMD.[15] In an ex vivo study, cortical thinning and the prevalence of large BMUs in the tibia were found to be associated with structural deterioration of the femoral neck[16] and proximal femur strength.[17] Although cortical porosity of the tibia was not associated with femoral stiffness or strength, the proportion of Ct.Po attributable to large pores (diameter >100 μm) was significantly associated with hip strength in both standing ($r = -0.61$) and falling ($r = 0.48$) conditions. However, cortical thinning is partially compensated by the apposition of new tissue matrix at the periosteal interface leading to an increased bone diameter and a further increase of the pore diameter gradient in the radial bone direction. The theory showing that bending strength is largely dictated by the size of the largest pores has been proposed by Griffith[18] and is nowadays well established in the field of fracture mechanics of cement-based materials.[19] Therefore, the cortical pore diameter distribution Ct.Po.Dm.D (hereinafter simply called pore-size distribution) represents a relevant target for identifying patients with high fracture risk. However, more than 60% of intracortical pores are smaller than 100 μm in diameter.[13] Given their small size, the in vivo imaging of cortical pores remains challenging, even with the most advanced high-resolution peripheral quantitative computed tomography (HR-pQCT). The imaging resolution of the first- and second-generation HR-pQCT systems with voxel sizes of 82 and 61 μm allows direct visualization and segmentation of large pores (ie, Ct.Po.Dm >100 μm) only, leaving the major fraction of smaller cortical pores unresolved. Iori and colleagues[20] have proposed a calibration rule for the estimation of Ct.Po locally from volumetric BMD (vBMD) distribution parameters. This method is more accurate (absolute error 3.4%) than established vBMD or threshold-based approaches, as it approximates the contribution of unresolved pores (ie, Ct.Po.Dm <80 μm). However, the HR-pQCT technology is not widely distributed and is used mostly in clinical research so far. With DXA-based aBMD, ie, the diagnostic gold standard, cortical bone loss resulting from structural decay is poorly captured.[9,21,22]

Quantitative ultrasound (QUS) methods are non-ionizing alternatives for the diagnosis of osteoporosis and the prediction of fracture risk.[23] Many QUS approaches target trabecular sites, eg, at the heel, and predicting BMD via empirical associations with the measured speed of sound (SOS), broadband ultrasound attenuation (BUA), and other parameters derived from the measurement.[24] More recent QUS technologies, eg, bidirectional axial transmission, measure cortical sites, eg, distal radius and tibia, and aim at the quantitative assessment of structural cortical

bone properties, eg, Ct.Th and Ct.Po.[25] However, none of the existing diagnostic technologies can assess quantitative information about the cortical pore micromorphology. Particularly, the transition from a normal age- and sex-specific pore-size distribution to a pathologically altered one caused by large BMUs could not be assessed in vivo so far.

We have recently developed a theoretical cortical bone backscatter model (CortBS) and an ultrasonic multi-angle 3D acquisition and data processing scheme to assess microstructural properties in cortical bone.[26] The method measures the frequency-dependent attenuation and backscatter coefficients $\alpha(f)$ and $BSC(f)$ at the tibia and retrieves the cortical pore-size distribution Ct.Po.Dm.D by fitting a theoretical backscatter coefficient to the measured $BSC(f)$. In an ex vivo study on bones from 19 human donors, pore-size parameters, particularly those describing the prevalence of large pores, could be assessed with high accuracy (adj. $R^2 = 0.55$). The combination of cortical thickness and CortBS parameters provided similar or better prediction accuracies of proximal femur stiffness and strength than aBMD.

In this cross-sectional pilot study, the CortBS method was applied for the first time in humans. Postmenopausal women with and without history of fragility fractures were included. We hypothesized that the frequency-dependent attenuation and microstructural CortBS parameters can be assessed in vivo and that they are associated with the occurrence of fragility fractures. The in vivo short-term precision of the CortBS parameters was assessed and the fracture discrimination performance was compared with those of DXA and HR-pQCT.

2. Materials and Methods

2.1 Research participants

For this cross-sectional study, 55 female subjects (aged ≥55 years) who have been referred to the Center for Muscle and Bone Research for a clinically indicated DXA bone density measurement were recruited. Height, weight, age, medical history regarding diseases affecting bone health, chronic diseases, fracture status with differentiation regarding adequate/inadequate trauma, medications negatively affecting bone health, as well as osteoprotective and osteoanabolic medications were assessed. To reflect the distribution of fracture rate with respect to BMD in postmenopausal women, the patient recruitment was stratified into three groups according to the results of the DXA measurement (lowest T-score of lumbar spine and proximal femur) and fracture status, ie, OP: osteoporosis (T-score ≤ −2.5); OPE-Fx: osteopenia (T-score between −1 and −2.5) and prevalent fragility fracture; OPE-nFx: osteopenia (T-score between −1 and −2.5) without prevalent fragility fracture. Exclusion criteria were (i) body mass index (BMI) >30; (ii) presence of metal implants or edema at the lower extremity; (iii) no allowance for X-ray exposure; or (iv) the inability to understand the nature of the study and follow the instructions. In addition to the measurements on patients, repeated ultrasound readings were performed on three healthy volunteers. The study was registered in the German Clinical Trial Register (DRKS00022217) and was approved by the local ethics committee of the Charité–University Hospital Berlin (reference number: EA4/068/19) and the German Federal Office for Radiation Protection (reference number: Z5-22464/2019-090-G). All participants provided their informed written consent before participation.

90

2.2 DXA bone densitometry

DXA (Lunar Prodigy Advance EnCore Software v. 13.4 or Lunar iDXA EnCore Software v. 16.1, GE Medical Systems, Madison, WI, USA) lumbar spine (L_1 to L_4) and proximal femur scans were performed as part of the clinical routine examination according to the standard GE Lunar operator manual. The leg (left or right side) with the lowest aBMD at the proximal femur was defined as index leg for subsequent ultrasound and HR-pQCT readings. aBMD values were assessed at the femoral neck ($aBMD_{Femur(Neck)}$), the total proximal femur area ($aBMD_{Femur(Total)}$), and at the spine ($aBMD_{Spine}$). T-scores were calculated, whereas the minimum scores at femur (T-score$_{Femur}$), spine T-score$_{Spine}$, and the lowest value of both anatomical regions (T-score$_{Total}$) were used for further analyses. If the T-score from one region could not be assessed, the other one was defined as T-score$_{Total}$.

2.3 Cortical backscatter (CortBS)

The measurement principle has been described in detail previously.[26] Briefly, a medical ultrasound scanner SonixTOUCH equipped with a SonixDAQ single-channel data acquisition system and a 4DL14-5/38 3-D linear array transducer (Ultrasonix, Richmond, Canada) was used. The system was controlled through a custom-developed user interface. Measurements were performed at the central anteromedial tibia region. The tibia length (L_{Tibia}) was assessed as the distance between the medial knee joint cleft and the medial malleolus. Both landmarks were palpated manually. Between these two points, the level of 50% L_{Tibia} was marked with a skin marker pencil. The ultrasound transducer was coupled to the skin at this position using an ultrasound coupling pad (aquaflex, Parker Laboratories, Inc., Fairfield, NJ, USA). Conventional B-mode images were used to position the probe such that a cross-sectional image of the periosteal tibia bone interface appeared in the center of the image. The probe was then manually tilted until the bone surface was approximately normal to the sound beam direction and the focus position F_z was adjusted to be approximately 1 mm below the periosteal bone surface (Fig. 1A).

For the measurement, a compound B-mode volume scan sequence was used. For the compound B-mode scan, a slightly focused beam produced by a 16-element aperture was scanned across the array from element position 1 to 128 with an increment of 1. For each transmit beam, pre-beamformed pulse-echo data were acquired from all 128 elements of the probe. The scan was repeated three times with different beam steering angles ($-10°$, $0°$, $10°$). The integrated motor allowed one to sweep the transducer array perpendicular to the compound B-mode imaging plane with tilt angles between $\pm7°$ with an increment of $1°$. Thereby, a cortical bone surface area of approximately 5 mm $\times$ 35 mm was probed at various beam inclination angles. The scan duration was less than 3 seconds. The signal analysis consists of (i) reconstruction of beamformed compound images for all sweep motor positions, ie, spatial compounding of all three beam steering angles (Fig. 1A); (ii) manual selection of a region of interest covering the bone region to be analyzed (Fig. 1B); (iii) automatic detection and 3D reconstruction of the periosteal bone surface (Fig. 1B); (iv) calculation of local beam inclinations, an inclination-corrected mean surface reflection spectrum and an inclination-controlled depth-dependent normalized mean difference spectrum NDS from the pre-beamformed channel data (Fig. 1C); (v) estimation of the frequency-dependent cortical bone attenuation and backscatter

coefficients $\alpha(f)$ and BSC(f), respectively (Fig. 1D–E); and (vi) the estimation of the cortical pore diameter distribution Ct.Po.Dm.D (Fig. 1F). The latter is obtained by minimizing the error between the measured and theoretical BSCs, which are modeled from arbitrary pore-size distributions. The acquisition and analysis ensure that only signals measured with limited beam inclination (ie, $\pm10°$ and $\pm30°$ for surface reflection and subsurface backscatter, respectively) were included in the analysis. Except for step 2, all analysis steps were processed fully automatically. A quality parameter, which provides a relative measure of usable data within the selected ROI (ie, data were not discarded by inclination, signal level, and other thresholds), was used as an objective criterion to either accept or reject a measurement. Based on repeated measurement with variable probe tilt, a quality score threshold of 77% was found to produce reproducible results (data not shown). From Ct.α(f), slope and intercept values Ct.α_f and Ct.α_o were obtained by linear regression (Fig. 1D). Characteristic parameters describing the asymmetric pore-diameter distribution Ct.Po.Dm.D (ie, 10% and 90% quantiles Q10 and Q90, respectively; width, minimum and maximum crossing points of full-width half-maximum (FWHM) values, and peak position were derived (Fig. 1F).

2.4 CortBS short-term precision

The short-term precision was evaluated according to Gluer and colleagues[27] by performing 10 repeated measurements with repositioning between each measurement on three healthy volunteers. Absolute and relative precision values were calculated using Equations (4a) and (5) in Gluer and colleagues,[27] respectively.

2.5 High-resolution peripheral computed tomography

Immediately after the CortBS measurement, a site-matched HR-pQCT scan was performed (XtremeCT II, Scanco Medical AG, Bassersdorf, Switzerland). Subjects were seated in a comfortable, height-adjustable chair. The lower leg of the subjects was positioned carefully in a carbon-fiber cast and fixated in the gantry. Subjects were instructed to sit as still as possible and to not talk or move to avoid motion artifacts. The gantry was moved into the scanner until the skin mark and the laser position indicator were aligned. A total scan length of 10.2 mm in the axial direction divided into 168 cross-sectional images was measured with an isotropic voxel size of 60.7 μm with a scan time of 2 minutes. The total effective dose was less than 5 mSv per scan. A representative reconstructed cross-sectional image is shown in Fig. 2A. Cortical and trabecular properties of the tibia were evaluated using the 3D Density and Structure Analysis software of the scanner as described elsewhere.[28] Moreover, cortical properties of (i) the entire tibia cross section (full) and (ii) a manually selected anteromedial region of interest (ROI; Fig. 2) were evaluated using a custom protocol adapted from Iori and colleagues.[20] This analysis estimates cortical porosity (Ct.Po$_{BH}$) using the algorithm proposed by Burghardt and colleagues,[29] cortical thickness (Ct.Th), pore density (Ct.Po.Dn), and distributions of porosity (Ct.Po.D), pore diameter (Ct.Po.Dm), and bone mineral density (Ct.BMD.D).[20] From these distributions, characteristic properties, ie, mean, standard deviation variance, skewness, kurtosis, as well as 10% and 90% quantile (Q10 and Q90) values, were derived.
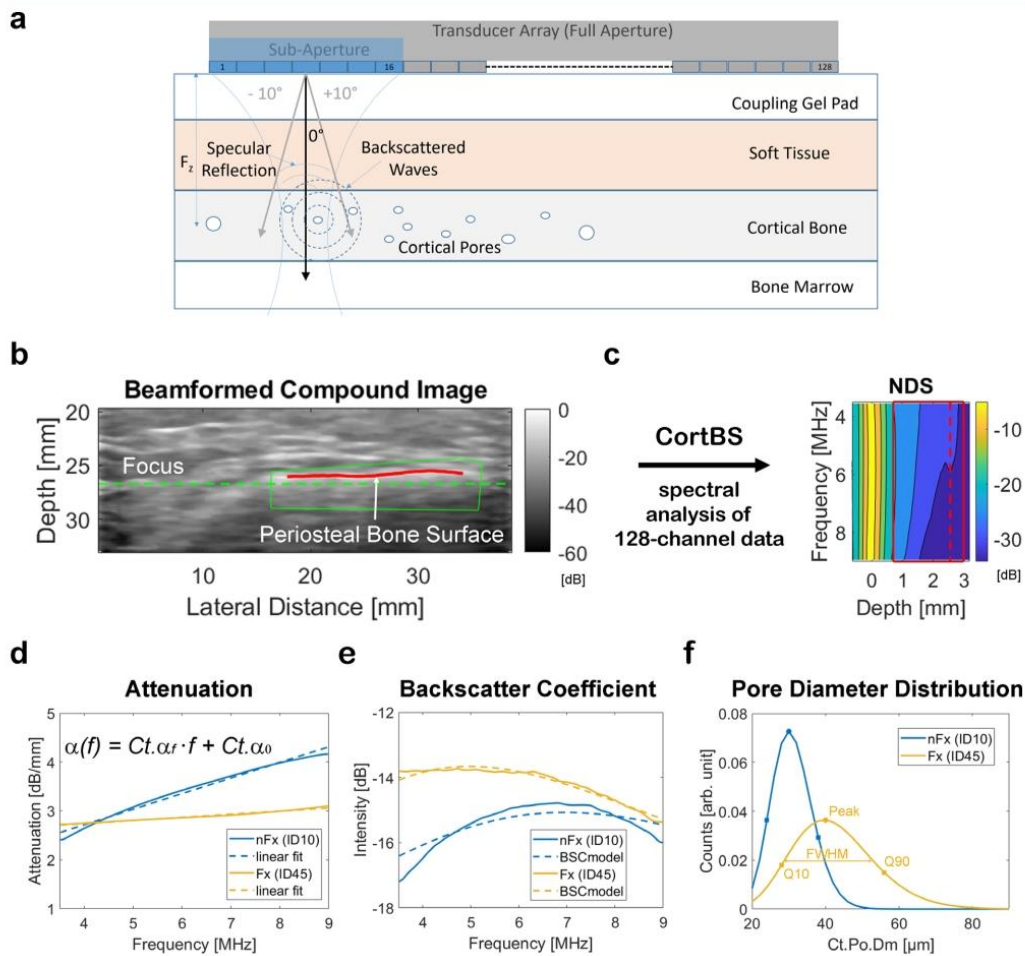
Fig 1. Schematic drawing of the CortBS method (*A*). A focused beam generated by a 16-element subaperture of the 128-element transducer array is scanned and steered across the bone. The focus depth F_z is positioned approximately 1 mm below the bone surface. Pulse-echo signals are recorded simultaneously with all 128 channels. The reconstructed compound B-mode compound image (*B*) shows the anteromedial cross section of the tibia midshaft (green dashed line: focus position; green line: manually selected ROI; red line: detected periosteal interface within ROI). The reconstructed 3D bone surface (red line) is used to calculate a depth-dependent spectrogram. Spectra arising from specular reflections at the bone surface are used for normalization. From the normalized depth-dependent backscatter spectrum (NDS) (*C*), the depth and frequency ranges of 1 to 3 mm and 4 to 9 MHz, respectively, are used to derive the attenuation and backscatter coefficients $\alpha(f)$ (*D*) and BSC(f) (*E*). By fitting model-based backscatter coefficients[26] to the measured BSC(f), the cortical pore diameter distribution Ct.Po.Dm.D is estimated (*F*). (*E, F*) Shown are representative $\alpha(f)$, BSC(f), and Ct.Po.Dm.D data for one subject with (ID45; *T*-score$_{Total}$ = −2.0) and one without fragility fractures (ID10; *T*-score$_{Total}$ = −3.5).

2.6 Statistics

Continuous variables are presented as means and standard deviations (SD). Nonparametric tests were used. Wilcoxon rank sum tests were performed to determine whether parameters were significantly different between the non-fractured and fractured groups. The correlation between ultrasound and X-ray parameters was assessed using Spearman's rank sum correlation coefficient ρ. To evaluate the correlation of multiple QUS parameters with HR-pQCT and DXA parameters, partial least squares (PLS) regression with threefold cross-validation was used. Spearman's rank sum correlation coefficient ρ and root mean square error (RMSE) between the predicted QUS-based parameter and
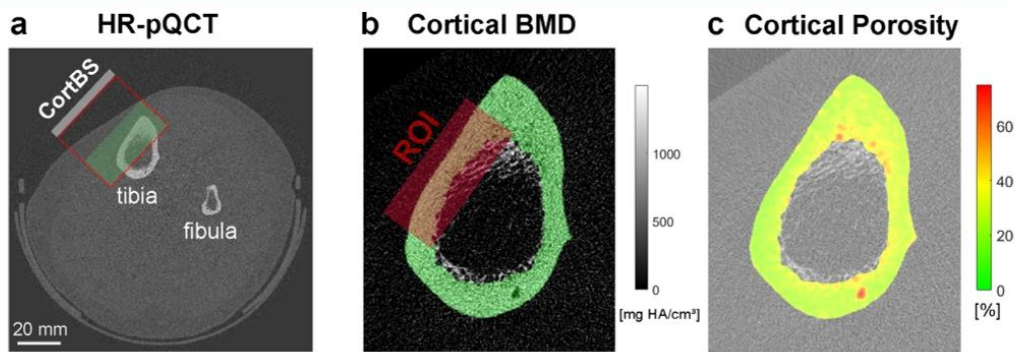
Fig 2. Representative cross-sectional HR-pQCT image with the overlaid CortBS measurement region (*A*). The box shaded in green is the image region shown in (*B*). The full tibia cross section and the site-matched CortBS measurement region were analyzed (*B*). Most of the pores in the cortical bone (marked in green) are unresolved but result in local fluctuations of the voxel values. Pores larger than ~90 μm are resolved. The calculation of a local porosity map (*C*) adapted from Iori and colleagues.[20]

those measured by HR-pQCT or DXA were computed. The fragility fracture discrimination performance of CortBS, HR-pQCT, and DXA was assessed by means of multivariate PLS discrimination analyses with Leave-One-Out Cross-Validation (PLS-LOOCV) using the libPLS library.[30] For variable selection, a subwindow permutation analysis (SPA) using 10,000 Monte Carlo samplings was repeated until a stable set of significant model variables was found. To avoid overfitting, the final models were created using three PLS components. Different discrimination models were developed to predict vertebral, other, and all fragility fractures from DXA-based *T*-scores, HR-pQCT, or CortBS parameters and for combinations with each subject's anthropometric data (weight, height, BMI), and age. The mean and standard error (SE) of the area under the curve (AUC) of the receiver operation characteristics (ROC), accuracy, sensitivity, and odds ratio (OR) with 95% confidence intervals (CI) were calculated. Differences between the AUC values were evaluated using MedcCalc 20.009a (MedCalc Software Ltd, Ostend, Belgium) by means of two-sided Hanley & McNeil tests.[31] Except for this test and the PLS-LOOC and SPA analyses, all statistical tests were performed using the Statistics Toolbox of Matlab R2019b (MathWorks, Natick, MA, USA). Statistical results were considered significant for *p* values <0.05.

3. Results

3.1 Study population

The patient characteristics are summarized in Table 1. Twenty-nine subjects had at least one fragility fracture. Among the fractured patients, 18 and 21 had vertebral and non-vertebral fractures, respectively. Age and anthropometric data were not different between fractured (Fx) and non-fractured (nFx) groups (Table 1). More subjects with fragility fractures received antiresorptive treatment than subjects without fractures. The higher number of subjects treated with an aromatase inhibitor was not significant ($p = 0.06$).

3.2 DXA

A valid vertebral spine *T*-score could not be assessed in 8 subjects because of severe degenerative changes in the lumbar spine. DXA parameters were associated with a subject's height ($\rho = 0.65$), weight ($\rho = 0.60$), and almost independent of BMI ($\rho = 0.50$) and age ($\rho = 0.45$) (Supplemental Table S1). None of the aBMD values and *T*-scores were significantly different between Fx and nFx groups (Table 2), but the difference of the lowest total *T*-scores between fractured and non-fractured groups almost reached the significance level ($p = 0.06$).

3.3 HR-pQCT

Data from one subject could not be evaluated because of an apparent motion artifact. From the remaining 54 subjects, 81 structure and material properties were extracted. HR-pQCT parameters obtained from the scanner software were associated with a subject's weight ($\rho = 0.68$), height ($\rho = 0.67$), age ($\rho = 0.54$), and almost independent of BMI ($\rho = 0.44$). Except for BMI, the associations of cortical parameters derived from the custom analysis with anthropometric data and age were generally lower (Supplemental Table S1). None of the parameters derived from the scanner software were significantly different between fractured and non-fractured groups (Table 3). In contrast, most parameters describing the local distributions of porosity and pore diameter in the anteromedial region of interest were significantly different between both groups. The most prominent differences were observed for skewness ($p = 0.004$) and kurtosis ($p = 0.004$) of the Ct.Po.Dm.D evaluated in the full cross sections.

3.4 CortBS

An ultrasound compound image of the anteromedial region of the tibia of bone together with the normalized difference spectrum and representative backscatter and attenuation coefficients and pore-size distributions for subjects with and without fragility fractures are shown in Fig. 1. The short-term precision

93

Table 1. Age, Basic Anthropometric Data, Disease, and Medication History of the Patient Cohorts With (Fx) and Without (nFx) Fragility Fractures

	All patients ($n = 55$)	Fx ($n = 29$)	nFx ($n = 26$)
Age (years)	69.9 ± 7.2	69.2 ± 7.5	70.2 ± 6.3
Height (cm)	164.2 ± 7.6	165.0 ± 8.1	163.1 ± 7.2
Weight (kg)	62.1 ± 8.3	62.4 ± 9.1	61.0 ± 6.7
Body mass index (kg/m^2)	23.0 ± 2.8	22.9 ± 2.8	23.0 ± 2.7
Diseases			
Diabetes	3	2	1
Rheumatic diseases	11	7	5
Other chronic inflammatory diseases	4	2	2
Medication			
Antiresorptive	23	17[a]	6
Osteoanabolic	5	4	1
Vitamin D	54	28	26
Selective estrogen receptor modulator (SERM)	3	1	2
Corticosteroid oral	14	7	7
Corticosteroid inhaled	3	2	1
Aromatase inhibitor	6	1	5
Proton pump inhibitor	4	1	3
Other medications[a]	25	15	10

Values are given as mean (SD) or number of subjects.
[a]$p < 0.05$.

Table 2. DXA Range, means, and SDs in Fractured (Fx) and Non-fractured (nFx) Groups

Parameter	Range	Fx ($n = 29$)	nFx ($n = 26$)
aBMD$_{Femur(Total)}$ (g/cm^2)	0.668–1.004	0.786 ± 0.072	0.808 ± 0.076
aBMD$_{Femur(Neck)}$ (g/cm^2)	0.635–0.991	0.793 ± 0.081	0.805 ± 0.072
aBMD$_{Spine}$ (g/cm^2)[a]	0.651–1.242	0.904 ± 0.130[b]	0.950 ± 0.110[c]
T-score$_{Femur}$	−3.1 to 1.5	-1.93 ± 0.86	-1.83 ± 0.55
T-score$_{Spine}$[a]	−4.3 to 0.5	-2.28 ± 1.04[b]	-1.90 ± 0.90[c]
T-score$_{Total}$[a]	−4.3 to −1.4	-2.41 ± 0.72[b]	-2.14 ± 0.66[c]

[a]$n = 47$.
[b]$n = 28$.
[c]$n = 19$.

of the individual parameter estimations was in the range between 7.9% and 13.9% (Table 4). For 5 patients, the quality factor was below 77% and, therefore, data were not analyzed. CortBS parameters were associated with subject's age ($\rho = 0.67$), height ($\rho = 0.50$), and marginally with weight ($\rho = 0.45$) and BMI ($\rho = 0.46$) (Supplemental Table S1). Parameter ranges and differences between fractured and non-fractured groups are summarized in Table 3. Slope Ct.α_f and intercept Ct.α_0 values of the attenuation coefficient were significantly different between fractured and non-fractured groups. The change of the width of the pore size distribution (Ct.Po.Dm.D$_{FWHM}$) almost reached the significance level ($p = 0.06$).

3.5 Fragility fracture discrimination

The results of discrimination performance analyses are summarized in Fig. 3 and Table 5. The DXA-based T-score values alone did not provide any significant discrimination model. Incorporating a subject's weight and height yielded significant models with, however, poor discrimination performance for vertebral and other fractures ($0.54 \leq$ AUC ≤ 0.55). Among all HR-pQCT parameters, those describing the shape distributions of porosity and pore diameter were the most predictive ones. Distinct parameter combinations provided good discrimination models for vertebral, non-vertebral, and all fragility fractures ($0.66 \leq$ AUC ≤ 0.73). Age and anthropometric information could not further improve the discrimination models. CortBS parameters provided good discrimination models for all types of fragility fractures ($0.65 \leq$ AUC ≤ 0.72). Whereas for non-vertebral fractures only attenuation parameters (Ct.α_0 and Ct.α_f) were selected, vertebral and all fractures were discriminated by a combination of attenuation and pore-size distribution parameters. Incorporation of weight and height information led to non-significant increases of the AUC values.

3.6 Associations between HR-pQCT and CortBS parameters

Attenuation was not associated with bone geometry except for one weak correlation between Ct.α_0 and Ct.Th (Supplemental Table S2). Multiple univariate associations were found for attenuation and Ct.Po.Dm.D parameters with bone density, structure, and porosity, and pore-diameter distributions. Most HR-pQCT parameters could be predicted with weak to moderate accuracy ($0.28 \leq \rho \leq 0.71$) by combinations of CortBS parameters.

94

Table 3. HR-pQCT Range, Means, and SDs of Selected Parameters in Fractured (Fx) and Non-fractured (nFx) Groups

	Range	Fx ($n = 29$)	nFx ($n = 25$)
Bone geometry			
Tt.Ar (mm^2)	313–536	420 ± 56	407 ± 47
Ct.Pm (mm)	72–100	86 ± 7	84 ± 5
Ct.Ar (mm^2)	170–318	254 ± 31	252 ± 40
Tb.Ar (mm^2)	97–298	170 ± 47	159 ± 41
Tb.Meta.Ar (mm^2)	40–121	69 ± 19	64 ± 17
Tb.Inn.Ar (mm^2)	58–177	101 ± 28	94 ± 25
Bone density			
Tt.vBMD (mg HA/cm^3)	439–748	596 ± 77	611 ± 65
Tb.vBMD (mg HA/cm^3)	32–165	77 ± 30	78 ± 30
Tb.Meta.vBMD (mg HA/cm^3)	106–291	184 ± 51	184 ± 35
Tb.Inn.vBMD (mg HA/cm^3)	−22 to 109	4.3 ± 20	5.8 ± 30
Ct.vBMD (mg HA/cm^3)	826–1049	930 ± 53	940 ± 31
Bone structure			
BV/TV	0.07–0.25	0.13 ± 0.04	0.13 ± 0.04
Tb.N (1/mm)	0.5–1.8	1.12 ± 0.29	1.18 ± 0.29
Tb.Th (mm)	0.19–0.36	0.27 ± 0.04	0.27 ± 0.03
Tb.Sp (mm)	0.56–2.05	1.01 ± 0.30	0.94 ± 0.29
Tb.1/N.SD (mm)	0.18–1.31	0.45 ± 0.22	0.39 ± 0.18
Ct.Th (mm)	2.8–6.56	4.96 ± 0.57	4.96 ± 0.83
Ct.Po (%)	0.4–8.2	2.5 ± 1.9	2.0 ± 1.0
Ct.Po.Dm (mm)	0.15–0.33	0.21 ± 0.04	0.22 ± 0.04
Custom (ROI)			
Ct.Th$_{(ROI)}$ (mm)	1.0–4.2	2.7 ± 0.8	2.7 ± 0.6
Ct.Po$_{BH(ROI)}$ (%)	1.1–11.1	5.4 ± 2.3	4.5 ± 2.2
Cortical porosity distribution			
Ct.Po.D$_{Mean(ROI)}$ (%)	14.7–33.8	26.0 ± 4.6	25.3 ± 3.6
Ct.Po.D$_{SD(ROI)}$ (%)	3.7–9.6	**6.0 ± 1.2**[a]	**5.4 ± 1.1**
Ct.Po.D$_{VAR(ROI)}$ (%)	13.5–92.9	**37.5 ± 16.2**[a]	**30.1 ± 13.2**
Ct.Po.D$_{skewness(ROI)}$	0.5–2.9	1.0 ± 0.4	1.4 ± 0.5
Ct.Po.D$_{skewness(Full)}$	0.48–2.93	**0.98 ± 0.37**[a]	**1.35 ± 0.51**
Ct.Po.D$_{kurtosis(ROI)}$	3.1–17.2	5.1 ± 1.5	7.3 ± 3.4
Ct.Po.D$_{kurtosis(Full)}$	3.1–17.2	**5.1 ± 1.5**[a]	**7.3 ± 3.4**
Cortical pore-diameter distribution			
Ct.Po.Dm.D$_{Mean(ROI)}$ (μm)	96–185	**128 ± 20**[a]	**120 ± 15**
Ct.Po.Dm.D$_{SD(ROI)}$ (μm)	39–165	83 ± 28	74 ± 23
Ct.Po.Dm.D$_{Q90(ROI)}$ (μm)	153–417	**230 ± 54**[a]	**205 ± 35**
Cortical bone BMD distribution			
Ct.BMD.D$_{kurtosis(Full)}$	3.15–5.54	**3.49 ± 0.48**[a]	**3.52 ± 0.23**

Significant differences are marked in bold. Definitions and descriptions of all variables are summarized in Supplemental Table S3.
[a] $p < 0.05$.

Table 4. CortBS Short-Term Precision (Absolute and Relative), Range, Mean, and SD Values in Fractured (Fx) and Non-fractured (nFx) Groups

Parameter	Precision	Range	Fx ($n = 25$)	nFx ($n = 25$)
Ct.α$_o$ (dB/mm)	0.22 (13.91)	1.06–3.10	**2.34 ± 0.40**[a]	**1.96 ± 0.48**
Ct.α$_f$ (dB/MHz/mm)	0.02 (15.29)	0.01–0.32	**0.11 ± 0.06**[a]	**0.16 ± 0.06**
Ct.Po.Dm.D$_{Peak}$ (μm)	2.51 (8.47)	24–52	38.6 ± 5.6	36.6 ± 7.1
Ct.Po.Dm.D$_{Q10}$ (μm)	1.93 (7.89)	20–42	29.9 ± 4.7	28.8 ± 5.8
Ct.Po.Dm.D$_{Q90}$ (μm)	3.28 (8.64)	30–64	48.7 ± 7.1	45.3 ± 8.8
Ct.Po.Dm.D$_{FWHM}$ (μm)	1.43 (11.99)	9.4–25.6	16.5 ± 3.5	14.9 ± 2.9
Ct.Po.Dm.D$_{FWHM,min}$ (μm)	2.09 (8.53)	20.0–42.8	31.1 ± 5.0	29.5 ± 5.8
Ct.Po.Dm.D$_{FWHM,max}$ (μm)	3.15 (8.62)	29.4–62.8	47.6 ± 6.8	44.4 ± 8.6

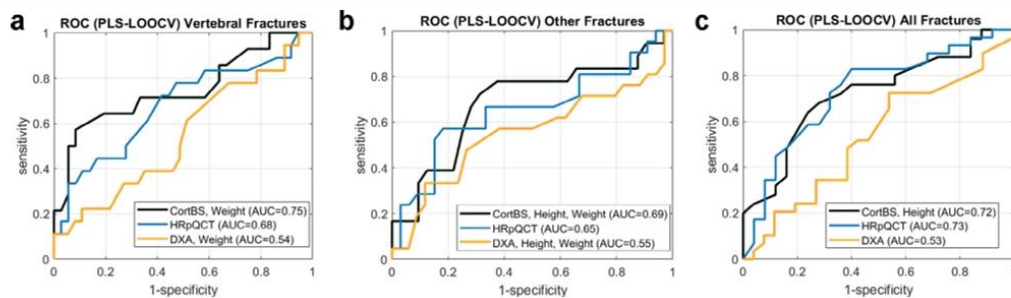Significant differences are marked in bold.
[a] $p < 0.05$.

Fig 3. Fragility fracture discrimination performance of DXA, HR-pQCT, and CortBS for vertebral fractures (*A*), other fractures (*B*), and all fractures (*C*). If anthropometric information improved the discrimination model, these ROC curves are shown.

3.7 Ultrasound-based BMD prediction

Fig. 4 shows the prediction of aBMD from CortBS parameters using multivariate PLS models. Although significant, the correlations were moderate ($0.59 \leq \rho \leq 0.63$).

4. Discussion

The diagnosis of osteoporosis based on the assessment of structural deterioration of the porous micromorphology has been prevented by the limitations of currently available diagnostic technologies.[7] The established diagnosis of OP based on aBMD captures the relative bone loss of an individual compared with a mean value of a young reference population but not the individual bone loss caused by impaired bone remodeling. Thereby, people with non-pathologically decreased *T*-scores but at risk for fragility fractures are currently undiagnosed until the fracture occurs.[8] Alternative diagnostic modalities provide X-ray radiation-free BMD and *T*-score surrogates[32–35] but do not overcome the principal lack of sensitivity of BMD to the causal microstructural and tissue deteriorations caused by OP. To date, HR-pQCT is the most sophisticated in vivo imaging modality for the microstructural analysis of bone. It can resolve pathologically enlarged cortical pores, but the spatial resolution is not sufficient to resolve the normal cortical pore micromorphology.[20] In this work, we have applied for the first time in humans a novel ultrasound technology that provides noninvasively and without ionizing radiation quantitative information about the pore-size distribution together with frequency-dependent attenuation in cortical bone at the tibia midshaft. The fracture discrimination performance of the novel CortBS technology was compared against conventional DXA-based diagnosis and state-of-the-art X-ray computed tomography (HR-pQCT).

4.1 The anteromedial tibia is a favorable site for the assessment of systemic structural bone tissue deteriorations leading to fragility fractures

The standard locations for DXA measurements (ie, L_1 to L_4 lumbar spine and hip and forearm) were initially selected because morbidity from fractures at these locations is high.[7] However, metal implants, previous fractures, scoliosis, osteosclerosis, and aortic calcifications render aBMD estimations at these sites

inaccurate or even impossible.[36] The most standardized HR-pQCT measurement site is the distal tibia.[28] In an ex vivo study, hip failure load has been reported to be associated with low vBMD and microstructural alterations measured at this site.[37] However, toward the epiphyses, cortical bone becomes thinner and is increasingly replaced by a trabecular core. Therefore, parameters assessed in this region are susceptible to both positioning errors and inter-subject anatomical differences. In this study, we have used the tibia midshaft region for the following reasons. First, the midshaft contains predominantly cortical bone. Second, the cortical thickness in the anteromedial measurement midshaft region is relatively invariant with respect to the long-axis position and approximately two to three times larger[17] than reference values reported for the proximal tibia.[38] Thereby, the tibia midshaft provides a much larger and anatomically more invariant tissue volume for cortical bone microstructural characterization than the distal shaft. Recent ex vivo studies provided evidence that structural deterioration at this measurement site is associated with reduced proximal femur strength[17] and that the parameters assessed by CortBS combined with Ct.Th provide superior predictions of proximal femur stiffness and strength compared with aBMD.[26] Ultrasound can be transmitted most easily to and along bone at the facies medialis of the tibia midshaft, where the periosteum is covered by a thin layer of soft tissue only. Already in 1995, Foldes and colleagues[39] suggested speed of sound measured by axial transmission at the tibia midshaft as an independent predictor of fracture risk in women with non-osteoporotic bone mineral density.[39] Since then, various novel bone QUS techniques have targeted this site for the measurement of Ct.Th, Ct.Po,[40,41] and speed of sound.[42] This study confirmed that a compromised pore architecture of the cortical tibia midshaft is associated with bone fragility. In line with the well-known microstructural deteriorations induced by OP, both HR-pQCT and CortBS revealed predominantly features describing the asymmetry of the cortical pore-size distribution rather parameters describing the mean pore-tissue volume fraction as factors associated with fragility fractures. Moreover, frequency-dependent ultrasound attenuation, which is determined by both structural and viscoelastic tissue properties,[26] was found to be significantly altered in subjects with fragility fractures. Recent numerical ultrasound transmission studies on three-dimensional bone mimicking structures suggested that pore

Table 5. Fragility Fracture Discrimination Performance: PLS-LOOC Discrimination Models Were Developed for the Individual Measurement Modalities Alone and in Combination With Anthropometric (AP) Data and Age

	Sensitivity	Specificity	AUC (SE)	Accuracy	OR (95% CI)	Variables
Vertebral fractures (Fx/nFx)						
DXA + AP (11/36)	0.11	0.94	0.54 (0.006)	0.67	2.2 (0.1–4.2)	$T\text{-score}_{Femur}$ Weight
HR-pQCT (18/36)	0.27	0.92	0.68^a (0.03)	0.70	4.2 (2.7–5.8)	$Ct.Po.D_{SD(ROI)}$ $Ct.Po.D_{VAR(ROI)}$ $Ct.Po.Dm.D_{Mean(ROI)}$ $Ct.Po.Dm.D_{SD(ROI)}$ $Ct.Po.Dm.D_{Q90(ROI)}$
CortBS (14/36)	0.43	0.92	0.72^a (0.009)	0.78	8.2 (6.7–9.8)	$Ct.\alpha_0, Ct.\alpha_f$ $Ct.Po.Dm.D_{FWHM}$ $Ct.Po.Dm.D_{FWHM-Max}$ $Ct.Po.Dm.D_{Q90}$
CortBS + AP (14/36)	0.50	0.94	$0.75^{a,b}$ (0.01)	0.82	17.0 (15.2–18.8)	$Ct.\alpha_0, Ct.\alpha_f$ $Ct.Po.Dm.D_{FWHM}$ $Ct.Po.Dm.D_{Q90}$ Weight
Other fractures (Fx/nFx)						
DXA + AP (15/34)	0.33	0.85	0.55 (0.02)	0.65	2.9 (1.6–4.2)	$T\text{-score}_{Femur}$ Height, weight
HR-pQCT (15/33)	0.48	0.85	0.66^a (0.03)	0.70	5.1 (3.8–6.4)	$Ct.Po_{BH(ROI)}$ $Ct.Po.D_{skewness(ROI)}$ $Ct.Po.Dn_{(ROI)}$ $Ct.Po_{BH(Full)}$ $Ct.Po.D_{skewness(Full)}$ $Ct.Po.D_{kurtosis(Full)}$ $T.Tb.Th_{(Full)}$
CortBS (12/32)	0.39	0.81	0.65^a (0.007)	0.66	2.76 (1.5–4.1)	$Ct.\alpha_0, Ct.\alpha_f$
CortBS + AP (12/32)	0.39	0.88	0.69^a (0.02)	0.70	4.45 (3.0–5.9)	$Ct.\alpha_0, Ct.\alpha_f$ Height, weight
All fractures (Fx/nFx)						
HR-pQCT (29/26)	0.83	0.64	0.73 (0.005)	0.74	8.5 (7.3–9.8)	$Ct.Po.D_{Q90(ROI)}$ $Ct.Po.D_{skewness(Full)}$
CortBS (29/25)	0.68	0.64	0.69 (0.02)	0.66	3.8 (2.6–4.9)	$Ct.\alpha_0, Ct.\alpha_f$ $Ct.PoDm.D_{Q10}$ $Ct.PoDm.D_{Q90}$ $Ct.PoDm.D_{Peak}$ $Ct.PoDm.D_{FWHM-Min}$ $Ct.PoDm.D_{FWHM-Max}$
CortBS + AP (29/25)	0.72	0.64	0.72 (0.006)	0.68	4.6 (3.4–5.8)	$Ct.\alpha_0, Ct.\alpha_f$ Height

Only significant models are listed. The numbers of fractured/non-fractured cases for each model are written in the first column in parentheses. Significant variables selected by SPA are listed in the last column. Significant differences of the AUC values between the models for each fracture group are indicated by superscript letters.

[a] AUC(CortBS/HRpQCT) > AUC(DXA + AP).
[b] AUC(CortBS+AP) > AUC(HR-pQCT).

radius and density can be inferred from the frequency dependence of ultrasonic attenuation.[43] In that study, monodisperse pore radii ranging from 50 to 100 μm and densities ranging from 20 to 50 pores per mm³ were investigated. The same group also proposed a model that aims at decoupling the effects of viscoelastic absorption and scattering.[44] Although forward and backscatter characteristics are not identical, the same concept could be integrated into the cortical backscatter model in the future to assess the relative contributions of structural and viscoelastic tissue alterations to the fragility fracture discrimination independently.

4.2 Discrimination performance

The results of this pilot study suggest a superior discrimination performance of the ultrasonic cortical backscatter measurement ($0.69 \le$ AUC ≤ 0.75) compared with DXA ($0.54 \le$ AUC ≤ 0.55) and a similar or even better performance compared with HR-pQCT ($0.66 \le$ AUC ≤ 0.73). The two attenuation parameters $Ct.\alpha_0$ and $Ct.\alpha_f$ were the strongest predictors for all types of fragility fractures. Together with the subject's height and weight, cortical bone attenuation provided the best discrimination performance for non-vertebral fractures (AUC = 0.69). The
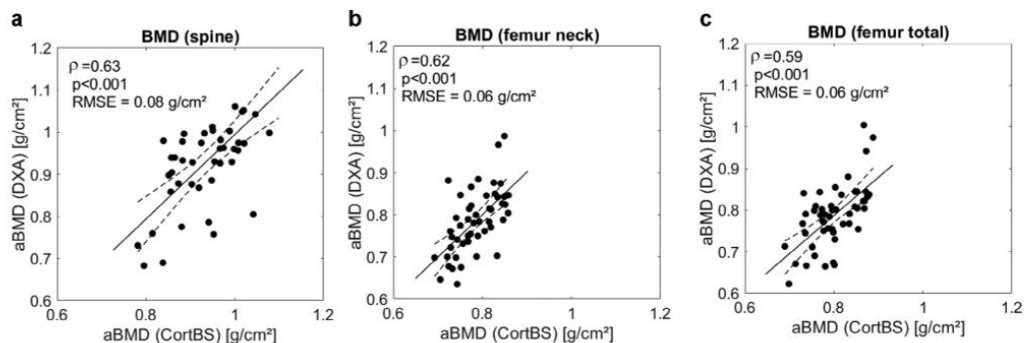
Fig 4. Estimation of aBMD at spine (*A*), femur neck (*B*), and total proximal femur (*C*) from ultrasound backscatter and anthropometric parameters using PLS regression.

subject's height is a known risk factor for non-vertebral fractures,[45] which has been partly linked to thinner and more porous cortices in taller women, as measured at the distal tibia by first-generation HR-pQCT.[46] Ct.Th at the tibia midshaft was not a predictive variable in our study, but both HR-pQCT and CortBS measurements confirmed that porosity and pore-size distributions as well as the mean porosity were associated with fragility fractures.

For vertebral fractures, attenuation together with width and 90% quantile values of the pore-diameter distribution were significant ultrasound predictor variables, while the subject's weight remained the only anthropometric factor (AUC = 0.75). This finding is in agreement with a previous report suggesting risk factors, eg, physical weakness, poor health, and weight loss, as risk factors for vertebral but not for non-vertebral fractures.[47]

Our AUC values were lower for DXA and comparable for QUS parameters than those reported in another study, in which cortical thickness and porosity were estimated from axial transmission ultrasound.[41] Although in that study on 201 postmenopausal women Ct.Th in was found to be discriminant for hip fractures only (AUC = 0.72), Ct.Po was discriminant for all fractures (AUC = 0.71) and for vertebral (AUC = 0.84) and wrist fractures (AUC = 0.71).

Several bone QUS technologies have been used in the past to measure cortical or cancellous bone sites, and at least some of them have demonstrated the potential to predict fracture risk with an equivalent efficiency compared with X-ray densitometry techniques.[23,48] Although ultrasound wave propagation is governed by the structural and material properties of the propagation medium, none of the currently available clinical devices provide any direct measurement of stiffness, strength, or tissue quality. Instead, they provide bone density, stiffness, or quality surrogate markers derived from empirical correlations of acoustic properties (eg, speed of sound [SOS] and broadband ultrasound attenuation [BUA]),[23] travel time delays,[33,49] or the shape of the backscatter spectrum[35] with aBMD. For example, Adami and colleagues[50] used *T*-scores derived from radiofrequency echographic multi spectrometry (REMS) in comparison with DXA-based *T*-scores for the discrimination of women with and without fractures as the identification of patients at risk for incident osteoporotic fractures. This prospective study on

1516 white women (aged 30 to 90 years) reported similar prediction performance for DXA- and QUS-based *T*-scores. A model-based measurement of Ct.Th and Ct.Po in radius and tibia bones has been achieved for the first time with the bidirectional axial transmission technology by means of multimode waveguide dispersion analysis.[40,51] The method considers variations of porosity as a major source of variations of cortical bone elasticity, sound velocity, and fracture toughness in postmenopausal women.[52–54] Results of a first validation study in postmenopausal women confirmed a comparable fracture discrimination performance of the BDAT variables as aBMD for both vertebral and peripheral fractures.[41] However, axial transmission measurements do not provide direct image guidance and are restricted to patients with low BMI.

CortBS reflects viscoelastic and microstructural deteriorations of cortical bone, which are causally linked to the natural aging process and the development of osteoporosis.[11] The crucial role of the porous microarchitecture, particularly the prevalence of large pores as a biomarker for reduced bone strength,[17] was also confirmed in the HR-pQCT analysis, which revealed the asymmetry of the porosity distribution but not the total porosity as a fracture discriminating tissue property. In contrast to that ex vivo study, which included bone from both male and female donors, Ct.Th was not found to be a fracture discriminating biomarker in our study.

4.3 Limitations

This pilot study has several limitations. First, the cohort size was small and restricted to postmenopausal women with *T*-scores below −1. Second, the included subjects had diverse fracture and medication histories as well as various comorbidities. However, the selected cohort resembles the population that is (i) most vulnerable for fragility fractures and (ii) mostly undertreated based on the BMD diagnosis. Despite these limitations, a good discrimination performance was achieved, which needs to be confirmed in larger studies covering a larger age range, both sexes, larger BMI ranges, and *T*-scores above −1. Third, the cross-sectional study design did not allow us to assess fracture risk. Future prospective studies should therefore evaluate the potential of CortBS parameters to identify people at risk

and to assess the individual fracture risk. Second, no real-time assessment of the CortBS measurement quality was possible in this study, which led to the exclusion of data from 5 subjects during the post hoc data analysis. For clinical applications, the data-quality assessment needs to be incorporated into the measurement, providing real-time feedback to the operator and the possibility to repeat the measurement, until an appropriate data quality is achieved.

CortBS is the first quantitative bone imaging modality that can quantify microstructural tissue deteriorations in cortical bone, which occur during normal aging and the development of osteoporosis. CortBS discriminates fragility fractures in postmenopausal women better than aBMD. It could be used as a portable, low-cost, non-ionizing, and widely applicable screening tool to identify people at risk, particularly in the population with low bone mass.

Disclosures

Acknowledgments

Peer review

The peer review history for this article is available at https://publons.com/publon/10.1002/jbm4.10536.

References

1. Feng X, McDonald JM. Disorders of bone remodeling. *Annu Rev Pathol.* 2011;6:121-145.

2. Cawthon PM. Gender differences in osteoporosis and fractures. *Clin Orthop Relat Res.* 2011;469(7):1900-1905.

3. Dhanwal DK, Dennison EM, Harvey NC, Cooper C. Epidemiology of hip fracture: worldwide geographic variation. *Indian J Orthop.* 2011; 45(1):15-22.

4. Borgstrom F, Karlsson L, Ortsater G, et al. Fragility fractures in Europe: burden, management and opportunities. *Arch Osteoporos.* 2020; 15(1):59.

5. Kanis JA, Cooper C, Rizzoli R, Reginster JY, Scientific Advisory Board of the European Society for Clinical and Economic Aspects of Osteoporosis (ESCEO) and the Committees of Scientific Advisors and National Societies of the International Osteoporosis Foundation (IOF). European guidance for the diagnosis and management of osteoporosis in postmenopausal women. *Osteoporos Int.* 2019;30(1):3-44.

6. Rendl S, Lapa C, Blumel C, Bundschuh RA, Schneider P. Decision making for osteoporotic treatment using FRAX or DVO risk algorithms in a clinical setting. *J Musculoskelet Neuronal Interact.* 2013;13(3):339-345.

7. Choksi P, Jepsen KJ, Clines GA. The challenges of diagnosing osteoporosis and the limitations of currently available tools. *Clin Diabetes Endocrinol.* 2018;4:12.

8. Hernlund E, Svedbom A, Ivergard M, et al. Osteoporosis in the European Union: medical management, epidemiology and economic burden. A report prepared in collaboration with the International Osteoporosis Foundation (IOF) and the European Federation of Pharmaceutical Industry Associations (EFPIA). *Arch Osteoporos.* 2013;8:136.

9. Siris ES, Chen YT, Abbott TA, et al. Bone mineral density thresholds for pharmacological intervention to prevent fractures. *Arch Intern Med.* 2004;164(10):1108-1112.

10. Andreasen CM, Delaisse JM, van der Eerden BC, van Leeuwen JP, Ding M, Andersen TL. Understanding age-induced cortical porosity in women: the accumulation and coalescence of eroded cavities upon existing intracortical canals is the main contributor. *J Bone Miner Res.* 2018;33(4):606-620.

11. Drake MT, Clarke BL, Lewiecki EM. The pathophysiology and treatment of osteoporosis. *Clin Ther.* 2015;37(8):1837-1850.

12. Bell KL, Loveridge N, Power J, Garrahan N, Meggitt BF, Reeve J. Regional differences in cortical porosity in the fractured femoral neck. *Bone.* 1999;24(1):57-64.

13. Zebaze R, Seeman E. Cortical bone: a challenging geography. *J Bone Miner Res.* 2015;30(1):24-29.

14. Chen H, Zhou X, Shoumura S, Emura S, Bunai Y. Age- and gender-dependent changes in three-dimensional microstructure of cortical and trabecular bone at the human femoral neck. *Osteoporos Int.* 2010;21(4):627-636.

15. Nishiyama KK, Macdonald HM, Buie HR, Hanley DA, Boyd SK. Postmenopausal women with osteopenia have higher cortical porosity and thinner cortices at the distal radius and tibia than women with normal aBMD: an in vivo HR-pQCT study. *J Bone Miner Res.* 2010; 25(4):882-890.

16. Iori G, Schneider J, Reisinger A, et al. Cortical thinning and accumulation of large cortical pores in the tibia reflect local structural deterioration of the femoral neck. *Bone.* 2020;137:115446.

17. Iori G, Schneider J, Reisinger A, et al. Large cortical bone pores in the tibia are associated with proximal femur strength. *PLoS One.* 2019; 14(4):e0215405.

18. Griffith AA. VI. The phenomena of rupture and flow in solids. *Philos Trans R Soc London Ser A.* 1921;221(582–593):163-198.

19. Kendall K, Howard AJ, Birchall JD. The relation between porosity, microstructure and strength, and the approach to advanced cement-based materials. *Philos Trans R Soc London Ser A.* 1983; 310(1511):139-153.

20. Iori G, Heyer F, Kilappa V, et al. BMD-based assessment of local porosity in human femoral cortical bone. *Bone.* 2018;114:50-61.

21. Schuit SC, van der Klift M, Weel AE, et al. Fracture incidence and association with bone mineral density in elderly men and women: the Rotterdam Study. *Bone.* 2004;34(1):195-202.

22. Wainwright SA, Marshall LM, Ensrud KE, et al. Hip fracture in women without osteoporosis. *J Clin Endocrinol Metab.* 2005;90(5):2787-2793.

99

23. Hans D, Baim S. Quantitative ultrasound (QUS) in the management of osteoporosis and assessment of fracture risk. *J Clin Densitom.* 2017; 20(3):322-333.

24. Nicholson PF. Ultrasound and the biomechanical competence of bone. *IEEE Trans Ultrason Ferroelectr Freq Control.* 2008;55(7):1539-1545.

25. Grimal Q, Laugier P. Quantitative ultrasound assessment of cortical bone properties beyond bone mineral density. *IRBM.* 2019;40(1): 16-24.

26. Iori G, Du J, Hackenbeck J, Kilappa V, Raum K. Estimation of cortical bone microstructure from ultrasound backscatter. *IEEE Trans Ultrason Ferroelectr Freq Control.* 2021;68(4):1081-1095.

27. Gluer CC, Blake G, Lu Y, Blunt BA, Jergas M, Genant HK. Accurate assessment of precision errors: how to measure the reproducibility of bone densitometry techniques. *Osteoporos Int.* 1995;5(4):262-270.

28. Whittier DE, Boyd SK, Burghardt AJ, et al. Guidelines for the assessment of bone density and microarchitecture in vivo using high-resolution peripheral quantitative computed tomography. *Osteoporos Int.* 2020;31(9):1607-1627.

29. Burghardt AJ, Buie HR, Laib A, Majumdar S, Boyd SK. Reproducibility of direct quantitative measures of cortical bone microarchitecture of the distal radius and tibia by HR-pQCT. *Bone.* 2010;47(3):519-528.

30. Li HD, Xu QS, Liang YZ. libPLS: an integrated library for partial least squares regression and linear discriminant analysis. *Chemometr Intell Lab Syst.* 2018;176:34-43.

31. Hanley JA, McNeil BJ. The meaning and use of the area under a receiver operating characteristic (ROC) curve. *Radiology.* 1982; 143(1):29-36.

32. Lewiecki EM. Pulse-echo ultrasound identifies Caucasian and Hispanic women at risk for osteoporosis. *J Clin Densitom.* 2021;24(2): 175-182.

33. Karjalainen JP, Riekkinen O, Kroger H. Pulse-echo ultrasound method for detection of post-menopausal women with osteoporotic BMD. *Osteoporos Int.* 2018;29(5):1193-1199.

34. Behrens M, Felser S, Mau-Moeller A, et al. The Bindex((R)) ultrasound device: reliability of cortical bone thickness measures and their relationship to regional bone mineral density. *Physiol Meas.* 2016;37(9): 1528-1540.

35. Diez-Perez A, Brandi ML, Al-Daghri N, et al. Radiofrequency echographic multi-spectrometry for the in-vivo assessment of bone strength: state of the art-outcomes of an expert consensus meeting organized by the European Society for Clinical and Economic Aspects of Osteoporosis, Osteoarthritis and Musculoskeletal Diseases (ESCEO). *Aging Clin Exp Res.* 2019;31(10):1375-1389.

36. Garg MK, Kharb S. Dual energy X-ray absorptiometry: pitfalls in measurement and interpretation of bone mineral density. *Indian J Endocrinol Metab.* 2013;17(2):203-210.

37. Kroker A, Plett R, Nishiyama KK, McErlain DD, Sandino C, Boyd SK. Distal skeletal tibia assessed by HR-pQCT is highly correlated with femoral and lumbar vertebra failure loads. *J Biomech.* 2017;59: 43-49.

38. Whittier DE, Burt LA, Hanley DA, Boyd SK. Sex- and site-specific reference data for bone microarchitecture in adults measured using second-generation HR-pQCT. *J Bone Miner Res.* 2020;35(11):2151-2158.

39. Foldes AJ, Rimon A, Keinan DD, Popovtzer MM. Quantitative ultrasound of the tibia: a novel approach for assessment of bone status. *Bone.* 1995;17(4):363-367.

40. Schneider J, Ramiandrisoa D, Armbrecht G, et al. In vivo measurements of cortical thickness and porosity at the proximal third of the tibia using guided waves: comparison with site-matched peripheral quantitative computed tomography and distal high-resolution peripheral quantitative computed tomography. *Ultrasound Med Biol.* 2019;45(5):1234-1242.

41. Minonzio JG, Bochud N, Vallet Q, et al. Ultrasound-based estimates of cortical bone thickness and porosity are associated with nontraumatic fractures in postmenopausal women: a pilot study. *J Bone Miner Res.* 2019;34(9):1585-1596.

42. Renaud G, Kruizinga P, Cassereau D, Laugier P. In vivo ultrasound imaging of the bone cortex. *Phys Med Biol.* 2018;63(12):125010.

43. White RD, Yousefian O, Banks HT, Alexanderian A, Muller M. Inferring pore radius and density from ultrasonic attenuation using physics-based modeling. *J Acoust Soc Am.* 2021;149(1):340.

44. Yousefian O, Karbalaeisadegh Y, Muller M. Frequency-dependent analysis of ultrasound apparent absorption coefficient in multiple scattering porous media: application to cortical bone. *Phys Med Biol.* 2021;66(3):035026.

45. Roux C, Briot K, Horlait S, Varbanov A, Watts NB, Boonen S. Assessment of non-vertebral fracture risk in postmenopausal women. *Ann Rheum Dis.* 2007;66(7):931-935.

46. Bjornerem A, Bui QM, Ghasem-Zadeh A, Hopper JL, Zebaze R, Seeman E. Fracture risk and height: an association partly accounted for by cortical porosity of relatively thinner cortices. *J Bone Miner Res.* 2013;28(9):2017-2026.

47. Finigan J, Greenfield DM, Blumsohn A, et al. Risk factors for vertebral and nonvertebral fracture over 10 years: a population-based study in women. *J Bone Miner Res.* 2008;23(1):75-85.

48. Moayyeri A, Adams JE, Adler RA, et al. Quantitative ultrasound of the heel and fracture risk assessment: an updated meta-analysis. *Osteoporos Int.* 2012;23(1):143-153.

49. Stein EM, Rosete F, Young P, et al. Clinical assessment of the 1/3 radius using a new desktop ultrasonic bone densitometer. *Ultrasound Med Biol.* 2013;39(3):388-395.

50. Adami G, Arioli G, Bianchi G, et al. Radiofrequency echographic multi spectrometry for the prediction of incident fragility fractures: a 5-year follow-up study. *Bone.* 2020;134:115297.

51. Vallet Q, Bochud N, Chappard C, Laugier P, Minonzio JG. In vivo characterization of cortical bone using guided waves measured by axial transmission. *IEEE Trans Ultrason Ferroelectr Freq Control.* 2016;63(9): 1361-1371.

52. Peralta L, Maeztu Redin JD, Fan F, et al. Bulk wave velocities in cortical bone reflect porosity and compression strength. *Ultrasound Med Biol.* 2021;47(3):799-808.

53. Granke M, Makowski AJ, Uppuganti S, Nyman JS. Prevalent role of porosity and osteonal area over mineralization heterogeneity in the fracture toughness of human cortical bone. *J Biomech.* 2016;49(13): 2748-2755.

54. Granke M, Grimal Q, Saied A, Nauleau P, Peyrin F, Laugier P. Change in porosity is the major determinant of the variation of cortical bone elasticity at the millimeter scale in aged women. *Bone.* 2011;49(5): 1020-1026.

100

Lebenslauf

Mein Lebenslauf wird aus datenschutzrechtlichen Gründen in der elektronischen Version meiner Arbeit nicht veröffentlicht.

Vollständige Publikationsliste von Minh Huong Nguyen-Ullrich

Published

Nguyen Minh H, Muller M, Raum K. Estimation of Thickness and Speed of Sound for Transverse Cortical Bone Imaging Using Phase Aberration Correction Methods: An In Silico and Ex Vivo Validation Study. Applied Sciences. 2022;12(10):5283. Impact Factor: 2.679

Armbrecht G, Nguyen Minh H, Massmann J, Raum K. Pore-Size Distribution and Frequency-Dependent Attenuation in Human Cortical Tibia Bone Discriminate Fragility Fractures in Postmenopausal Women With Low Bone Mineral Density. JBMR Plus. 2021. Impact Factor: 6.284

Nguyen Minh H, Du J, Raum K. Estimation of Thickness and Speed of Sound in Cortical Bone Using Multifocus Pulse-Echo Ultrasound. IEEE Trans Ultrason Ferroelectr Freq Control. 2020;67(3):568-79. Impact Factor: 2.989

Rauch T, Nguyen Minh H, Henk J, Mertig I. Model for ferromagnetic Weyl and nodal line semimetals: Topological invariants, surface states, anomalous and spin Hall effect. Physical Review B. 2017;96(23):235103. Impact Factor: 3.575

Abstracts – conferences – oral presentation

Nguyen Minh, H, Raum, K, Estimation of Thickness and Speed of Sound using refraction and phase aberration corrected pulse-echo ultrasound. International Symposium on Ultrasonic Characterization of Bone (ISUCB), *06/*2019 Frejus, France.

Nguyen Minh, H, Raum, K, Estimation of cortical thickness and speed of sound using multi-focus and pulse-echo ultrasound. 25th Congress of the European Society of Biomechanics (ESB), 07/2019 Vienna, Austria.

Nguyen Minh, H, Raum, K, Estimation of Thickness and Speed of Sound using refraction and phase aberration corrected pulse-echo ultrasound. IEEE International Ultrasonics Symposium (IUS), 10/2019 Glasgow, Scotland.

Abstracts – conferences – poster presentation

Nguyen Minh, H, Du, J, Raum, K, Estimation of cortical micromorphology from high frequency ultrasound backscatter. *International Symposium on Ultrasonic Characterization of Bone (ISUCB), 06/*2019 Frejus, France.

Nguyen Minh, H, Du, J, Raum, K, Estimation of cortical micromorphology from high frequency ultrasound backscatter. IEEE International Ultrasonics Symposium (IUS), 10/2019 Glasgow, Scotland.

Acknowledgements/Danksagung

My PhD has been a truly formative and life-changing experience and would not have been possible without the support and guidance that I have received from many people.

I would like to thank my supervisor Prof. Kay Raum for giving me the opportunity to do research in his group and his guidance throughout the work. His guidance and regular meetings were essential to this work. I also would like to thank Dr. Gabriele Armbrecht for the great cooperation throughout the patient study. In addition, I am also grateful to get the support of Prof. Marie Muller.

I also thank the industrial collaborators, especially Matthias Jurgk from Gampt mbH and Prof. Uwe Heuert from exceeding solution GmbH, who supported me in implementing the Multifocus and CortBS method into the Ultrasonix system.

I also thank the Berlin-Brandenburg School for Regenerative Therapies (BSRT) and Sabine Bartosch for the workshop, where I gained a lot of knowledge and where I was able to network with international students.

I also extend thank and appreciate my lab mates for their support, all funny moments we collected together. A special thanks to Urszula for supporting me in the lab and the emotional support throughout the whole time. I am very grateful for Regina, who always had the time for emotional support and advice and her uplifting, warm words. Many thanks to Nirina for spreading positive energy and the emotional support, especially throughout my first international conference. I am grateful to meet Gianluca, who supported me in the beginning of my PhD. I also want to express my gratitude to my former colleagues and now friends Jiahan and Mathis. In summary, I really cherish the time we all spent together in the lab. Many thanks to Jenny for proofreading my last paper and my thesis.

Finally, I want to express my sincere gratitude to my family and my closest friends. Thank you to my life partner Erik for all your unlimited support, unconditional love and for always believing in me even when I doubt myself. Thanks for filling my days with positive energy and optimism in a daily basis. Thank you for being my rock. I am also especially very grateful for my best friend Nam, who was so caring and support the whole time. I especially thank my mom, dad and sister for always believing in me and encouraging me to pursue my dreams. My lovely sister Phuong always enlightens my lowest moments. Thank you for not only being the best sister, but also a best friend. Without the support of you all this work would not have been possible.

I dedicate this thesis to my family, my life partner Erik, my friends for their unconditional love and constant support. I love you all truthfully.